A Fault Diagnosis System
for
Rotary Machinery Supported by Rolling Element Bearings

by

Shahab Hasanzadeh Ghafari

A thesis
presented to the University of Waterloo
in fulfillment of the
thesis requirement for the degree of
Doctor of Philosophy
in
Mechanical Engineering

Waterloo, Ontario, Canada, 2007

Author's Declaration

I hereby declare that I am the sole author of this thesis. This is a true copy of the thesis, including any required final revisions, as accepted by my examiners.

Signature

I understand that my thesis may be made electronically available to the public.

Signature

Abstract

The failure of rolling element bearings is one of the foremost causes of breakdown in rotary machinery. So far, a variety of vibration-based techniques have been developed to monitor the condition of bearings; however, the role of vibration behavior is rarely considered in the proposed techniques.

This thesis presents an analytical study of a healthy rotor-bearing system to gain an understanding of the different categories of bearing vibration. In this study, a two degree-of-freedom model is employed, where the contacts between the rolling elements and races are considered to be nonlinear springs. The analytical investigations confirm that the nature of the inner ring oscillation depends on the internal clearance. A fault-free bearing with a small backlash exhibits periodic behavior; however, bearings categorized as having normal clearance oscillate chaotically. The results from the numerical simulations agree with those from the experiments confirming bearing's chaotic response at various rotational speeds.

Bearing faults generate periodic impacts which affect the chaotic behavior. This effect manifests itself in the phase plane, Poincare map, and chaotic quantifiers such as the Lyapunov exponent, correlation dimension, and information entropy. These quantifiers serve as useful indices for detecting bearing defects. To compare the sensitivity and robustness of chaotic indices with those of well-accepted fault detection techniques, a comprehensive investigation is conducted. The test results demonstrate that the Correlation Dimension (CD), Normalized Information Entropy (NIE), and a proposed time-frequency index, the Maximum Approximate Coefficient of Wavelet transform (MACW), are the most reliable fault indicators.

A neuro-fuzzy diagnosis system is then developed, where the strength of the aforementioned indices are integrated to provide a more robust assessment of a bearing's health condition. Moreover, a prognosis scheme, based on the Adaptive Neuro Fuzzy Inference System (ANFIS), in combination with a set of logical rules, is proposed for estimating the next state of a bearing's condition. Experimental results confirm the viability of forecasting health condition under different speeds and loads.

Acknowledgements

First of all, I would like to express my sincere thanks to my supervisors, Professor Farid Golnaraghi and Professor Fathy Ismail, whose encouragement, guidance, and knowledge have made it possible for me to complete this thesis. In addition, I am grateful to Dr. Lin, Professor Lambert, Dr. Abdel-Rahman, and Dr. Melek for their detailed review and excellent advices.

The financial support from Natural Sciences and Engineering Research Council of Canada (NSERC), University of Waterloo graduate scholarship, and my supervisors, is greatly appreciated.

Of equal importance, I wish to thank my friends: Nima Eslaminasab, Orang Vahid, Chris McClellan, Golzar Taravati, Kiarash Narimani, Hamidreza Bolandhemat, Babak Ebrahimi, Madu Thirugnanasam, Brad Schubert, Yu Shen, Peter Liu, and Dr. Wilson Wang. Also, a special thank to Dr. Arash Narimani and Dr. Siamak Arzanpour for their friendship, help and support.

Many thanks go to Robert Wagner and Andy Barber, the technical staff of the department, for their conscientious effort.

I have benefited greatly from the support of my sister, Naghmeh, Dr. Peyman Servati, Amir Taravati and Dr. Manijeh Kimiavi.

I would like to express my deepest appreciation to my father, Mehdi Hasanzadeh Ghafari and my mother Dr. Minoo Rafiee for their everlasting love, support and encouragement.

Lastly but most importantly, I would like to express my deepest gratitude for the constant support, patience, understanding and love that I received from my wife Bahar and my lovely daughters Avin and Tara during the past years. It is to them that I dedicate this thesis.

Table of Contents

Introduction **1**
1.1 Overview 1
1.2 Bearing Condition Monitoring Techniques 3
1.3 Vibration Based Condition Monitoring 5
1.4 Motivation and Objectives 8
1.5 Thesis Outline 9
Analytical Investigation of Bearing Vibration **10**
2.1 System Modeling 12
2.2 Load Distribution Angle 16
2.3 Equilibrium Points 17
2.4 Analytical Solution 22
2.4.1 Case 1: Zero Clearance Ball Bearings 24
2.4.2 Case 2: Small Clearance Ball Bearing, Clearance Class 1 29
2.5 Chaotic Vibration of the Inner Ring 34
2.6 Summary 37
Numerical Analysis and Experimental Verification **38**
3.1 Numerical Simulation 40
3.2 Experimental Observations 50
3.3 Summary 54
Fault Diagnosis and Chaotic Indicators **55**
4.1 Chaotic Indicators 56
4.1.1 Lyapunov Exponent 57
4.1.2 Correlation Dimension 59
4.1.3 Information Entropy 61
4.2 Effect of Machinery Faults on Chaotic Indicators 62
4.2.1 Bearing Localized Faults 63
4.2.2 Imbalance and Misalignment 68
4.3 Summary 71

Assessment of Bearing Condition Monitoring Techniques 72
5.1 Data Acquisition and Signal Pre-Processing 75
5.2 Fault Index Extraction and Signal Processing Techniques 77
5.2.1 Kurtosis 77
5.2.2 Crest Factor 78
5.2.3 Envelope analysis 78
5.2.4 High Frequency Resonant Technique (HFRT) 80
5.2.5 Lyapunov Exponent 81
5.2.6 Continuous Wavelet Map 82
5.2.7 Discrete Wavelet Transform 84
5.2.8 Correlation Dimension 85
5.2.9 Normalized Information Entropy 85
5.3 Experimental Results and Discussions 86
5.3.1 Inner Race Fault 88
5.3.2 Outer Race Fault 90
5.3.3 Rolling Element Damage 91
5.4 Effect of Speed and Load on Selected Monitoring Indices 96
5.5 Summary 100
Neuro-Fuzzy Diagnosis System 101
6.1 Decision-making Schemes 103
6.1.1 Multi Layer Perceptron (MLP) 104
6.1.2 Radial Basis Function Network (RBF) 104
6.1.3 Adaptive Neuro-Fuzzy Inference System (ANFIS) 105
6.2 Results and Discussion 106
6.3 Summary 110
Bearing Condition Prognosis 111
7.1 Experimental Setup 113
7.2 Monitoring indices 114
7.3 Neural Network Predictors 114
7.3.1 Recurrent Neural Networks (RNN) 115
7.3.2 Adaptive Neuro-Fuzzy Inference System (ANFIS) 116

7.4 Bearing Fault State Prognosis 116
7.5 Summary 124
Conclusions 125
Appendix I 128
Appendix II 131
References 133

List of Figures

Figure 2.1. Simplified model of a rotor supported by two bearings 12
Figure 2.2. Rolling element bearing 2 DOF model 13
Figure 2.3. Radial deformation of rolling element in bearing assembly 14
Figure 2.4. Load distribution angle 16
Figure 2.5. Location of the equilibrium points when $\omega \approx 0$ 19
Figure 2.6. Response orbits and equilibrium points 20
Figure 2.7. Location of the stable and unstable dynamic equilibrium points 21
Figure 2.8. Comparison of the original model with first-, second-, and third-order approximation 22
Figure 2.9. Comparison between the original model and first-, second-, and third-order approximations for $e = 4\mu m$ 23
Figure 2.10. Parameters α_{mn}, f_x, f_y and their approximations 25
Figure 2.11. The frequency-response curves for ($e = 0\ \mu m$) 29
Figure 2.12. Valid ranges of approximation 29
Figure 2.13. Frequency-response curves for ($e = 4\ \mu m$) 33
Figure 2.14. Two-dimensional projections of the inner ring motion 34
Figure 2.15. : Poincare maps of the inner ring motion 35
Figure 2.16. Bifurcation diagram e=7 μm 36
Figure 2.17. Period doubling e=7 μm 36
Figure 2.18. Chaos map ball bearing SKF 6204 37
Figure 3.1. Bearing impact test 43
Figure 3.2. Bearings modal impact test 43
Figure 3.3. Poincare maps of simulation results 45
Figure 3.4. Numerical simulations for broad-band bifurcation diagrams 46
Figure 3.5. Simulation results: detailed bifurcation diagram for a ball bearing 47
Figure 3.6. Route to chaos in ball bearing SKF 6204 48
Figure 3.7. Route to chaos in cylindrical roller bearing SKF NJ204ECP 50
Figure 3.8. Experimental test bed 51
Figure 3.9. Vibration of ball bearing (experimental data) 52

Figure 3.10. Experimental Poincare map 53
Figure 4.1. Stability Lyapunov exponent at various shaft rotational speeds 58
Figure 4.2. Experimental correlation dimension and measured error band 60
Figure 4.3. Stability information entropy at various shaft rotational speeds 62
Figure 4.4. Simulation results: Effect of localized faults on the chaotic attractor 64
Figure 4.5. Effect of the localized defects on the Lyapunov exponent 66
Figure 4.6. Effect of the localized defects on the correlation dimension 67
Figure 4.7. Effect of the localized defects on the information entropy 68
Figure 4.8. Effect of imbalance on the strange attractor 69
Figure 4.9. Effect of misalignment on the strange attractor 70
Figure 5.1. Bearing induced localized faults 76
Figure 5.2. HFRT signal processing flow diagram 81
Figure 5.3. Morlet Wavelet 83
Figure 5.4. Scaling and wavelet function of *db4* 84
Figure 5.5. Condition monitoring of bearing with inner race fault 93
Figure 5.6. Condition monitoring of bearing with outer race fault 94
Figure 5.7. Condition monitoring of bearing with rolling element damage 95
Figure 5.8. Schematic of load-speed test bed 97
Figure 5.9. Variation of the Normalized Information Entropy (NIE) 98
Figure 5.10. Variation of correlation dimension (CD) 98
Figure 5.11. Variation of the Maximum Approximate Coefficient of Wavelet (MACW) 99
Figure 6.1. Bearing condition decision-making process 103
Figure 6.2. Network structure of an ANFIS employed for bearing diagnosis 105
Figure 6.3. Diagnosis results of the MLP network 108
Figure 6.4. Diagnosis results of the RBF network 109
Figure 6.5. Diagnosis results of the ANFIS network 109
Figure 7.1. Experimental setup 114
Figure 7.2. Recurrent Neural Network (RNN) structure 116
Figure 7.3. Outer race damage Test 1 and Test 3 117
Figure 7.4. Prediction results of schemes 1, 2, and 3 121
Figure 7.5. Prediction results of schemes 4, 5, and 6 122

Figure I.1. Contact of two bodies with curved surfaces……..……..127
Figure I.2. Line contact between roller and raceways…….129
Figure II.1. Probability distribution of normal bearing vibration data……130

List of Tables

Table 2.1. Specifications of ball bearing SKF6204 18
Table 3.1. Specification of ball and roller bearing..... 44
Table 4.1. Effect of imbalance on the correlation dimension (simulation results) 69
Table 4.2. Effect of misalignment on the correlation dimension..... 70
Table 5.1. Replacement criteria for calculating the largest Lyapunov exponent..... 82
Table 5.2. Comparison among different techniques 90
Table 6.1. Bearing condition monitoring data sets 107
Table 6.2. Diagnosis results of proposed neural networks 110
Table 7.1. Test descriptions and conditions..... 118
Table 7.2. Prognostic schemes..... 120
Table 7.3. Comparison of prognosis performance..... 123
Table 7.4. Overall prognostic efficiency..... 124

Chapter 1

Introduction

1.1 Overview

Rotary machines are recognized as crucial equipment in power stations, petrochemical plants, and automotive industry that require precise and efficient performance. Bearings are the most widely used mechanical parts in rotational equipment and are primary cause of breakdowns in machines. Such malfunctions can lead to costly shutdowns, lapses in production, and even human casualties. To minimize machine downtimes, a sensitive and robust monitoring system is needed to detect faults in their early stages and to provide warnings of possible malfunctions. Such a monitoring system can reduce maintenance costs, avoid catastrophic failures and increase machine availability. To develop an effective diagnostic and prognostic system, a comprehensive understanding of the bearing behavior is required.

Typically, a rolling element bearing consists of two rings with a set of elements running in the tracks between the rings. The standard shapes of a rolling element include ball, cylindrical roller, tapered roller, needle, and barrel roller, encased in a cage that provides equal spacing and prevents internal strikes.

Even a normally loaded, properly lubricated, and correctly assembled bearing fails due to material fatigue after a certain running time. This is referred as fatigue life of a bearing, and is calculated by the common formula

$$L_{10} = \left(\frac{C}{P} \right)^n \qquad [\text{million revolution}] \tag{1.1}$$

For a point contact such as a ball, $n = 3$, and for roller bearings, $n = 10/3$. P denotes the equivalent dynamic load, depending on geometry of the bearing, and the radial and thrust load components [1]. Regarding the ISO standard [2], dynamic load rating C corresponds to the constant load, where 90% of the identical test bearings reach a fatigue life of one million revolutions.

The typical fatigue life of a bearing can be significantly shortened due to manufacturing defects, improper handling and installation, or lack of lubrication. The result is either a localized or a distributed defect in the components of the bearings. The principal bearing faults and their causes are briefly discussed in the following.

- **Wear**

The most common source of bearing failure is wear. It can occur as a result of material fatigue in a bearing's components. Wear can also happen because of entering foreign particles such as dust, sand, or metal shavings due to improper sealing or contaminated lubricant. In the early stages, wear is usually a localized fault that is easily distributed throughout a bearing's components.

- **Plastic Deformation**

A bearing, subjected to excessive load, high amplitude impact, or shock while stationary, can be damaged by plastic deformation at the contact surface. This type of fault is usually localized.

- **Corrosion**

Water entering due to sealing failure and a corrosive environment are two reasons for bearing corrosion damage. In a corroded bearing, the rust particles, worn off by the rolling elements, have an abrasive effect and generate wear. This type of damage commonly occurs as a distributed fault.

- **Brinelling**

Brinell indentation marks appear in the bearing raceways from different sources. Indentation can result from plastic deformation, created by excessive loads. Machine vibration, hammering during installation, and accidental falls can also cause Brinell indentation. The other cause of Brinell marks is the passage of electric current due to motor leakage. Premature Brinelling damage is a localized defect, but can affect all the components.

- **Improper Mounting**

The most frequent mounting problem is excessive preloading due to improper tolerances which are recognized by track formation in raceways. Misaligned seats and excessive thrust loads can cause localized flaking. The improper use of a hammer or puller in mounting and dismounting a bearing can instigate lip fracture or permanent indentation in raceways.

- **Design and Manufacturing Problems**

Inadequate support, a loose fit, an excessive load applied by a set screw, improper load distribution, wavy raceways, and unequal rolling element size, all can result in localized wear.

- **Improper lubrication**

A lubrication problem can cause small and large welding areas or deep scratches in the lip and roller face area. Also color changes in the bearing components are a sign of lubrication problem.

1.2 Bearing Condition Monitoring Techniques

Typically, the previous defects mostly arise during the operation of a bearing. Therefore, the detection of these defects at an early stage without machine disassembly is pivotal for condition monitoring, quality inspection, and predictive maintenance. Various

methods are used for the diagnosis of bearing defects. The methods are broadly classified as acoustic measurements, current and temperature monitoring, wear debris detection, and vibration analysis.

- **Acoustic Measurement**

The most effective acoustic-based bearing health monitoring is acoustic emission. It is a transient impulse generated by the rapid release of strain energy in solid material under mechanical or thermal stress. The detection of cracks is the prime application of acoustic emission; therefore, this technique can be used as a tool for condition monitoring of bearing faults and shaft cracks. The measurement of a machine's sound can also be employed for detecting defects in bearings. Typically, the accuracy of these methods depends on sound pressure and sound intensity data.

- **Temperature Monitoring**

Bearing distributed defects generate excessive heat in the rotating components. Monitoring the temperature of a bearing housing or lubricant is the simplest method for fault detection in rotary machines.

- **Electrical Motor Current Monitoring**

The operating conditions of a machine can be monitored by analyzing the spectrum of the motor current. The changes in the electric background noise are associated with the changes in the mechanical components of the machine; therefore, fault signatures can be detected by motor current signal processing techniques.

- **Wear Debris Analysis**

In this method, the presence of metallic particles in the lubricant is detected by sensitive sensors. Furthermore, the spectrographic analysis of the different metallic elements in the lubricant can facilitate the location of the fault.

- **Vibration Measurement**

Since the abnormal vibration of rotary machines is the first sensory effect of rotary component failure, vibration analysis is widely employed in the industry. The fault vibration signal generated by the interaction between a damaged area and a rolling surface occurs regardless of the defect type. Consequently, a vibration analysis can be employed for the diagnosis of all types of faults, either localized or distributed. Furthermore, low-cost sensors, accurate results, simple setups, specific information on the damage location, and comparable rates of damage are other benefits of the vibration measurement method.

1.3 Vibration Based Condition Monitoring

Even a fault-free bearing generates vibration; thus, studying the base-line behavior of bearing oscillation is necessary to find the abnormality in the damaged vibration signature. The principal source of vibration in roller element bearings is varying compliance, caused by the continuous change of position and the number of load carrying elements. Based on this phenomenon, different models have been proposed to represent the periodic vibration of bearings [3, 4, 5]. The periodic vibration of bearings can be transformed to chaotic through a quasi-periodic [6], period doubling, and intermittency routes [7]. Recently, some research has been reported in the literature, regarding possible relation between chaotic parameters and bearing faults. For example, it has been shown that the correlation integral of bearing vibration data [8, 9], and the modified Poincare map of vibration data [10] are potential features for fault diagnosis.

The majority of the research on the diagnosis and prognosis of bearings is based on signal processing techniques, independent of bearing vibration characteristics. In these works, first a localized or distributed defect is created on a bearing by means of grinding, acid etching, drilling, overloading, or over speeding to intentionally introduce defects in the bearing components. After a vibration signal is measured usually, by accelerometers,

different signal processing techniques are employed to extract the fault sensitive features to serve as the monitoring indices. This procedure is quite similar among the published literature. The reported signal processing methods are categorized as time domain, frequency domain, and time-frequency domain. These techniques are not totally independent, and in many cases, they are complementary to each other.

Time domain analysis has been widely employed. Successful results of Root Mean Square (RMS) [11, 12], Kurtosis [13, 14, 15, 16], skewness, peak value [17], Crest Factor (CF) [18], and synchronous averaging [19, 31] have been reported in the low frequency range of <5 kHz. Band pass filtering has also been conducted in the time domain, it is based on the fact that the strike between the damage and the rotating component can excite high frequency resonances (10-100 kHz). The generated energy from this impact is not sufficient to excite the entire rotor's assembly, but is enough to excite vibration sensor resonance. Monitoring the vibration amplitude at the resonant band pass filtered frequency is the principle of the shock pulse method [17, 20, 21, 22]. It is implemented in shock pulse meters which are the most accepted diagnostic instrument in the industry. Time domain analysis has the advantage of simple calculations, straightforward signal pre-processing, and speed independency. However, insensitivity to early stage faults and deeply distributed defects are drawbacks of this approach.

Perhaps, frequency domain, also called spectral analysis, is the most reported signal processing method for bearing diagnosis. Each bearing component has a characteristic frequency, which is calculated from the kinematics of the rotating parts. Monitoring these frequencies or their harmonics at a low frequency range (<5 kHz) has been successful in bearing diagnosis [13, 23, 24]; however, some research draws attention to the weakness of this method for detecting small defects [25]. To decrease the effect of the noise level and frequency side bands, some researchers have adopted the amplitude demodulated or enveloped signal. The spectral analysis of a low and/or high frequency range enveloped signal is repeatedly reported as an efficient method for bearing diagnosis [26, 27, 28, 29, 32, 34, 35, 36]. A number of frequency domain features, based on simple or complex

signal processing methods such as power cepstrum [11], adaptive noise cancellation [30, 33], and denoising [37], are also proposed for bearing diagnosis. The frequency domain approach is sensitive and robust to detect bearing defects and to identify the localized damage location. However, the accuracy of this method highly depends on the bearing dimensions and rotational speed. In addition, all the frequency domain methods require an intelligent selection of the frequency band in order to be effective.

Time-frequency methods can provide useful information regarding energy distribution over frequency bands. In signal processing, a number of time-frequency analysis methods such as the short time Fourier transform, Wigner-Ville distribution, wavelet transforms, and basis pursuit [39] have been proposed. Due to its flexibility and computational benefits, wavelet transform is widely used for bearing diagnosis and prognosis [38, 40, 41, 43, 44, 45, 46]. Some researchers have suggested the use of diagnostic features, obtained from wavelet decompositions [42], and wavelet packets [47, 48].

In many cases, particularly in speed and load variable systems, a simple inspection of the monitoring index does not provide reliable information regarding the condition of the machine. Therefore, there is still a demand for reliable, flexible, and automated procedures for the diagnosis of such systems. Artificial Neural Networks (ANNs) with their flexibility and learning capabilities are the best candidates for a decision-making engine of a diagnostic scheme. The input to such a scheme is monitoring indices obtained from signal processing, and the output corresponds to the level of the bearing's health. Different kinds of ANNs are proposed for bearing condition monitoring with time and/or frequency domain features. The multi-layer feed-forward [49, 50, 51, 54], radial basis function [52], wavelet neural networks [53], adaptive resonance theory network [54], and Adaptive Neuro-Fuzzy Inference System (ANFIS) [55, 77] are among the most referenced networks in bearing condition monitoring. Also, other types of intelligent systems such as automated intelligent systems [56, 57], pattern recognition models [58, 60, 66], cascade correlation algorithms [59], automated fuzzy inference [61], support

vector machine [62, 63], and genetic algorithms [64, 65] have also been employed, to extract the condition of the bearing.

Bearing prognosis refers to the adoption of current and previous monitoring indices to forecast machine's future states. Bearing prognostic methods are either model-based life perdition, or intelligent systems. The first category focuses on a model to predict the fatigue life of a bearing [67-73], whereas the second category involves statistical or intelligent systems to estimates the future state of a bearing. A few prognostic methods are recently proposed based on Recurrent Neural Network (RNNs) [74], Multi Layer Perceptron (MLP) [75], and self organizing map [76] with limited applications.

1.4 Motivation and Objectives

So far, vibration-based condition monitoring of a rolling element bearing has been mostly studied from a signal processing point of view. Very little attention has been paid to the effect of the fault on the bearing's vibration behavior. Therefore, the first step in successfully implementing of bearing health monitoring is to establish the base-line behavior of a healthy bearing. Furthermore, although a number of rotary machines operate under variable speed and load conditions, very few researchers have proposed robust techniques for the fault diagnosis and prognosis of such systems.

In this thesis, the nonlinear dynamics of rolling element bearings are initially studied. A comprehensive analytical study is conducted to investigate the different categories of rolling element vibration and the characteristics of each class. The results of the analytical studies are validated by numerical simulations and experiments.

In the next step, the effect of the bearing damage on the vibration signature is investigated. This study pinpoints the potential of the proposed vibration indices, normalized information entropy, correlation dimension, and the maximum of approximate coefficients of wavelet for fault diagnosis. Their sensitivity and robustness are then compared with those of well-accepted fault detection techniques by testing

various damage types and sizes. Based on the comparison, three fault features, with the least dependency on speed and load conditions, are selected as the bearing monitoring indices.

Next, a decision-making scheme, consisting of a neural network is suggested to map the monitoring indices into the bearing's health under variable speed conditions. The output of the neural system identifies the severity of bearing's damage. Finally, a scheme for estimating the future state of a bearing's condition for various speeds and loads is suggested. The proposed prognostic structure consists of monitoring indices, a forecasting algorithm, and decision-making rules. The performance of the diagnostic and prognosis schemes is studied under variable testing conditions.

1.5 Thesis Outline

This thesis consists of eight chapters. Chapter 2 consists of a series of analytical and numerical studies of the bearing's nonlinear dynamic model. In this section, different categories of bearing vibration and the effect of the internal clearance are studied. In Chapter 3, the results of the numerical simulations of the model are proven to be in good agreement with the results of the experiments. Chapter 4 presents quantifiers to measure the chaotic behavior of a bearing. The stability of these measures: Lyapunov exponent, correlation dimension, and information entropy, are investigated at various rotational speeds. The sensitivity and robustness of the novel chaotic-based indicators are compared with that of well-accepted monitoring techniques in Chapter 5.

A decision-making scheme, a neuro-fuzzy inference network, is employed in Chapter 6 to map the fault features to a bearing's health condition. Chapter 7 presents a novel scheme for estimating the future state of a bearing's condition over a range of speeds and loads. Lastly, Chapter 8 provides concluding remarks and recommendations for future research.

Chapter 2

Analytical Investigation of Bearing Vibration

So far, the vibration-based condition monitoring of bearings has been examined from the signal processing perspective without serious attention to the dynamics of bearing vibration. The first step in the successful implementation of a bearing condition monitoring system is to investigate the fundamentals of a healthy bearing's oscillations. Fault-free bearings generate vibration due to the finite number of balls carrying the external radial load. The fundamental problem, to describe the vibration of rolling element bearings, has been identified, by Gustafsson and Tallian [3] and Sunnersjo [4], as the varying compliance of the rolling elements. These studies have demonstrated that the compliance variation is periodic with a period that corresponds to the ball passage frequency. Tallian and Gustafsson [78] have been the first to explore the role of a bearing's internal clearance on vibration. Their simulation results indicate that larger internal clearances increase the amplitude of bearing vibration, which is also analytically confirmed in this chapter. Also Wardel and Poon [79] have experimentally verified that an increase in the internal clearance raises the level of vibration in rolling element bearings.

Meyer et al. [5] first proposed a model for bearing vibration, based on the linear spring characteristics of the balls under axial (thrust) loads. Tandon and Choudhury have [80, 81] developed a three Degree-of-Freedom (3 DOF) model to predict and characterize a bearing's response to inner race, rolling element, and outer race defects under radial loads. The authors have suggested that the stiffness can be assumed, due to small variations of the rotor displacement under dynamic forces to be linear. Akturk et al. [82, 83] have presented a nonlinear 3 DOF model, based on the Hertzian contact theory.

Numerical simulations of the model confirm that increasing the preload and/or the number of balls reduces the vibration amplitude. In a series of papers, Tamura and co-workers [84, 85, 86] have numerically analyzed the stiffness characteristics and vibration of self-aligning ball bearings according to the Hertzian contact model for bearings with two, three, four, and a large number of rollers. Harsha et al. [87, 88, 89] have numerically investigated the effects of surface waviness and the number of balls on the generated vibration. The authors have verified that the frequency of vibration, due to surface irregularities, depends on the order of the waviness.

Gad et al. [90] have explored the appearance of chaotic-like motions by using a nonlinear model, also based on the Hertzian contact. Their numerical simulations prove that the rotor-ball bearing system exhibits harmonic, superharmonic, subharmonic, beat, and chaotic oscillations. Mevel et al. [6] have used numerical simulations of a nonlinear model to study the dynamics of ball bearing systems. For a lightly loaded ball bearing, the authors have found a period-doubling route to chaos, when the ball passage frequency is near the first natural frequency of the system, and a quasi-periodic route to chaos when the ball passage frequency approaches the second natural frequency. To determine the effect of the internal clearance in ball bearings, Tiwari et al. [91] have reported an increase in the clearance results in wider chaotic regions. This fact is also observed in the present work and detailed in the chaos map in Figure 2.18. Their numerical experiments also relate that a decrease in the clearance increases the linear behavior of the system. This phenomenon is analytically studied in this work; also, a closed form solution for the vibration of bearings within a small range of radial clearance is presented.

So far, very little research has been reported on the analytical study of bearing vibration models. Furthermore, the possible relation between the various vibration categories and the bearing parameters has not been discussed. This chapter presents analytical studies on a nonlinear 2 DOF model by applying the generalized averaging method. The investigation of the behavior of the equilibrium points in this work reveals the underlying source of various vibration regimes in a bearing. This research identifies different

categories of bearing vibrations and demonstrates the effect of the internal clearance on the vibration signature.

2.1 System Modeling

In general, a rotary machine can be simplified as a model of a rotating disc, carried by a central shaft, and supported by two flexible bearings represented by the axis-symmetric springs and dashpots in Figure 2.1. In a rotor, supported by rolling element bearings, few of the balls or rollers carry the dynamic load, and their elastic deformation in the load zone provides the stiffness of the system. When the machine rotates at a slow speed, the inertia force and viscous damping are negligible, and the decisive force exerted on the system is the rotor static weight. In this case, the total stiffness of the system varies periodically at a frequency equal to that of the rolling element passage. At higher speeds, the inertia and damping of the rotor affects the motion of the rotating ring in the vertical and horizontal directions, causing a nonlinear, coupled, and varying stiffness.

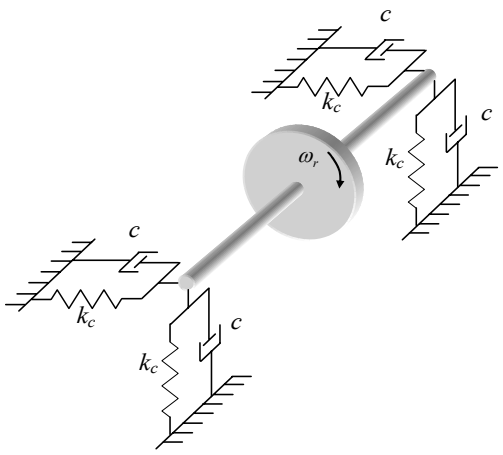

Figure 2.1. Simplified model of a rotor supported by two bearings

To investigate the dynamics of ball bearings as a part of a rotor assembly, the system is modeled as a mass-damper-spring system, where the rotor mass is lumped at the centre of the inner ring, and supported by a set of identical parallel nonlinear springs representing the balls. This 2 DOF model, Figure 2.2, considers the inertia of the balls to be negligible,

compared with that of the rotor. The summation of the restoring forces of the balls in the load zone provides the excitation force, applied to the mass.

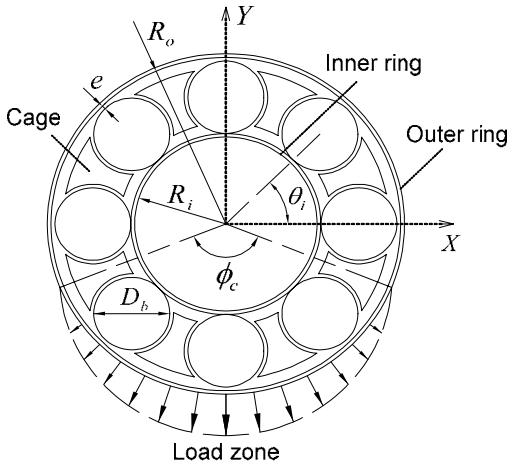

Figure 2.2. Rolling element bearing 2 DOF model

The following assumptions are made regarding the model:

- The shaft is held at the centre of the inner ring, and the outer ring is stationary.
- The only external force is the weight of the rotor, and the raceways are assumed to be fault-free.
- The geometric parameters of the bearing: inner and outer rings radii R_i, R_o, internal clearance *e*, and ball diameter D_b are considered to be constant during operation.

In this model, the balls are equally spaced around the rotor by a cage and the angular location of the ith ball θ_i, is given by

$$\theta_i = \omega t + \frac{2\pi i}{N} \tag{2.1}$$

where N is the number of balls, and the cage speed, ω, is proportional to the shaft speed ω_s according to

$$\omega = \frac{R_i \omega_s}{R_i + R_o} \tag{2.2}$$

The displacement of the inner ring from its centre causes a small deformation δ_i, on each rolling element. The radial deformation of each roller is geometrically derived in terms of

the angular location of each element, the location of inner ring centre (x, y), and the clearance between the rolling element and each raceway *e*, as illustrated in Figure 2.3.

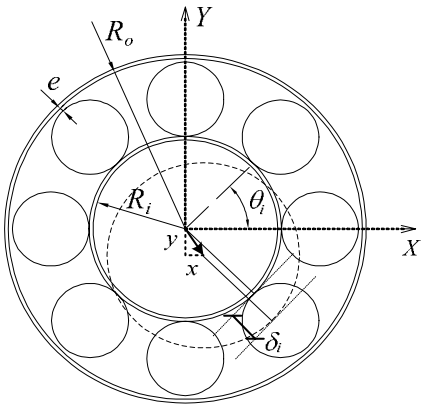

Figure 2.3. Radial deformation of rolling element in bearing assembly

$$\delta_i = x\cos\theta_i + y\sin\theta_i - e \tag{2.3}$$

If equation (2.1) is substituted into(2.3), the radial deformation of each ball is given by

$$\delta_i = x\cos\left(\omega t + \frac{2\pi i}{N}\right) + y\sin\left(\omega t + \frac{2\pi i}{N}\right) - e \tag{2.4}$$

The restoring force F_i, associated with each ball located in the load zone, is calculated based on the Hertzian contact theory such that

$$F_i = k\delta_i^n \tag{2.5}$$

The power n, depends on the rolling element shape; for ball elements, n = 1.5, and cylindrical rollers, n = 1.08. The derivations of the contact stiffness *k*, for the ball and the cylindrical roller bearing are detailed in Appendix I.

The deformation force is generated when the rollers are under compression; in this case, they exhibit a nonlinear stiffness. When the radial displacement of the inner ring, relative to the stationary outer ring, is negative, no compression force is generated. Hence, the total deformation force, exerted on the inner ring, is the summation of the compression forces of each rolling element in the vertical and horizontal directions. These equations are expressed in the following coupled format:

$$F_x = k\sum_{i=1}^{N-1}\left(x\cos\theta_i + y\sin\theta_i - e\right)^n \cos\theta_i H\left(x\cos\theta_i + y\sin\theta_i - e\right)$$
$$F_y = k\sum_{i=1}^{N-1}\left(x\cos\theta_i + y\sin\theta_i - e\right)^n \sin\left(\omega t + \frac{2\pi i}{N}\right) H\left(x\cos\theta_i + y\sin\theta_i - e\right) \quad (2.6)$$

where n depends on the shape of the rolling element. When the expression inside the bracket of the Heaviside step function, ($H(x) = 1$ when $x > 0$, and $H(x) = 0$ when $x \le 0$) is greater than zero, the relevant roller is under compression and applies force on the inner race, unless the roller is located outside the loading zone without any contribution in the resultant force. If the bearing contains N_c elements in the load zone, the Heaviside function *H,* can be eliminated from(2.6). Consequently, the governing equations of the motion in the rotor-bearing system are expressed as follows:

$$m\ddot{x} + c\dot{x} + k\sum_{i=0}^{N_c-1}\left(x\cos\left(\omega t + \frac{2\pi i}{N}\right) + y\sin\left(\omega t + \frac{2\pi i}{N}\right) - e\right)^n \cos\left(\omega t + \frac{2\pi i}{N}\right) = \sum Q_x$$
$$m\ddot{y} + c\dot{y} + k\sum_{i=0}^{N_c-1}\left(x\cos\left(\omega t + \frac{2\pi i}{N}\right) + y\sin\left(\omega t + \frac{2\pi i}{N}\right) - e\right)^n \sin\left(\omega t + \frac{2\pi i}{N}\right) = W + \sum Q_y \quad (2.7)$$

The external force $\sum Q$, can be the effect of imbalance, misalignment, or internal forces that are generated due to the wavy surfaces or damage. The rolling element bearing exhibits damping as well as stiffness. Typically, the internal damping *c*, arises from the lubricant with a minor effect of friction at the points of contact. The other sources of internal force in bearings are centrifugal and gyroscopic effects. Since the mass of the rolling element is very small, compared with that of the rotor's mass *m*, the centrifugal force and the gyroscopic force are negligible.

To solve equations(2.7), the number of balls in the load zone N_c and the location of the equilibrium points of the rotor are determined analytically by employing a Taylor-series expansion of the restoring force of the element in the load zone, (2.7) is transformed into a set of coupled nonlinear ordinary differential equations with periodic coefficients. A closed-form solution of this system of equations is then obtained by the generalized method of averaging.

2.2 Load Distribution Angle

In the ball bearings, the rolling elements transmit the load from one ring to the other. The radial force is consistently distributed over a number of balls which are compressed between the inner and outer rings. Therefore, the radial displacement of the rotor is positive *only* for the balls within the load zone, and can be expressed as follows:

$$\begin{aligned} \delta_i > 0 \quad & \text{i}^{\text{th}} \text{ ball inside the load zone} \\ \delta_i \le 0 \quad & \text{i}^{\text{th}} \text{ ball outside the load zone} \end{aligned} \tag{2.8}$$

By applying the polar transformation, $x = r_t \cos\alpha_t, y = r_t \sin\alpha_t$, to the location of the inner ring centre (Figure 2.4), equation (2.4) can be transformed in the following criteria for the balls in the load zone:

$$\cos\left(\omega t + \frac{2\pi i}{N} - \alpha_t\right) \ge \frac{e}{r_t} \tag{2.9}$$

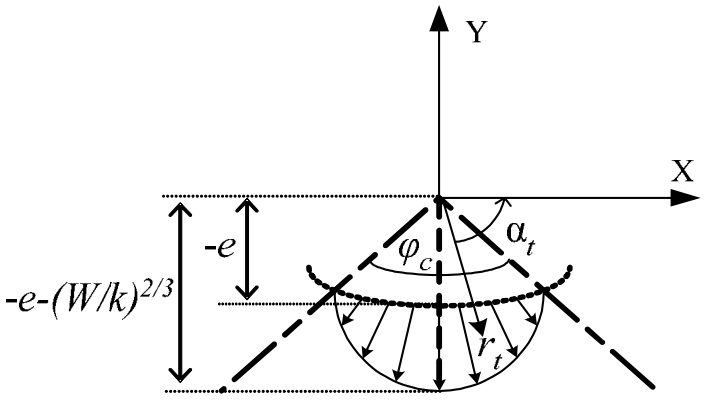

Figure 2.4. Load distribution angle

The maximum value of r_t occurs when a single ball carries the weight of the rotor. In this case, considering Hertzian contact theory under a quasi-static condition, $\omega \approx 0$, results in

$$\max(r_t) = -e - \left(\frac{W}{k}\right)^{\frac{2}{3}} \tag{2.10}$$

Equations (2.9) and (2.10) yield the load distribution angle, φ_c, by computing

$$\phi_c = 2\cos^{-1}\frac{e}{e + \left(W/k\right)^{2/3}} \tag{2.11}$$

Consequently, the number of balls inside the load zone that contribute to the forcing term is derived from

$$N_c = \frac{N}{\pi}\cos^{-1}\frac{e}{e+\left(W/k\right)^{2/3}} \tag{2.12}$$

The number of balls, N_c, in the load zone depends on the internal clearance, radial force, and ball stiffness. In addition, the location and *number* of balls inside the load zone changes with time, thereby changing the number of balls contributing to the system stiffness. This is the underlying source of the vibration and the time varying nature of the system.

2.3 Equilibrium Points

The equilibrium points of the shaft, denoted (x_e, y_e), are any set of (x, y) for which the time derivatives in (2.7) are identically zero. Therefore, for a fault-free ball bearing, mounted in an ideally balanced rotor, the equilibrium points satisfy the following coupled equations:

$$\begin{aligned}
&\sum_{i=0}^{N_c-1}\left(x\cos\left(\omega t+\frac{2\pi i}{N}\right)+y\sin\left(\omega t+\frac{2\pi i}{N}\right)-e\right)^{1.5}\cos\left(\omega t+\frac{2\pi i}{N}\right)=0\\
&\sum_{i=0}^{N_c-1}\left(x\cos\left(\omega t+\frac{2\pi i}{N}\right)+y\sin\left(\omega t+\frac{2\pi i}{N}\right)-e\right)^{1.5}\sin\left(\omega t+\frac{2\pi i}{N}\right)=\frac{W}{k}
\end{aligned} \tag{2.13}$$

The location of the equilibrium points depends on the clearance, radial force, and the number of balls in the load zone. Equation (2.13) is solved numerically to obtain the equilibrium points of the system. The maximum number of balls, inside the load zone $N_c = N/2$, occurs for the zero internal clearance, $e = 0$. In a quasi-static condition ($\omega \approx 0$), applying the polar transformation, $x_e = r_e\cos\varphi_e$ and $y_e = r_e\sin\varphi_e$, in (2.13) results in

$$\sum_{i=0}^{\frac{N}{2}-1}\left(r_e\cos\left(\varphi_e-\frac{2\pi i}{N}\right)\right)^{1.5}\cos\left(\frac{2\pi i}{N}\right)=0$$
$$\sum_{i=0}^{\frac{N}{2}-1}\left(r_e\cos\left(\varphi_e-\frac{2\pi i}{N}\right)\right)^{1.5}\sin\left(\frac{2\pi i}{N}\right)=\frac{W}{k} \tag{2.14}$$

In the range of $3\pi/2$ to 2π, it is assumed that $\cos^{1.5}\left(\varphi-\frac{2\pi i}{N}\right)\approx\cos\left(\varphi-\frac{2\pi i}{N}\right)$. The trigonometric combinations transform (2.14) into the following, when N = 8, 12, 16…:

$$\frac{Nr_e^{1.5}\cos\varphi_e}{4}=0 \qquad \text{and} \qquad \frac{Nr_e^{1.5}\sin\varphi_e}{4}=\frac{W}{k} \tag{2.15}$$

This results in the coordination of the equilibrium points for a zero internal clearance, expressed as

$$\left(x_e,y_e\right)\Big|_{e=0}=\left(0,-\left(4W/Nk\right)^{2/3}\right) \tag{2.16}$$

To study the effect of the internal clearance on the position of the equilibrium points, (2.13) is solved numerically for the ball bearing SKF6204, with the specifications listed in Table 2.1. First, the equilibrium points are obtained under a quasi-static condition, $\omega\approx 0$. For a positive clearance, the number of balls in the load zone is found to vary between four and one depending on the amount of internal clearance. Figure 2.5 reflects the location of the equilibrium points in the *X*-*Y* plane.

Table 2.1. Specifications of ball bearing SKF6204 (www.skf.com)

Ball diameter (mm)	7.938	Race groove radius (mm)	4.1278
Inner race diameter (mm)	25. 5620	Number of balls	8
Outer race diameter (mm)	41.4380	Rotor's weight (N)	23.004
Pitch diameter (mm)	33.5	Stiffness ($N/m^{1.5}$)	9.21×10^9

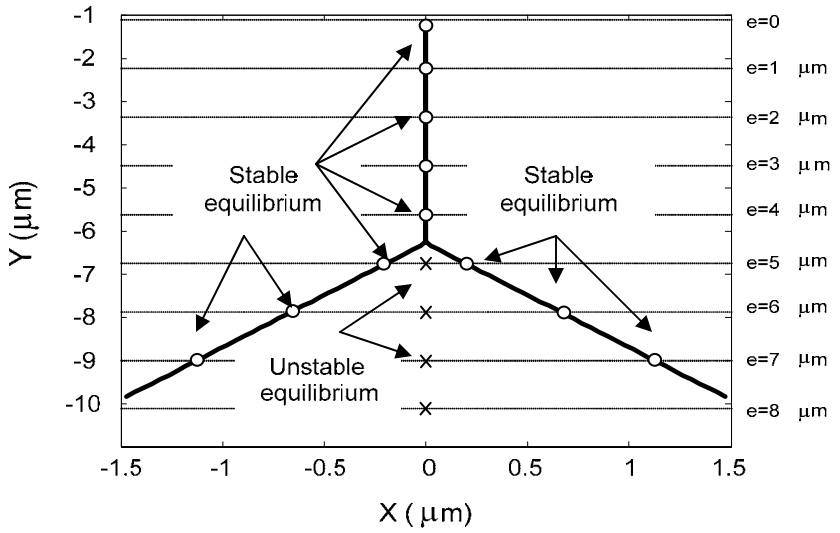

Figure 2.5. Location of the equilibrium points when $\omega \approx 0$ (o: centre, x: saddle)

When the internal clearance is less than $e < 4.5\ \mu m$, the inner ring is in contact with 3 or 4 balls, and a single equilibrium point exists. For clearance values larger than $e > 4.5\ \mu m$, three possible equilibrium points exist. The stability of the equilibrium points are characterized by evaluating the eigenvalues of the Jacobian matrix of (2.7) at the equilibrium point (x_e, y_e) for the ball bearing supporting the balanced rotor as follows:

$$\begin{bmatrix} 0 & 1 & 0 & 0 \\ \frac{-1.5k}{m}\left(x_e\cos\theta_i + y_e\sin\theta_i - e\right)^{0.5}\cos^2\theta_i & \frac{-c}{m} & \frac{-1.5k}{m}\left(x_e\cos\theta_i + y_e\sin\theta_i - e\right)^{0.5}\cos\theta_i\sin\theta_i & 0 \\ 0 & 0 & 0 & 1 \\ \frac{-1.5k}{m}\left(x_e\cos\theta_i + y_e\sin\theta_i - e\right)^{0.5}\cos\theta_i\sin\theta_i & 0 & \frac{-1.5k}{m}\left(x_e\cos\theta_i + y_e\sin\theta_i - e\right)^{0.5}\sin^2\theta_i & \frac{-c}{m} \end{bmatrix} \quad (2.17)$$

When $0 \le e \le 4.5\mu m$, the Jacobian matrix generates four complex eigenvalues with negative real parts, confirming the stability of the equilibrium points. Further, the two-dimensional projection of the system phase history in the *X*-*Y* plane, Figure 2.6 (a), obtained from the long-time integration of (2.7), shows that the equilibrium point in this range is indeed a *centre*. In the range of $e > 4.5\ \mu m$, the eigenvalues of the equilibrium point closest to the *Y*-axis include a pair of real numbers with opposite signs, denoting an unstable *saddle*, as traced in Figure 2.6 (b). The equilibrium points away from the *Y*-axis

produce four eigenvalues with negative real parts, proving the stability of these points. The same arrangement in Figure 2.5 confirms that the inner equilibrium point is a saddle, whereas the outer equilibrium points are centres. The bifurcation point, $e = 4.5\ \mu m$, lying at the intersection of the three zones, generates two real negative and two complex eigenvalues with negative real parts which indicates a marginally stable equilibrium point.

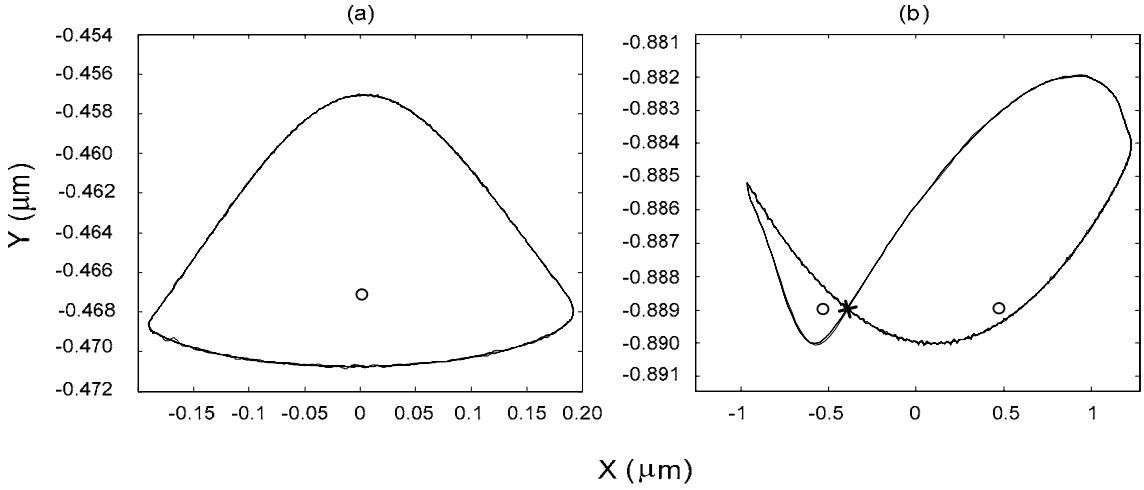

Figure 2.6. Response orbits and equilibrium points at a) *e*=3 μm and (b) *e*=5 μm when $\omega = 800$ rpm; (o : centre, x : saddle)

When $\omega \neq 0$, the solution of (2.13) is obtained at discrete points in time. For the internal clearance values below the bifurcation point, $e = 4.5\ \mu m$, the results are unchanged with a single stable equilibrium point, a centre, located at the *Y*-axis for each value of *e*. When the internal clearance increases and passes the bifurcation point, the solution of (2.13) results in three equilibrium points with similar characteristics to those found in the quasi-static case at *each* point in time. As a result, the locations of the three equilibrium points vary over time with different stretches of the same curve. This curve in Figure 2.7 is symmetric with respect to the Y-axis. As the shaft rotates, the saddle moves on the centre stretch of the curve, while each of the centres move on one of the outer stretches. Figure 2.7 reveals the location of the equilibrium point for a range of internal clearances and a

cage speed of ω = 800 rpm. A distinct curve corresponds to each value of $e > 4.5\ \mu m$. The stability regions of these curves are identified on a map of equilibrium points.

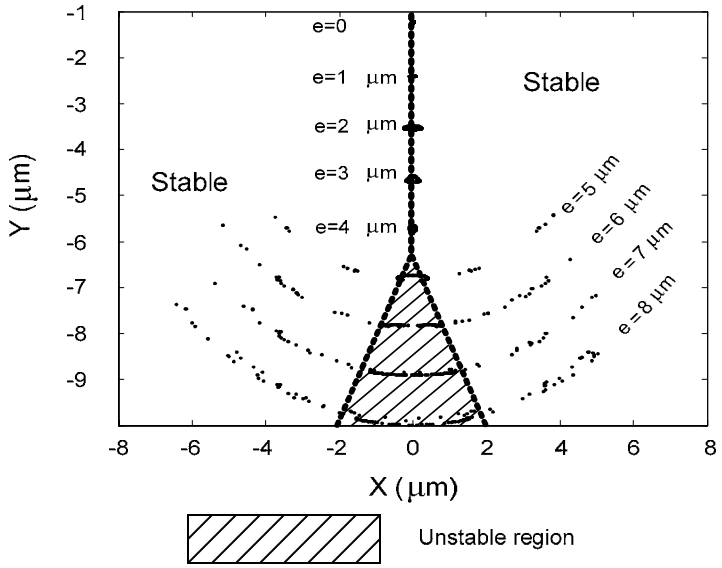

Figure 2.7. Location of the stable and unstable dynamic equilibrium points

This analysis confirms the existence of two qualitatively different types of inner ring vibration, separated by a bifurcation point at $e = 4.5\ \mu m$. For small internal clearances, $e < 4.5\ \mu m$, the vibration is periodic. Beyond the bifurcation point, a "two-well potential" system develops [92] with two symmetric centres away from the *Y*-axis and a saddle close to the *Y*-axis. At a low cage speed, the motion is still periodic and confined to one of the two wells (occurring on one side of the *Y*-axis only). Once the cage speed is high enough to provide the necessary energy, the shaft begins to jump from one well to the other in a chaotic manner; that is, a periodic input at a single frequency, ω, leads to a random like output motions of the shaft with a broad spectrum of frequencies. Furthermore, the locations of the centres and saddles continue to change *randomly* over time as the shaft orbits in the phase space. At higher cage speeds, the chaos disappears and a periodic motion encompasses both wells.

2.4 Analytical Solution

To obtain closed-form expressions of the response of the bearing, the ideal model, (2.7), is simplified for ball bearings by expanding the x- and y-components of the restoring force in the Taylor-series around an equilibrium point. This method is valid only when the motion is restricted to the neighborhood of a single equilibrium point (one well). Figure 2.8 and Figure 2.9 depict the steady state time-response of the original model, compared with first-, second-, and third-order approximations, when the internal clearance is equal to zero and 4 μm, respectively.

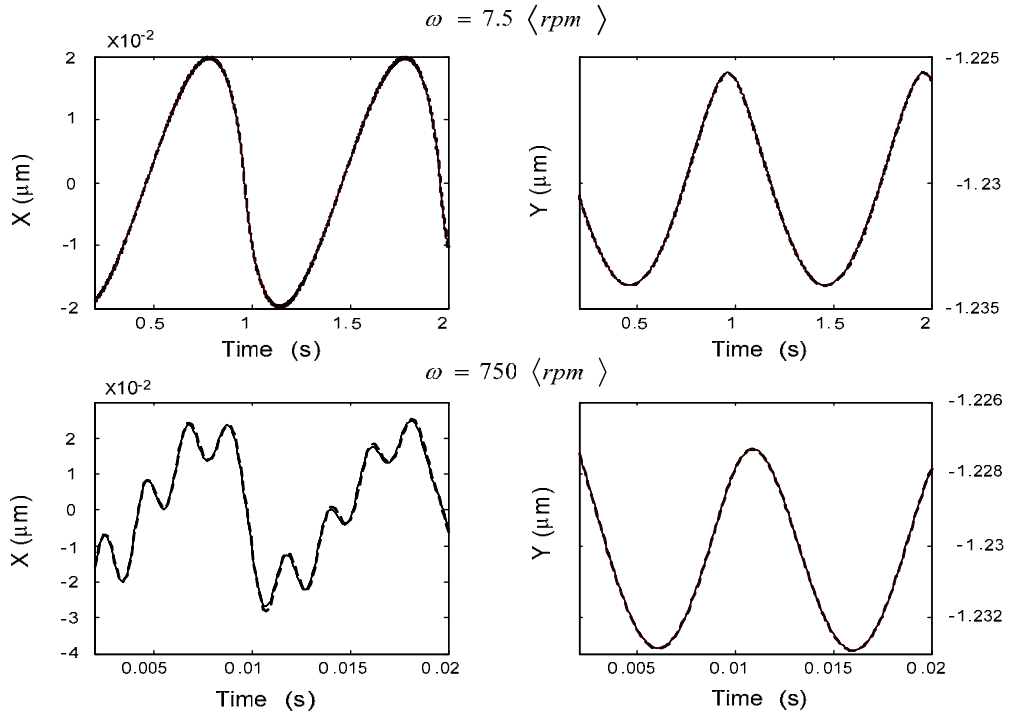

Figure 2.8. Comparison of the original model (solid) and first- (dash), second- (dot), and third- (center) order approximations for e = 0

For zero clearance e = 0, the errors in the response, obtained by using the approximations compared with the original model, are negligible for low, 7.5 rpm, and high, 750 rpm, cage speeds.

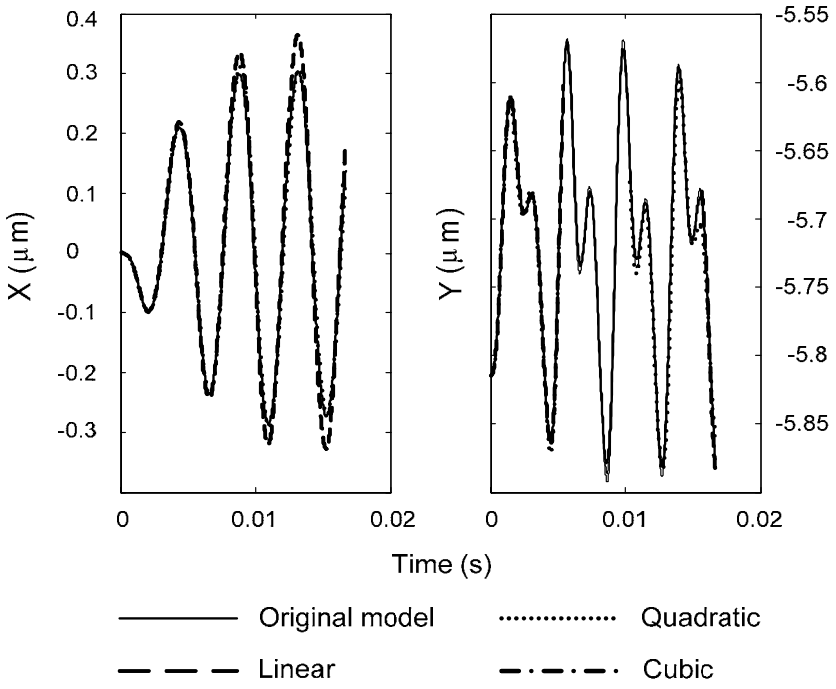

Figure 2.9. Comparison between the original model and first-, second-, and third-order approximations for *e* = 4*μm*

Figure 2.9 conveys that for a higher internal clearance, $e = 4\mu m$, the second and third-order approximations are more accurate than those of the first-order model. However, the steady state error rate of the linear model, even at a high cage speed of 4800 rpm, is less than 0.2%. Therefore, a first-order expansion is suitable for a small internal clearance, $e \le 4.5\mu m$. By employing a first-order expansion, the equations of motion are transformed to

$$\begin{aligned} \ddot{x} + \mu\dot{x} + \alpha_{11}x + \alpha_{12}y &= f_x \\ \ddot{y} + \mu\dot{y} + \alpha_{21}x + \alpha_{22}y &= f_y + \frac{W}{m} \end{aligned} \tag{2.18}$$

where the parameters, $\mu, \alpha_{mn}, f_x,$ and f_y are defined as

$$\begin{aligned} \mu &= c/m \\ f_x &= \frac{k}{m}\sum_{i=0}^{N_c-1}\sqrt{y_e\sin\theta_i - e}\left(0.5y_e\sin\theta_i + e\cos\theta_i\right) \\ f_y &= \frac{k}{m}\sum_{i=0}^{N_c-1}\sqrt{y_e\sin\theta_i - e}\left(0.5y_e\sin^2\theta_i + e\sin\theta_i\right) \end{aligned} \tag{2.19}$$

$$\alpha_{11} = \frac{3k}{2m} \sum_{i=0}^{N_c-1} \sqrt{y_e \sin\theta_i - e}\, \cos^2 \theta_i$$

$$\alpha_{22} = \frac{3k}{2m} \sum_{i=0}^{N_c-1} \sqrt{y_e \sin\theta_i - e}\, \sin^2 \theta_i$$

$$\alpha_{12} = \alpha_{21} = \frac{3k}{2m} \sum_{i=0}^{N_c-1} \sqrt{y_e \sin\theta_i - e}\, \cos\theta_i \sin\theta_i$$

The generalized method of averaging [93] is utilized to solve the coupled linear time-varying differential equations (2.18) for two cases:

Case 1: ball bearings with a zero internal clearance and

Case 2: ball bearings with a small positive radial clearance $0 \le e \le 4.5 \mu m$.

2.4.1 Case 1: Zero Clearance Ball Bearings, e = 0 µm

In this case, the load zone angle is equal to π, and the number of loaded bearing elements is *N*/2. The curve fitting of α_{mn}, f_x, f_y is used to further simplify the equations of motion by replacing the parameters in (2.19) as follows:

$$\begin{aligned}
f_x &\equiv c_x \sin N\omega t \\
f_y &\equiv c_{0y} + c_y \cos N\omega t \\
\alpha_{11} &\equiv \sigma_x^2 + c_{11} \sin^2 N\omega t = \left(\sigma_x^2 + \frac{c_{11}}{2}\right) - \frac{c_{11}}{2} \sin 2N\omega t \\
\alpha_{12} &\equiv c_{12} \sin N\omega t \\
\alpha_{22} &\equiv \sigma_y^2 + c_{22} \cos N\omega t
\end{aligned} \tag{2.20}$$

where

$$\begin{aligned}
\sigma_x &= 1.12312 \sqrt{\frac{k}{m}} \sqrt[4]{y_e} \\
\sigma_y &= 1.66174 \sqrt{\frac{k}{m}} \sqrt[4]{y_e}
\end{aligned} \tag{2.21}$$

and c_{mn} is determined through curve fitting of coefficients $\alpha_{11}, \alpha_{12},$ and α_{22}.

Figure 2.10 illustrates the time-varying parameters of (2.19) and their approximation by applying the curve-fits of (2.20) for one revolution of the cage. The figures confirm that the curve-fitted functions and original parameters are in good agreement.

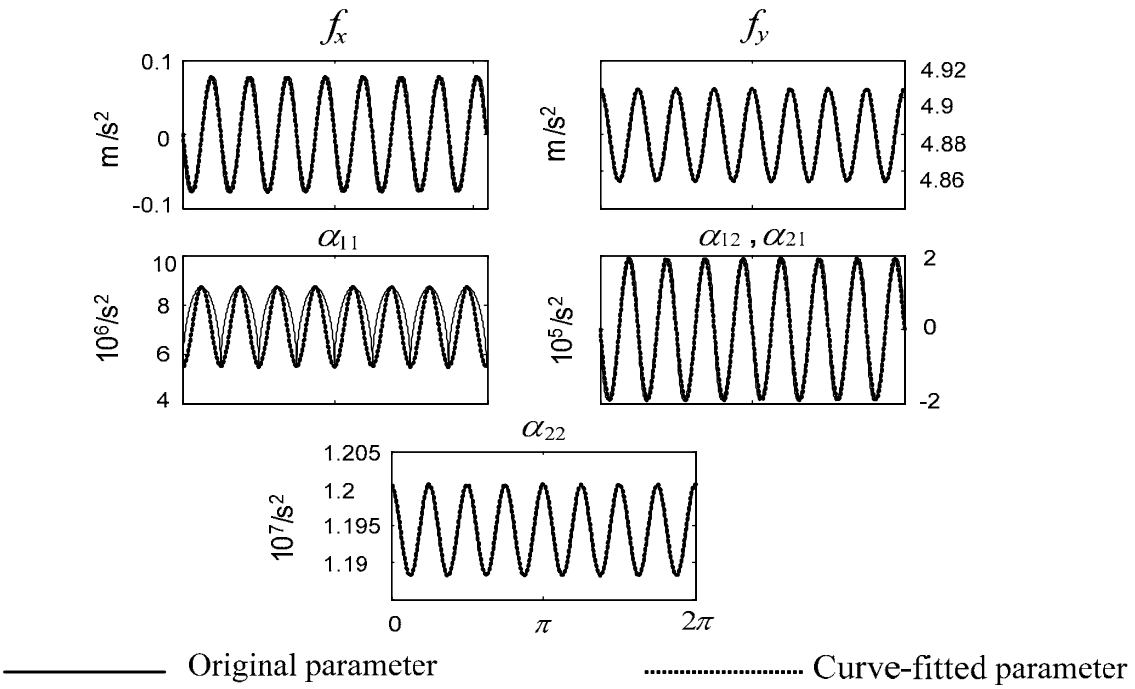

Figure 2.10. Parameters α_{mn}, f_x, f_y and their approximations

The time, *t*, in (2.18) is normalized by the following parameters:

$$\begin{aligned} \omega_1 &= \frac{N\omega}{\sigma_x} \qquad & \omega_2 &= \frac{N\omega}{\sigma_y} \\ t_1 &= \sigma_x t & t_2 &= \sigma_y t \\ \xi_1 &= \frac{\mu}{2\sigma_x} & \xi_2 &= \frac{\mu}{2\sigma_y} \end{aligned} \tag{2.22}$$

Therefore

$$\begin{aligned} \frac{dx}{dt_1} &= \sigma_x \frac{dx}{dt} & \frac{dy}{dt_2} &= \sigma_y \frac{dy}{dt} \\ \frac{d^2x}{dt_1^2} &= \sigma_x^2 \frac{d^2x}{dt^2} & \frac{d^2y}{dt_2^2} &= \sigma_y^2 \frac{d^2y}{dt^2} \end{aligned} \tag{2.23}$$

By substituting the normalized parameters in (2.18)

$$\begin{aligned} &\ddot{x} + 2\xi_1\dot{x} + \left(1 + \frac{c_{11}\sin^2\omega_1 t_1}{\sigma_x^2}\right)x + \left(\frac{c_{12}\cos\omega_1 t_1}{\sigma_x^2}\right)y - \frac{c_x \sin\omega_1 t_1}{\sigma_x^2} = 0 \\ &\ddot{y} + 2\xi_2\dot{y} + \left(\frac{c_{21}\sin\omega_2 t_2}{\sigma_y^2}\right)x + \left(1 + \frac{c_{22}\cos\omega_2 t_2}{\sigma_y^2}\right)y - \frac{c_y\cos\omega_2 t_2}{\sigma_y^2} - \left(\frac{mc_{0y} + W}{m\sigma_y^2}\right) = 0 \end{aligned} \tag{2.24}$$

Using the method of variation of parameters, the solutions of (2.24) are given for two *distinct* situations:

a) The cage speed in the neighbourhood of the fundamental frequency of the horizontal, *X*-direction, motion of the inner race; $N\omega \approx \omega_1$

b) The cage speed in the neighbourhood of the fundamental frequency of the vertical, *Y*-direction, motion of the inner race; $N\omega \approx \omega_2$

By assuming that ω_1 and ω_2 are incommensurate, far from each other, and in the presence of damping, the motions can be decoupled in the horizontal and vertical directions. Consequently, the bearing response is represented by a single DOF in each case such that

$$\begin{aligned} x &= u_1 \cos\left(\omega_1 t_1 + \gamma_1\right) \\ \dot{x} &= -\omega_1 u_1 \sin\left(\omega_1 t_1 + \gamma_1\right) \\ y &= u_2 \cos\left(\omega_2 t_2 + \gamma_2\right) \\ \dot{y} &= -\omega_2 u_2 \sin\left(\omega_2 t_2 + \gamma_2\right) \end{aligned} \tag{2.25}$$

Let $\omega_1 t_1 + \gamma_1 = \varphi$ and $\omega_2 t_2 + \gamma_2 = \psi$, and then the differentiation from (2.25) results in

$$\begin{aligned} \ddot{x} &= \frac{-\dot{u}_1\omega_1 - u_1\omega_1^2 \sin\varphi\cos\varphi}{\sin\varphi} \\ \ddot{y} &= \frac{-\dot{u}_2\omega_2 - u_2\omega_2^2 \sin\psi\cos\psi}{\sin\psi} \end{aligned} \tag{2.26}$$

By substituting (2.25) and (2.26) terms in (2.24), the simplification results in following set of modulation equations:

$$\begin{aligned} \dot{u}_1 &= -u_1\omega_1 \sin\varphi\cos\varphi - 2\xi_1 u_1 \sin^2\varphi + \left(1 + \frac{c_{11}\sin^2\left(\varphi-\gamma_1\right)}{\sigma_x^2}\right)\frac{u_1 \sin\varphi\cos\varphi}{\omega_1} \\ &+ \frac{u_2 c_{12}\cos\left(\varphi-\gamma_1\right)\sin\varphi\cos\psi}{\omega_1\sigma_x^2} - \frac{c_x \sin\left(\varphi-\gamma_1\right)\sin\varphi}{\omega_1\sigma_x^2} \\ \dot{\gamma}_1 &= -\omega_1\cos^2\varphi - 2\xi_1\cos\varphi\sin\varphi + \left(1 + \frac{c_{11}\sin^2\left(\varphi-\gamma_1\right)}{\sigma_x^2}\right)\frac{u_1\cos^2\varphi}{\omega_1} \\ &+ \frac{u_2 c_{12}\cos\left(\varphi-\gamma_1\right)\cos\varphi\cos\psi}{u_1\omega_1\sigma_x^2} - \frac{c_x \sin\left(\varphi-\gamma_1\right)\cos\varphi}{u_1\omega_1\sigma_x^2} \end{aligned} \tag{2.27}$$

and

$$
\begin{aligned}
\dot{u}_2 &= -u_2\omega_2 \sin\psi\cos\psi - 2\xi_2 u_2 \sin^2\psi + \frac{c_{21}\sin\left(\psi-\gamma_2\right)u_1\sin\psi\cos\varphi}{\omega_2\sigma_y^2} \\
&+\left(1+\frac{c_{22}\cos\left(\psi-\gamma_2\right)}{\sigma_y^2}\right)\frac{u_2\sin\psi\cos\psi}{\omega_2} - \frac{c_y\cos\left(\psi-\gamma_2\right)\sin\psi}{\omega_2\sigma_y^2} - \frac{\left(mc_{0y}+W\right)\sin\psi}{m\omega_2\sigma_y^2} \\
\dot{\gamma}_2 &= -\omega_2\cos^2\psi - 2\xi_2\cos\psi\sin\psi + \frac{u_1c_{21}\sin\left(\psi-\gamma_2\right)\cos\psi\cos\varphi}{u_2\omega^*\sigma_y^2} \\
&+\left(1+\frac{c_{22}\cos\left(\psi-\gamma_2\right)}{\sigma_y^2}\right)\frac{\cos^2\psi}{\omega_2} - \frac{c_y\cos\left(\psi-\gamma_2\right)\cos\psi}{u_2\omega_2\sigma_y^2} - \frac{\left(mc_{0y}+W\right)\cos\psi}{m\omega_2u_2\sigma_y^2}
\end{aligned}
\tag{2.28}
$$

With the use of first order averaging method, the right-hand side of (2.27) and (2.28) are averaged for one period over φ and ψ to produce the modulation equations of each case, represented as

$$
\begin{aligned}
\dot{u}_1 &= -\xi_1u_1 - \frac{u_1c_{11}\sin 2\gamma_1}{8\omega_1\sigma_x^2} - \frac{c_x\cos\gamma_1}{2\omega_1\sigma_x^2} \\
\dot{\gamma}_1 &= -\frac{\omega}{2} - \frac{c_{11}\cos 2\gamma_1}{8\omega_1\sigma_x^2} + \frac{c_x\sin\gamma_1}{2u_1\omega_1\sigma_x^2} + \frac{2\sigma_x^2+c_{11}}{4\omega_1\sigma_x^2}
\end{aligned}
\tag{2.29}
$$

and

$$
\begin{aligned}
\dot{u}_2 &= -\xi_2u_2 - \frac{c_y\sin\gamma_2}{2\omega_2\sigma_y^2} \\
\dot{\gamma}_2 &= -\frac{\omega_2}{2} + \frac{1}{2\omega_2} - \frac{c_y\cos\gamma_2}{2u_2\omega_2\sigma_y^2}
\end{aligned}
\tag{2.30}
$$

To study the steady-state response of the system, the fixed points of each set of modulation equations are found by setting the right-hand sides of (2.29) and (2.30) to zero. Therefore,

$$
\begin{aligned}
4c_x\cos\gamma_1 + u_1c_{11}\sin 2\gamma_1 &= -8\omega_1\sigma_x^2\xi_1u_1 \\
4c_x\sin\gamma_1 - u_1c_{11}\cos 2\gamma_1 &= 4u_1\omega_1^2\sigma_x^2 - 2u_1\left(2\sigma_x^2+c_{11}\right)
\end{aligned}
\tag{2.31}
$$

and

$$
\begin{aligned}
c_y\sin\gamma_2 &= -2\omega_2\sigma_y^2\xi_2u_2 \\
c_y\cos\gamma_2 &= -\omega_2^2u_2\sigma_y^2 + u_2\sigma_y^2
\end{aligned}
\tag{2.32}
$$

By considering $c_{11}u_1 << 4c_x$, and squaring and summing both sides of (2.31) and(2.32), the frequency response relations in closed-form can be obtained from

$$u_1 = \frac{c_x}{2\sigma_x^2\sqrt{\left(\xi_1\omega_1\right)^2 + \left(\frac{\omega_1^2}{2} - \frac{2\sigma_x^2 + c_{11}}{4\sigma_x^2}\right)^2}} \tag{2.33}$$

and

$$u_2 = \frac{c_y}{2\sigma_y^2\sqrt{\left(\xi_2\omega_2\right)^2 + \left(\frac{\omega_2^2}{2} - \frac{1}{2}\right)^2}} \tag{2.34}$$

Figure 2.11 compares of the results, obtained by the method of averaging, with those obtained numerically for the frequency response of the horizontal, u_1, and the vertical, u_2, motions of the ball bearing SKF6204. There is good agreement between the approximate responses, resulting from the method of averaging, in both cases. However, the quality of the approximation deteriorates in the neighborhood of the superharmonic resonance of the order two in each case, $\frac{1}{2}\omega_1$ and $\frac{1}{2}\omega_2$, and the quality of the vertical motion approximation deteriorates in the neighborhood of ω_1. The reason for the former discrepancies is the underlying assumption, given in (2.25), that the balls are responding to primary-resonance excitations at $N\omega \approx \omega_1$ or $N\omega \approx \omega_2$. The reason for the latter discrepancy is that the approximate solution,(2.33), ignores the coupling between the horizontal and vertical modes of vibration.

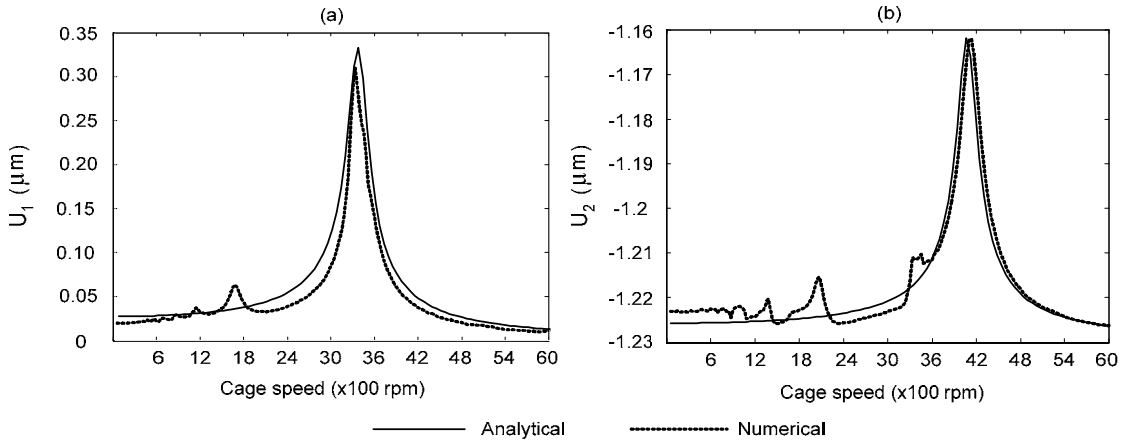

Figure 2.11. The frequency-response curves for the (a) horizontal and (b) vertical motions (*e* = 0 *μm*)

2.4.2 Case 2: Small Clearance Ball Bearing, Clearance Class 1 (0<e<4.5 μm)

In this case, the number of balls in the load zone is derived from (2.12). In order to apply the method of averaging, the common square root term in (2.19) is approximated as follows:

$$\sqrt{y_e \sin\theta_i - e} \approx \frac{y_e}{2\sqrt{e}} \sin^2\theta_i \tag{2.35}$$

Figure 2.12 shows that this approximation is valid within a specific range of the period, 0- 2π, depending on i, and the approximation it is set equal to zero outside that range to match the value of the original function.

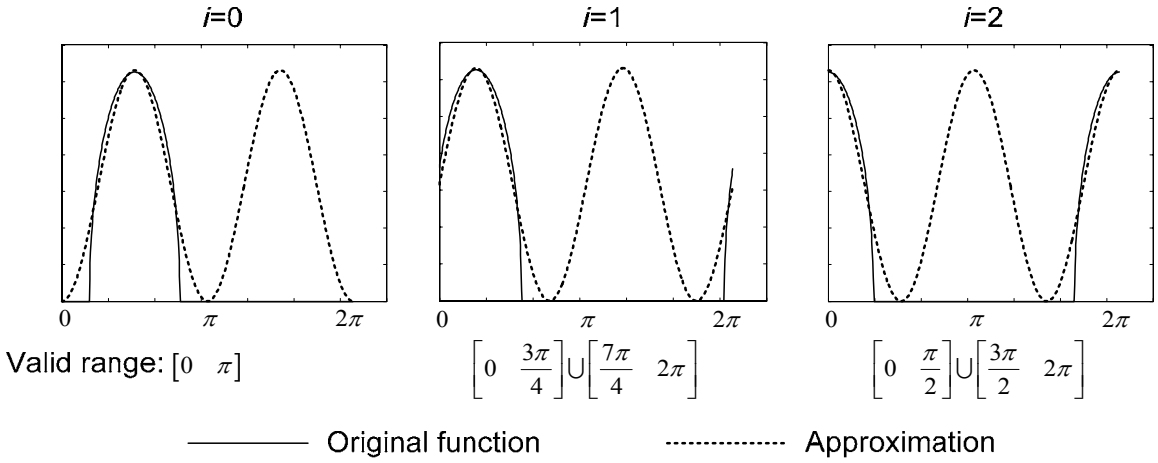

Figure 2.12. Valid ranges of approximation in (2.35)

The governing equations of motion (2.18) are normalized by the following parameters:

$$\begin{aligned} \omega_1 &= \frac{\omega}{\sigma_x} \qquad \omega_2 = \frac{\omega}{\sigma_y} \\ t_1 &= \sigma_x t \qquad t_2 = \sigma_y t \\ \xi_1 &= \frac{\mu}{2\sigma_x} \qquad \xi_2 = \frac{\mu}{2\sigma_y} \end{aligned} \tag{2.36}$$

Therefore,

$$\begin{aligned} \frac{dx}{dt_1} &= \sigma_x \frac{dx}{dt} \qquad \frac{dy}{dt_2} = \sigma_y \frac{dy}{dt} \\ \frac{d^2x}{dt_1^2} &= \sigma_x^2 \frac{d^2x}{dt^2} \qquad \frac{d^2y}{dt_2^2} = \sigma_y^2 \frac{d^2y}{dt^2} \end{aligned} \tag{2.37}$$

By substituting (2.36) and (2.37) in (2.18),

$$\begin{aligned} &\ddot{x} + 2\xi_1 \dot{x} + \left(\frac{3ky_e}{4\sqrt{e}m\sigma_x^2} \sum_{i=0}^{N_c-1} \sin^2\theta_i \cos^2\theta_i \right) x + \left(\frac{3ky_e}{4\sqrt{e}m\sigma_x^2} \sum_{i=0}^{N_c-1} \sin^3\theta_i \cos\theta_i \right) y \\ &- \frac{ky_e}{2\sqrt{e}m\sigma_x^2} \sum_{i=0}^{N_c-1} \sin^2\theta_i \left(0.5 y_e \sin\theta_i \cos\theta_i + e\cos\theta_i \right) = 0 \\ &\ddot{y} + 2\xi_2 \dot{y} + \left(\frac{3ky_e}{4\sqrt{e}m\sigma_y^2} \sum_{i=0}^{N_c-1} \sin^3\theta_i \cos\theta_i \right) x + \left(\frac{3ky_e}{4\sqrt{e}m\sigma_y^2} \sum_{i=0}^{N_c-1} \sin^4\theta_i \right) y \\ &- \frac{ky_e}{2\sqrt{e}m\sigma_y^2} \sum_{i=0}^{N_c-1} \sin^2\theta_i \left(0.5 y_e \sin^2\theta_i + e\sin\theta_i \right) = \frac{W}{m} \end{aligned} \tag{2.38}$$

Then the solutions of (2.38) are found for two distinct cases:

a) The cage speed in the neighborhood of the fundamental frequency of the inner race *X*-direction motions $N\omega \approx \omega_1$

b) The cage speed in the neighborhood of the fundamental frequency of the inner race *Y*-direction motions $N\omega \approx \omega_2$

By assuming that ω_1 and ω_2 are incommensurate, far from each other, and in the presence of damping, the motions in the horizontal and vertical directions are decoupled and the single-mode approximations are

$$
\begin{aligned}
x &= u_1 \cos\left(\omega_1 t_1 + \gamma_1\right) \\
\dot{x} &= -\omega_1 u_1 \sin\left(\omega_1 t_1 + \gamma_1\right) \\
y &= u_2 \cos\left(\omega_2 t_2 + \gamma_2\right) \\
\dot{y} &= -\omega_2 u_2 \sin\left(\omega_2 t_2 + \gamma_2\right)
\end{aligned}
\tag{2.39}
$$

As a result, the bearing response can be represented by using a single DOF in each case. By choosing $\omega_1 t_1 + \gamma_1 = \varphi$ and $\omega_2 t_2 + \gamma_2 = \psi$, (2.38) is transformed to a first-order form

$$
\begin{aligned}
\dot{u}_1 &= -u_1\omega_1 \sin\varphi\cos\varphi - 2\xi_1 u_1 \sin^2\varphi + \frac{3u_1 k y_e}{4\sqrt{e}m\omega_1\sigma_x^2}\sum_{i=0}^{N_c-1}\sin^2\left(\varphi_i-\gamma_1\right)\cos^2\left(\varphi_i-\gamma_1\right)\sin\varphi\cos\varphi \\
&+ \frac{3u_2 k y_e}{4\omega_1\sqrt{e}m\sigma_x^2}\sum_{i=0}^{N_c-1}\sin^3\left(\varphi_i-\gamma_1\right)\cos\left(\varphi_i-\gamma_1\right)\sin\varphi\cos\psi \\
&- \frac{k y_e}{2\sqrt{e}m\omega_1\sigma_x^2}\sum_{i=0}^{N_c-1}\sin^2\left(\varphi-\gamma_1\right)\left(0.5 y_e \sin\left(\varphi_i-\gamma_1\right)\cos\left(\varphi_i-\gamma_1\right)+e\cos\left(\varphi_i-\gamma_1\right)\right)\sin\varphi \\
\dot{\gamma}_1 &= -\omega_1\cos^2\varphi - 2\xi_1\sin\varphi\cos\varphi + \frac{3k y_e}{4\sqrt{e}m\omega_1\sigma_x^2}\sum_{i=0}^{N_c-1}\sin^2\left(\varphi_i-\gamma_1\right)\cos^2\left(\varphi_i-\gamma_1\right)\cos^2\varphi \\
&+ \frac{3u_2 k y_e}{4\omega_1 u_1\sqrt{e}m\sigma_x^2}\sum_{i=0}^{N_c-1}\sin^3\left(\varphi_i-\gamma_1\right)\cos\left(\varphi_i-\gamma_1\right)\cos\varphi\cos\psi \\
&- \frac{k y_e}{2\sqrt{e}m\omega_1 u_1\sigma_x^2}\sum_{i=0}^{N_c-1}\sin^2\left(\varphi-\gamma_1\right)\left(0.5 y_e \sin\left(\varphi_i-\gamma_1\right)\cos\left(\varphi_i-\gamma_1\right)+e\cos\left(\varphi_i-\gamma_1\right)\right)\cos\varphi
\end{aligned}
\tag{2.40}
$$

and for the *Y*- direction

$$
\begin{aligned}
\dot{u}_2 &= -u_2\omega_2 \sin\psi\cos\psi - 2\xi_2 u_2 \sin^2\psi + \frac{3u_1 k y_e}{4\sqrt{e}m\omega_2\sigma_y^2}\sum_{i=0}^{N_c-1}\sin^3\left(\psi_i-\gamma_2\right)\cos\left(\psi_i-\gamma_2\right)\sin\psi\cos\varphi \\
&+ \frac{W\sin\psi}{m\omega_2\sigma_y^2} + \frac{3u_2 k y_e}{4\omega_2\sqrt{e}m\sigma_y^2}\sum_{i=0}^{N_c-1}\sin^4\left(\psi_i-\gamma_2\right)\sin\psi\cos\psi \\
&- \frac{k y_e}{2\sqrt{e}m\omega_2\sigma_y^2}\sum_{i=0}^{N_c-1}\sin^2\left(\psi_i-\gamma_2\right)\left(0.5 y_e \sin^2\left(\psi_i-\gamma_2\right)+e\sin\left(\psi_i-\gamma_2\right)\right)\sin\psi \\
\dot{\gamma}_2 &= -\omega_2\cos^2\psi - 2\xi_2\sin\psi\cos\psi + \frac{3u_1 k y_e}{4\sqrt{e}m\omega_2\sigma_y^2}\sum_{i=0}^{N_c-1}\sin^3\left(\psi_i-\gamma_2\right)\cos\left(\psi_i-\gamma_2\right)\cos\psi\cos\varphi \\
&+ \frac{W\cos\psi}{m\omega_2 u_2\sigma_y^2} + \frac{3k y_e}{4\omega_2\sqrt{e}m\sigma_y^2}\sum_{i=0}^{N_c-1}\sin^4\left(\psi_i-\gamma_1\right)\cos^2\psi \\
&- \frac{k y_e}{2\sqrt{e}m\omega_2 u_2\sigma_y^2}\sum_{i=0}^{N_c-1}\sin^2\left(\psi_i-\gamma_2\right)\left(0.5 y_e \sin^2\left(\psi_i-\gamma_2\right)+e\sin\left(\psi_i-\gamma_2\right)\right)\cos\psi
\end{aligned}
\tag{2.41}
$$

By averaging the right hand side of (2.40) and (2.41) over the valid ranges of the approximate functions for each ball, two sets of modulation equations, representing the decoupled response in *X*-, and *Y*-directions, are found such that

$$\begin{aligned} \dot{u}_1 &= -u_1\xi_1 + \frac{C_1}{\omega_1}\left(\sin\gamma_1 + \cos\gamma_1\right) \\ \dot{\gamma}_1 &= -\frac{\omega_1}{2} + \frac{C_2}{\omega_1} - \frac{C_1}{u_1\omega_1}\left(\sin\gamma_1 - \cos\gamma_1\right) \end{aligned} \tag{2.42}$$

and

$$\begin{aligned} \dot{u}_2 &= -u_2\xi_2 + \frac{C_3u_2}{\omega_2}\cos 2\gamma_2 - \frac{C_4}{\omega_2}\left(-\sin\gamma_2 + \cos\gamma_2\right) \\ \dot{\gamma}_2 &= -\frac{\omega_2}{2} + \frac{0.28C_3}{\omega_2} + \frac{C_3}{\omega_2}\sin 2\gamma_2 - \frac{C_4}{u_2\omega_2}\left(-\sin\gamma_2 - \cos\gamma_2\right) \end{aligned} \tag{2.43}$$

where

$$\begin{aligned} C_1 &= \frac{0.1067ky_e}{2\sqrt{e}m\sigma_x^2} & C_2 &= \frac{0.2730ky_e}{4\sqrt{e}m\sigma_x^2} \\ C_3 &= \frac{0.1875ky_e}{4\sqrt{e}m\sigma_y^2} & C_4 &= \frac{0.3201k\sqrt{e}}{2m\sigma_y^2} \end{aligned} \tag{2.44}$$

To find the steady-state response, the left hand side of each set of modulation equations is set to zero resulting in

$$\begin{aligned} C_1\left(\sin\gamma_1 + \cos\gamma_1\right) &= u_1\xi_1\omega_1 \\ -C_1\left(\sin\gamma_1 - \cos\gamma_1\right) &= u_1\left(\frac{\omega_1^2}{2} - C_2\right) \end{aligned} \tag{2.45}$$

and

$$\begin{aligned} C_3u_2\cos 2\gamma_2 - C_4\left(-\sin\gamma_2 + \cos\gamma_2\right) &= u_2\omega_2\xi_2 \\ C_3u_2\sin 2\gamma_2 - C_4\left(-\sin\gamma_2 - \cos\gamma_2\right) &= u_2\left(\frac{\omega_2^2}{2} - 0.28C_3\right) \end{aligned} \tag{2.46}$$

By considering $C_3u_2 << C_4$, and squaring and summing both sides of (2.45) and (2.46), the two frequency response equations are

$$u_1 = \frac{\sqrt{2}C_1}{\sqrt{\left(\xi_1\omega_1\right)^2 + \left(\frac{\omega_1^2}{2} - C_2\right)^2}} \tag{2.47}$$

and

$$u_2 = \frac{\sqrt{2}C_4}{\sqrt{\left(\xi_2\omega_2\right)^2 + \left(\frac{\omega_2^2}{2} - 0.28C_3\right)}} \tag{2.48}$$

Figure 2.13 compares the results, computed by the method of averaging with those, obtained numerically for the frequency response of the horizontal and vertical motions of ball bearing SKF6204. Figure 2.13 (a) indicates that the agreement and quality of approximation of the horizontal motions is good throughout the range of frequency. Figure 2.13 (b) indicates that the quality of the approximation of the vertical, *Y*-direction, motion deteriorates only in the neighbourhood of the fundamental frequency of the horizontal motion, ω_1, and its superharmonic resonance of the order two $\frac{1}{2}\omega_1$ and subharmonic resonance of order $2\omega_1$.

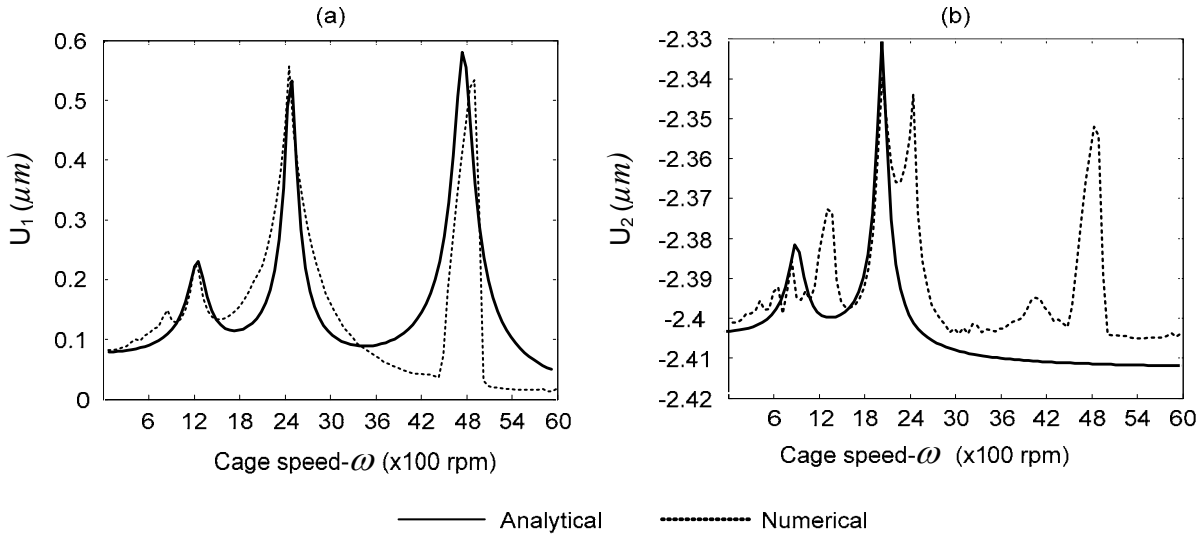

Figure 2.13. Frequency-response curves of the (a) horizontal and (b) vertical motions (*e* = 4 *μm*)

By comparing the frequency-response curves at zero clearance, Figure 2.11, and the small positive clearance, Figure 2.13, it is evident that a larger internal clearance causes

the higher amplitude of vibration in both the X and Y directions, confirming the previous research work [79]. In addition, the frequency response plots show that increasing the clearance results in lowering the resonance frequencies in both directions. As a result, the bearings with larger internal clearances are subject to resonance at lower cage speeds. The reason for this *softening* effect is the decrease in the *average* number of balls, supporting the inner ring over a single period as the clearance increases, which decreases the *effective* stiffness of the oscillator. This effect is more pronounced in the vertical direction than in the horizontal one. In fact, the order of the natural frequencies of the bearing reverses between $e = 0$ and $e = 4\ \mu m$. For $e = 0$, $\omega_1 < \omega_2$, while at $e = 4\ \mu m$, we found that $\omega_1 > \omega_2$. At some intermediate clearance value, ω_2 passes in the neighbourhood of ω_1. As a result, the bearing undergoes auto-parametric resonance; and the assumption that the vertical and horizontal motions can be decoupled is then invalid.

2.5 Chaotic Vibration of the Inner Ring

To study the appearance of chaotic vibration, the phase history of the bearing is observed, when $e > 4.5\ \mu m$. The periodic motions are represented by closed orbits in two-dimensional projections of the phase history. The projections of the chaotic motions have wandering orbits; that is, orbits that never close or repeat and tend to fill up a limited area within the projection plane. Figure 2.14 compares the orbits of the inner ring motion, projected into the $Y - \dot{Y}$ plane for various internal clearances, and a shaft speed of 3000 rpm.

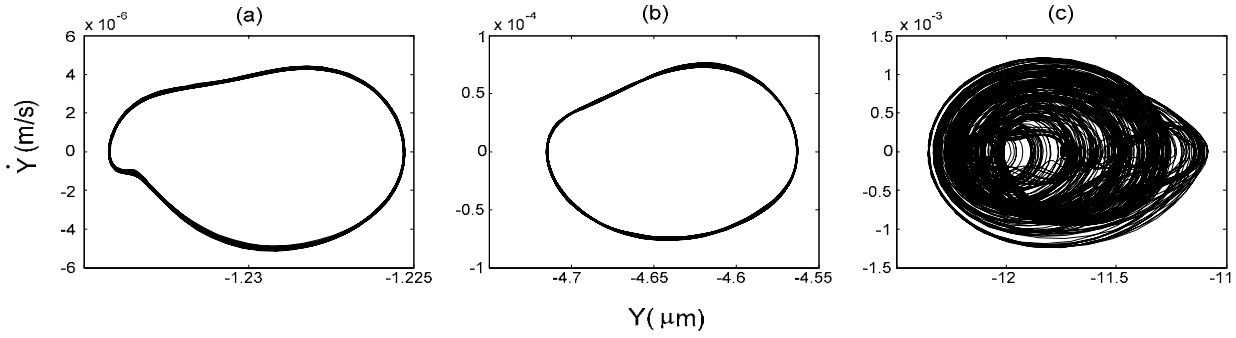

Figure 2.14. Two-dimensional projections of the inner ring (a) e=0, (b) e=3 μm, (c) e=7*μm*

Figure 2.14 (a) and (b) portray the periodic responses of the inner ring. At a larger internal clearance, e =7 μm, the bearing exhibits an aperiodic response. It consists of an infinite number of open orbits filling a limited region of the phase plane. This type of phase portrait is a strong indication of the existence of chaotic vibration in ball bearings. To confirm the nature of these orbits, their distribution on a Poincare map is examined. A map with a limited number of points denotes a periodic response, whereas the existence of a strange attractor in the map confirms the chaotic behavior.

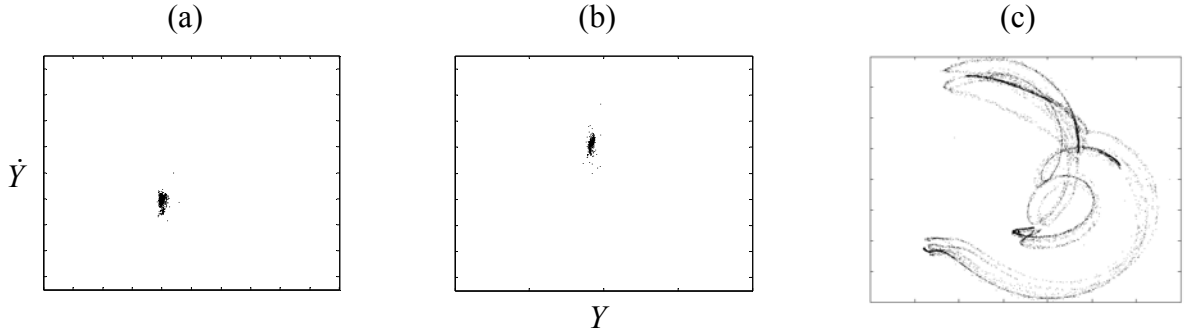

Figure 2.15. : Poincare maps of the inner ring motion (a) e=0, (b) e=3 *μm*, (c) e=7 *μm*

Figure 2.15 shows the Poincare maps that correspond to the two-dimensional projections in Figure 2.14. The maps are constructed by sampling the $Y - \dot{Y}$ plane at the period of the ball passage $2\pi/N\omega$. The Poincare maps, Figure 2.15 (a) and (b), consist of one point, denoting a harmonic motion of the inner ring for e = 0 and 3 μm clearances, as it is expected. The strange attractor in Figure 2.15 (c) confirms the existence of chaotic motion, when e = 7 μm.

To investigate the appearance of chaos and the routes to chaos when e = 7 μm, a corresponding bifurcation diagram is constructed, as the shaft speed, ω_s, is increased from 0 to 3000 rpm by sampling $\dot{Y}$ at the Ball Passage Frequency (BPF). Figure 2.16 signifies multiple regions of chaotic motions, as well as several routes to chaos. One route to chaos identified in the figure is period doubling. This route consists of a series of doublings in the period of the periodic motion, as the bifurcation parameter, ω_s,

increases. Both the period doubling and reverse period doubling are observed in the diagrams at the locations, indicated in the Figure 2.17.

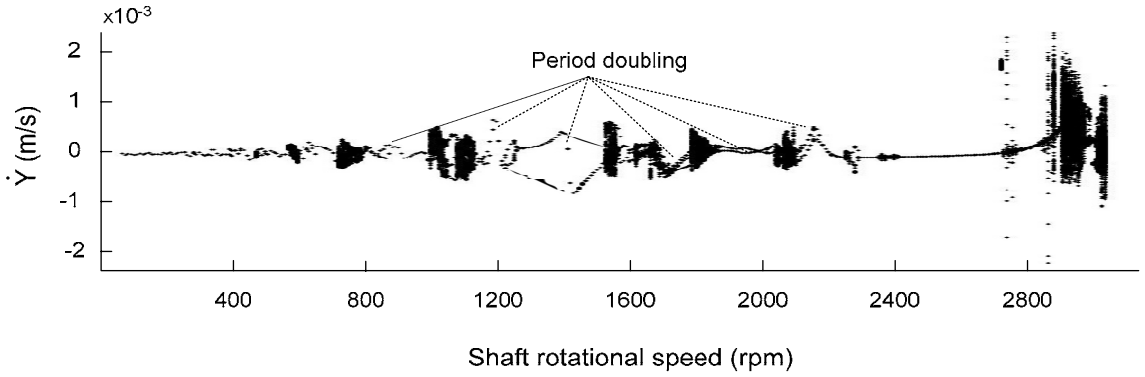

Figure 2.16. Bifurcation diagram e=7 μm

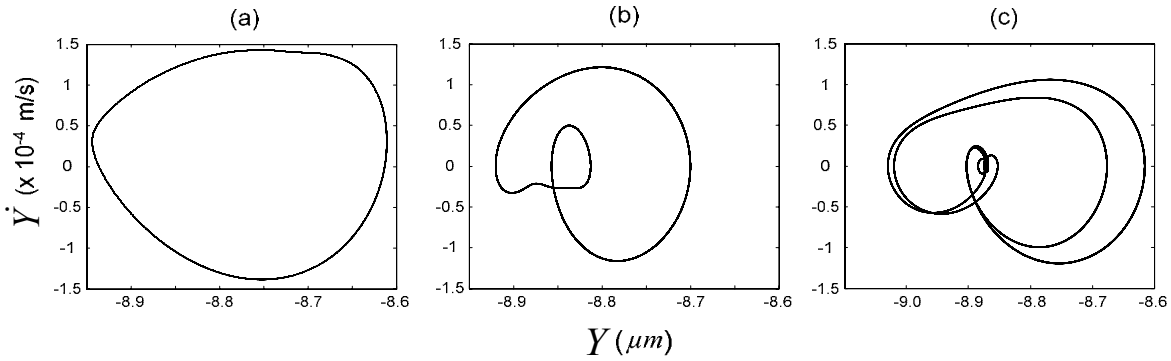

Figure 2.17. Period doubling e=7 μm (a) period T at 2315 rpm, (b) period 2T at 2260 rpm, and (c) period 4T at 2225 rpm

The chaos map in Figure 2.18 exhibits the regions of chaotic behavior in the clearance-shaft speed plane. Each horizontal line in Figure 2.18 corresponds to a bifurcation diagram that is similar to that in Figure 2.16. The map is constructed by assembling lines that correspond to the internal clearance steps of 1 μm for each. A qualitative sense of the correspondence between the color grading and chaotic behavior is obtained by comparing the seventh line of Figure 2.18 to that in Figure 2.16. The map reflects that the inner race chaotic motions dominate the bearing response when the internal clearance is larger than 5 μm, and the shaft speed is higher than 2500 rpm.

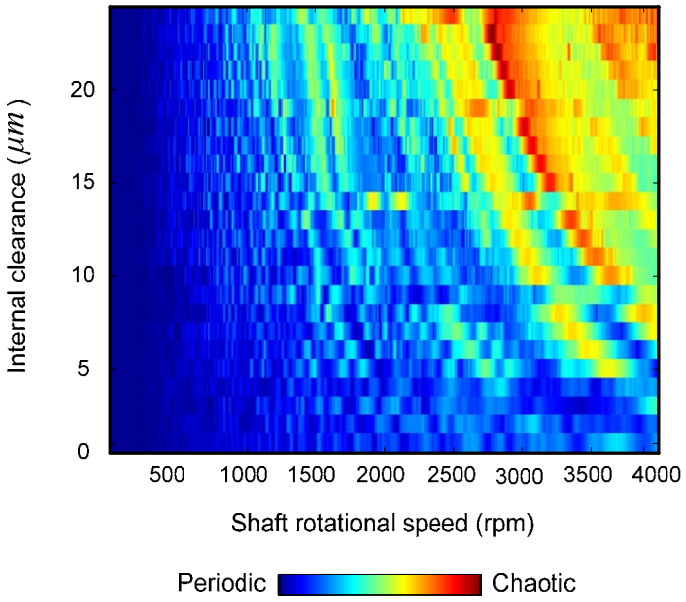

Figure 2.18. Chaos map ball bearing SKF 6204

2.6 Summary

This chapter describes a newly developed analytical method to study the dynamics of rolling element bearings, based on the Hertzian elastic contact model. For the investigated bearing, it is shown that the inner ring has either one or three equilibrium points, depending on the internal clearance. Bearings with a small clearance, $e < 4.5\ \mu m$, have one stable equilibrium point and exhibit periodic vibration of the inner ring around this centre. For a larger clearance, $e > 4.5\ \mu m$, three equilibrium points exist: an unstable saddle near the middle and two stable centres one either side. Two stable regions exist around the stable centres. As the inner ring rotates, the locations of these equilibrium points change randomly, over time, along an arch. If the cage speeds are high enough, the inner ring jumps from one of the stable regions to the other, exhibiting chaotic behavior.

The Increase in the internal clearance has a softening effect on the bearing resulting in a decrease in resonance frequencies. For bearings with $e > 4.5\ \mu m$, chaotic motions develop for specific ranges of the shaft speed. There are several routes leading to these chaotic regions. One route is a period-doubling route. The incidence of these chaotic regions increases, as the value of the internal clearance and the shaft speed increases.

Chapter 3

Numerical Analysis and Experimental Verification

In the previous chapter, it is found that the internal clearance plays an important role in the vibration behavior of a bearing. In addition, the chaos map of the sample bearing, Figure 2.18, shows that within the normal class of clearance (20-30 μm) the chaotic behavior is dominant at speed ranges higher than 1000 rpm. Since it is unfeasible to obtain closed form solution for chaotic systems, a numerical study is ideal to overcome the experimental and theoretical difficulties. Experimental problems occur due to the vibration of the power transmission components, high level of noise, and the measurement of small varying velocity and displacement. On the other hand, theoretical difficulties are mainly caused by the nonlinear behavior and the time varying parameters of the governing equations.

A number of numerical studies have been reported in the literature to characterize bearing vibration. The first observation of non-periodic vibration in a fault-free roller bearing has been reported by Sunnersjo [4]. The primary focus of his work has been on the periodic vibration, caused by the varying compliance at the low speed range. He also has explored non-periodic vibration at higher speeds. The simulation results, generated by Fukata et al. [94] have showed the superharmonic, subharmonic and beat vibration synchronized with the BPF. Besides the periodic behavior, they have explored a random-like vibration which is not synchronized with the BPF. Tsuda et al. [95] have presented results of a numerical analysis on chaotic vibration of bearings. In this work, the chaotic phenomenon is identified by means of the Lyapunov exponent and bifurcation diagram. In addition, they have observed different kinds of subharmonic oscillations and a number of period doubling routes, entailed to chaotic regions.

Kahraman and Singh [96] have explored the existence of strange attractors in the simulated model of a geared rotor bearing with backlash. Also, they have also identified period doubling and quasi-periodic routes to chaos. Mevel et al. [6] have described the subharmonic route to chaos in a lightly loaded ball bearing through numerical simulations of a nonlinear model. In their work the system exhibits subharmonic, vibration when the BPF approaches the first natural frequency of the rotor system. In addition, a quasi-periodic route to chaos has been identified and is characterized as the *competition* between the second natural frequency and the ball passage frequency. Tiwari et al. [91] have numerically studied the vibration of ball bearings. In this interesting work, three regions of high amplitude responses are identified. In the first region, a period doubling bifurcation, leading to chaotic response, is observed. The second region is generated by Hop bifurcation and quasi-periodic vibration. Finally, a superharmonic behavior at the ½ BPF is explored in the third region.

In a series of papers, Harsha [87, 88, 89] has numerically investigated the vibration of ball bearings. All the simulations have been conducted in terms of a nonlinear Hertzian contact model under an artificial damping introduced into the system to eliminate the transient vibration. Although Harsha has not succeeded to show a clear strange attractor; for the existing imbalance force and race waviness, he has identified various chaotic regions, starting from 2050 rpm for a small internal clearance of 0.5 μm [81]. Three regions of dynamic responses, include periodic, quasi-periodic and chaotic are reported in [97]. Furthermore, a quasi-periodic route has been proposed as a leading regime from periodic to chaotic behavior. Bai et al. [98] have identified three routes to chaos in the variation of the internal clearance: period doubling, quasi-periodic, and boundary crisis. The third route is a sudden creation of a chaotic attractor that occurs, as the speed passes through its critical value and the periodic response suddenly becomes unstable. Usually, the boundary crisis happens in higher range of clearance (>19 μm). Lioulios and Antoniadis [99] have demonstrated that even a small fluctuation in the rotor speed can

result in major changes of the system dynamics, from periodic to unstable periodic or chaotic response.

The novel numerical analysis presented in this chapter describes the period doubling and quasi-periodic routes to the chaos in ball bearings, and for the first time, an intermittency route for cylindrical roller bearings. In addition, the experimental investigation confirms the chaotic behavior of ball bearings by extracting a strange attractor from the measured vibration data. The significant similarity between the experimental and numerical strange attractors validates the proposed mathematical model, and verifies the existence of broad-band chaos in the bearing oscillation.

3.1 Numerical Simulation

To investigate the chaotic behavior of the rolling element bearings, the equations of motion (2.7), derived in the Chapter 2, are solved by the Rung-Kutta (4, 5) method. The selection of the proper step size, Δt, is pivotal for solving nonlinear equations. On the one hand, a large step size results in faster computations, but can fail in following high frequency contents. On the other hand, a small step size requires a longer time to reach a steady state and increases the computational noise. In addition, further analyses, such as plotting Poincare maps, computing the Lyapunov exponent, and determining the attractor's dimension, all require an integer delay at the dominant frequency which is a function of the time increment and the BPF. The time increment for all the presented simulations is computed from the following equation that yields a time delay at the BPF:

$$\Delta t = \frac{R_o + R_i}{N R_i f_s} \times 10^{-3} \tag{3.1}$$

where R_o, and R_i stand for the outer and inner ring radii, N is the number of rolling elements, and f_s denotes the shaft rotational frequency (Hz).

The initial conditions play an important role in the chaotic time series. In this regard, the following assumptions are made for the numerical simulations:

- The shaft is held at the centre of the bearing and all the balls are equally spaced.
- The bearing is fault-free and the only external force is the rotor's ideally balanced weight.
- For fast convergence, the initial displacement is set at the equilibrium point, found from the numerical solution of (2.13).
- The initial velocities in both directions are assumed to be zero.
- All the results are obtained, after the system passes its transient state.

The stiffness of each rolling element, k, depends on the geometric specifications of bearing components, roller shape, and material properties. This value for the ball bearing is calculated from (For details see Appendix I)

$$\sqrt[3]{\frac{1}{k^2}} = \Gamma^{-3/2}\sqrt[3]{\frac{4}{D_b}+\frac{2}{D_m-D_b}-\frac{1}{r_i}} + \Gamma^{-3/2}\sqrt[3]{\frac{4}{D_b}-\frac{2}{D_m+D_b}-\frac{1}{r_o}} \tag{3.2}$$

where D_b and D_m are the ball and pitch diameters, r_o and r_i are the outer and inner race groove radii, and the Hertzian deformation constant, Γ, is derived from

$$\Gamma = \frac{3K}{\pi\mu}\sqrt[3]{\frac{1-\nu^2}{3E^2}} \tag{3.3}$$

where $K/\pi\mu$ is the Hertzian constants, ν is Poisson's ratio, and E is elastic module of the ball. The coefficient, $K/\pi\mu$, is determined by the curvature relationship in the contact position, and for the ball bearing SKF 6204, is equal 0.2990 [100].

Likewise for the cylindrical roller (Appendix I),

$$k = 2.6232\times10^4\left(l_c - 2r_c\right)^{0.92} \tag{3.4}$$

Here l_c is the length of the roller contact line with each raceway, and r_c is the radius of the roller edge.

The internal damping of the rolling element bearings arises primarily from the lubricant. The theoretical evaluation of the bearing's damping, due to the effect of the lubricant material, viscosity, and temperature, is very difficult. Therefore, in this work, the damping parameter is experimentally measured by an impact test. The experimental setup

for the modal analysis test is illustrated in Figure 3.1. Each test is conducted, after the bearing has been running for 20 minutes, to reach a stable viscosity and temperature value. Since the viscosity of the lubricant plays an important role in the value of the damping coefficient, and consequently, in the solutions of the governing equations, the bearings are tested while they are lubricated with standard oil (v =15 mm^2/s) and high viscous grease (v = 110 mm^2/s). The bearing is tested in a free-free condition which is achieved by supporting the bearing on a light elastic band, as shown in Figure 3.1. The equipment utilized for this test are the data analyzer, LMS SCADAS III, including the data acquisition hardware and modal analysis software, *LMS Test Lab*, a Dytran Piezo accelerometer 3035AG, and a Dytran impulse hammer, Dynapulse 5850B with a sensitivity of 1 mV/LBF, and a 150 gram tip. The results of the impact test from the modal analysis software are shown in Figure 3.2.

The first natural frequency of the ball bearing is measured at 2941 Hz with a damping ratio 4.15%. Therefore, the damping of the tested ball bearing can be found from the following:

$$c_b = 2\zeta m\omega_n = 572.4 \qquad (Ns/m) \tag{3.5}$$

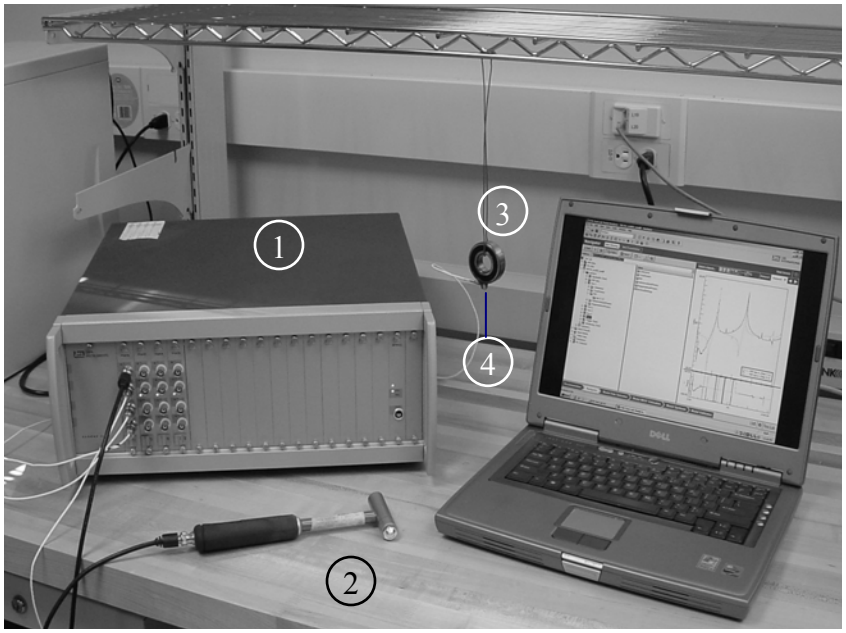

1. SCADAS III 2. Impact hammer 3. Test bearing 4. Accelerometer

Figure 3.1. Bearing impact test

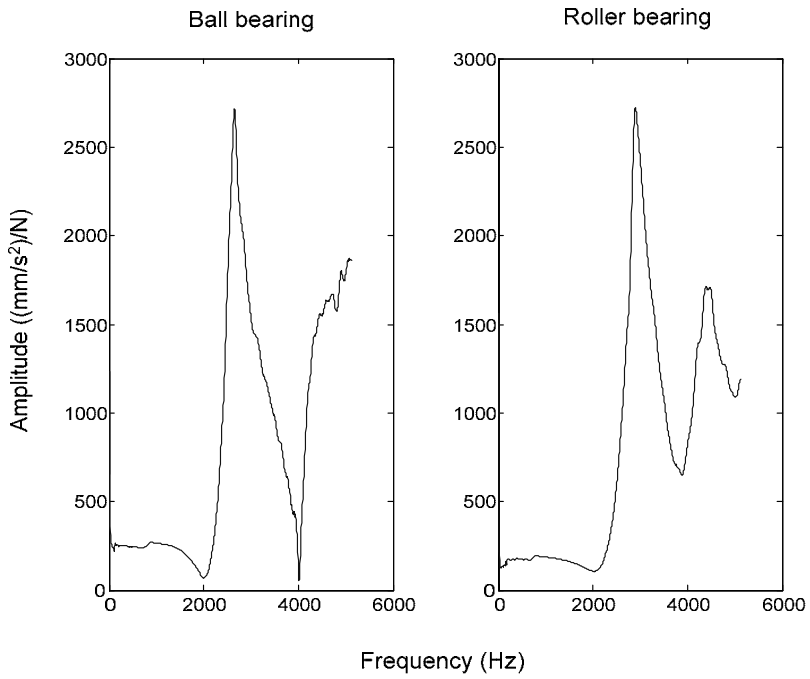

Figure 3.2. Bearings modal impact test; ball bearing first natural frequency 2941 Hz, Roller bearing first natural frequency 2906 Hz

The measured value for a grease lubricated bearing is 694 Ns/m. Likewise; the impact test on a cylindrical roller bearing measures the first natural frequency at 2906 Hz with the damping ratio, 4.74%. From this, the damping coefficient is computed at 646 (Ns/m). The equations of motion (2.7) are solved for the deep groove ball bearing, SKF 6204, for the rotational speed 680 rpm, utilizing the specifications listed in Table 3.1, and using both measured damping coefficients. The internal clearance of both bearings is selected at the normal class of 20 μm. Therefore, according to the previous analytical discussion in the Chapter 2, there is a high possibility that chaotic behavior occurs.

Table 3.1. Specification of ball and roller bearing

Ball Bearing SKF 6204		**Roller Bearing SKF NJ204ECP**	
Ball diameter (mm)	7.938	Inner race diameter (mm)	26.500
Inner race diameter (mm)	25. 5620	Outer race diameter (mm)	41.500
Outer race diameter (mm)	41.4380	Pitch diameter (mm)	35.000
Pitch diameter (mm)	33.5	Length of roller (mm)	9.000
Race groove radius (mm)	4.1278	Radius of roller edge (mm)	0.333
Clearance (μm)	20	Clearance (μm)	20
Number of balls	8	Number of Rollers	11
Rotor's weight (N)	23.004	Rotor's weight (N)	23.004
Coefficient of stiffness (N/m)	9.21×10^9	Coefficient of stiffness (N/m)	3.21×10^8

The Poincare map is a powerful diagnosis tool for investigating chaotic systems. The map can be generated by crossing the trajectories of a three-dimensional phase space through a two-dimensional plane. When the Poincare map of a vibration signal is not in the form of a finite number of the points, the motion may be chaotic. The chaotic Poincare map of an undamped or lightly damped system appears as a cloud of points. In a chaotic damped system, the Poincare map contains a set of organized points, arranged in parallel lines and magnetized to an unknown point. The appearance of these trajectories, called the strange attractor, in the Poincare map is a strong indicator of the presence of chaotic motion.

The Poincare map, obtained from the numerical solution of the oil lubricated bearing, Figure 3.3 (a), indicates a noise-like response that appears as an unorganized cloud of points. Increasing the damping coefficient in the model to the level of the grease lubricated bearing reveals the existence of a strange attractor, as portrayed in Figure 3.3 (b).

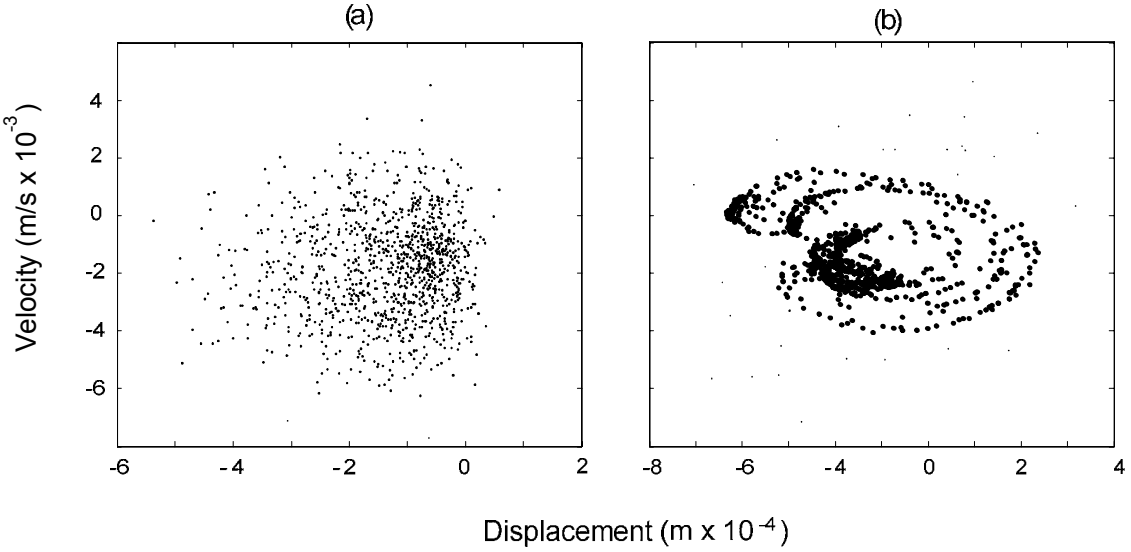

Figure 3.3. Poincare maps of simulation results: (a) damping 572.4 Ns/m and (b) damping 694 Ns/m

To assess the general characteristics of the bearing vibration, a broad-band bifurcation diagram for the velocity in the vertical direction is plotted for both types of simulated bearings with an internal clearance of 20 μm. The presented bifurcation diagram, Figure 3.4, is similar to the 20th line of the chaos map in Figure 2.18. In the chaos map, the variation of the velocity at each specific speed is represented by the color format. Both bifurcation diagrams demonstrate that the bearings with balls or cylindrical elements, respectively, exhibit chaotic behavior for a wide range of shaft speeds. The vibration of the ball bearing in Figure 3.4 (a) begins with a regular periodic motion, as expected at low running speeds. When the shaft speed increases, the bearing exhibits a limited band chaos, immediately followed by post chaotic motion. At speeds higher than 600 rpm, the system frequently experiences broad-band chaos with a narrow-band periodic motion of

T, 2T, 3T, or 4T period in the chaotic regions. Figure 3.4 (b) confirms that the periodic motion exists at low shaft speeds in the investigated bearing with cylindrical elements. The system reveals a limited band chaos in a range of 5 to 200 rpm. Afterwards, the bearing exhibits a broad-band chaotic vibration.

These simulation results confirm the previous chapter discussions, regarding the effect of the internal clearance in the regime of the vibration. However, the occurrence of chaotic behavior is more significant at a larger clearance. Even for a normal class of clearance, bearings exhibit periodic vibration at low speeds.

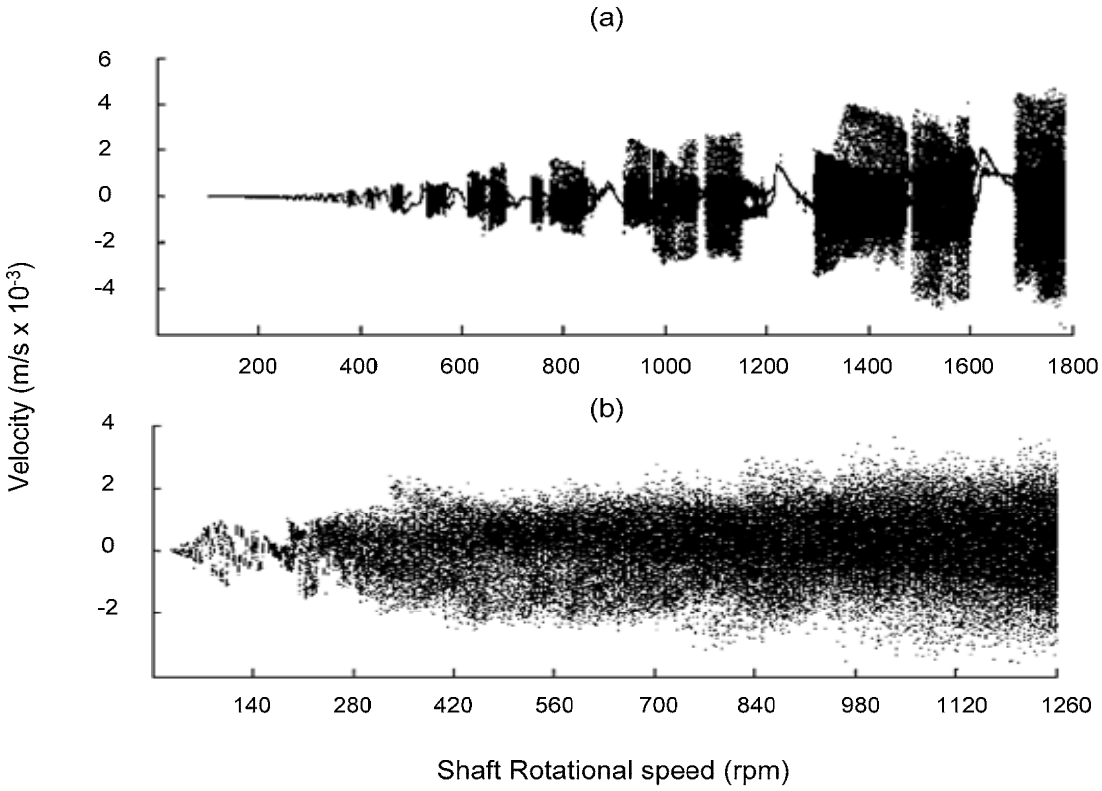

Figure 3.4. Results of the numerical simulations shown for broad-band bifurcation diagrams for: (a) a ball bearing, (b) a roller bearing

As mentioned in Chapter 2, a series of the doublings in the nature of the periodic motion occurs in the bifurcation diagram of the bearing vibration. This period doubling usually exists before and/or after the chaotic boundaries in the bifurcation diagram. When this

phenomenon originates from a periodic region, the doubling process can be continued until the motion become chaotic. Vice versa, a chaotic characteristic can be transformed to periodic through a series of reverse period doublings. Period doubling is a well-known route to chaos. Figure 3.5 shows the period doubling before and after a chaotic region and bubble bifurcation in the range of 440 to 520 rpm. The presented period doubling has a Feigenbaum number of 1.46 that expresses ratios of bifurcation diagram in Figure 3.5.

Figure 3.4 (b) presents another route to chaos in a cylindrical roller bearing. In this regime, the periodic motion is influenced by transient chaotic bursts. Increasing the rotational speed results in chaotic bursts occur more frequent and longer. The occurrence of transient vibration increases, until the dynamics of system become completely chaotic. This route to chaos, which is observed in the bifurcation diagram of the cylindrical roller bearing in Figure 3.4 (b), is called *intermittency*.

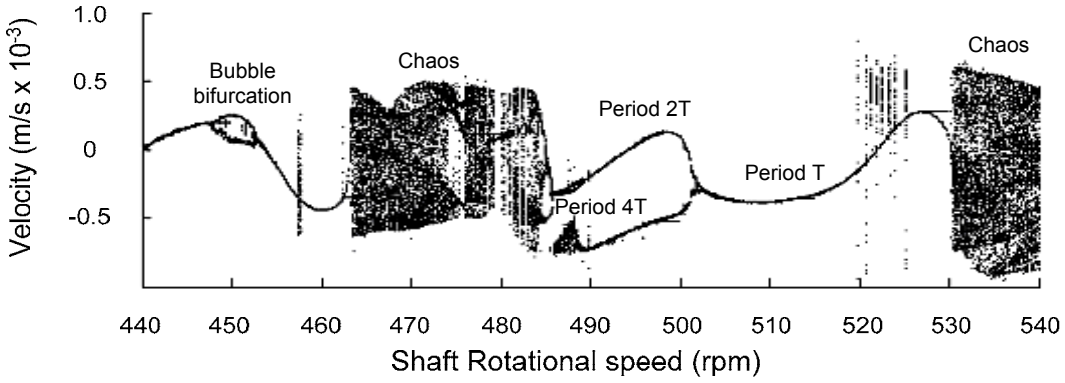

Figure 3.5. Simulation results: detailed bifurcation diagram for a ball bearing

Further insight into the chaotic behavior in bearings is gained from the numerical simulations by following the "route to chaos", for the ball bearing and roller bearing, as shown in Figure 3.6 and Figure 3.7, respectively.

Figure 3.6 (a), (b), and (c) illustrate the periodic vibration of the system at the low speed of 98 rpm which corresponds to the BPF of 5 Hz. The distinct spectral lines in Figure 3.6 (a), the closed orbit in the phase plane in Figure 3.6 (b), and the single point Poincare map in Figure 3.6 (c), all demonstrate the periodic behavior of the system. The solution

of the equation (2.7) based on the shaft rotational speed of 490 rpm (BPF = 25 Hz) is depicted in Figure 3.6 (d), (e), and (f). The signs of period doubling are observed in the spectrum, Figure 3.6 (d), the closed orbit in phase plane that crosses itself, Figure 3.6 (e), and the existing two points in the Poincare map, Figure 3.6 (f). The system exhibits chaotic vibration at the higher speed of 980 rpm, which corresponds to the ball passing frequency of 50 Hz. Besides the distinct harmonics of the BPF, the spectrum in Figure 3.6 (g) reflects a broad-band of frequencies. The open phase plane orbits tend to fill a portion of the diagram. The drifting of the phase orbits in Figure 3.6 (h) is a strong indicator of chaos in the system. Finally, the occurrence of a strange attractor in the Poincare map in Figure 3.6 (k) further validates the chaotic oscillation of the bearing. The change of a periodic motion to a quasi-periodic regime, and to chaos, is a common route to chaos called Hopf bifurcation.

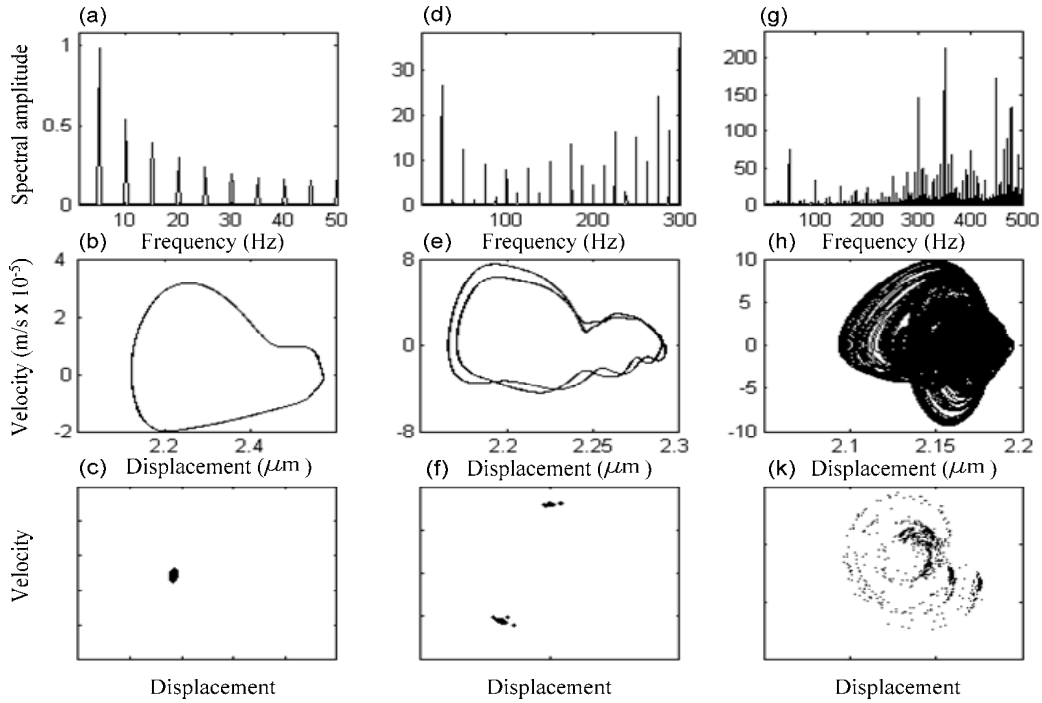

Figure 3.6. Route to chaos in ball bearing SKF 6204

Similarly, the simulations reveal the intermittency route to chaos for the cylindrical roller bearing for speeds of 14, 140 and 560 rpm. Figure 3.7 (a), (b), and (c) confirm the same phenomenon, of "periodic vibration at a low speed" also happens in cylindrical roller bearings (shaft speed 14 rpm; BPF = 1 Hz). Increasing the shaft speed (shaft speed 140 rpm; BPF = 10 Hz) leads to the intermittency characteristic as shown in Figure 3.7 (d), (e), and (f). In this route, although the periodic vibration is dominant, chaotic bursts can be detected in a longer time series. This transformation from a periodic to a chaotic regime is intermittency route to chaos. In this regime, the chaotic effect can be observed as the weak broad-band frequency in the power spectrum, Figure 3.7 (d), and a slightly thicker phase plane in Figure 3.7 (e). A chaotic trajectory appears in the Poincare map, if the resolution of the solution is small enough, and the length of the data series is sufficiently long, as shown in Figure 3.7 (f). When the shaft speed exceeds 280 rpm, the bearing exhibits broad-band chaotic vibration, which is apparent in the bifurcation diagram. A detailed solution for the vibration of a roller bearing at a shaft speed of 560 rpm (BPF = 40 Hz) is presented in Figure 3.7 (g), (h), and (k). Here, the strong broad-band frequency, Figure 3.7 (g), the open orbits of the phase plane, Figure 3.7 (h), and a vague strange attractor in the Poincare map due to the light damping of the system, Figure 3.7 (k), all verify the chaotic behavior of bearing oscillation.

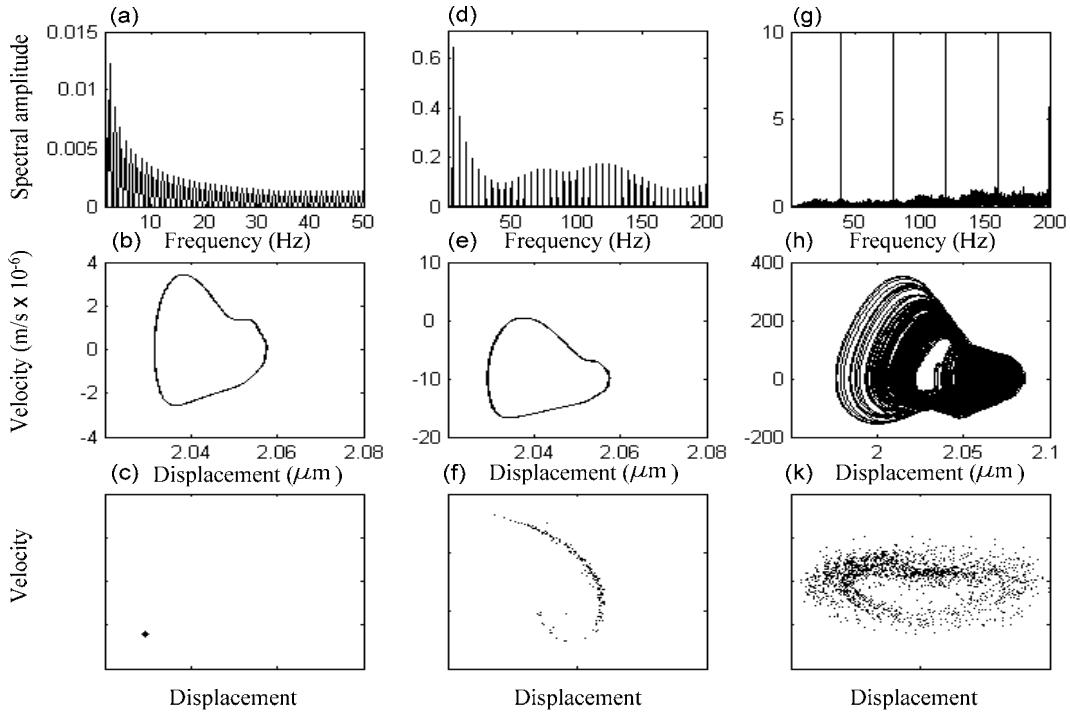

Figure 3.7. Route to chaos in cylindrical roller bearing SKF NJ204ECP

3.2 Experimental Observations

In the experimental setup Figure 3.8, a well-lubricated deep groove ball bearing, SKF 6204, is inserted in the bearing housing. A flexible coupling is utilized to minimize the effect of the driving component vibration. In addition, particular attention is paid to the system's alignment to decrease the misalignment that can add unwanted periodicity in vibration signature. The vibration of the bearing is measured by a Dytran 3035 AG accelerometer with a sensitivity of 100 mV/g. The system is driven with a 3 hp induction motor, equipped with an AC Tech M1230 SB speed controller, in the range of 0-1800 rpm. A DACTRON dynamic signal analyzer, Photon 100, equipped with a low-pass anti-aliasing filter is utilized for the data acquisition.

The system's chaotic characteristic is easily observed, when it is viewed from a phase plane or particularly from the Poincare map. Accordingly, a code in the Matlab environment is developed to integrate the acceleration data via the trapezoidal method to

obtain the velocity and displacement. To increase the number of Poincare points for the observation of the strange attractor, a long data series is required. In the current experiments, the vibration data is stored at a sampling frequency rate of 6000 Hz for 30 minutes with the shaft rotating at 680 rpm. Then, the vibration signal is re-sampled at 250 Hz to collect the Poincare points.

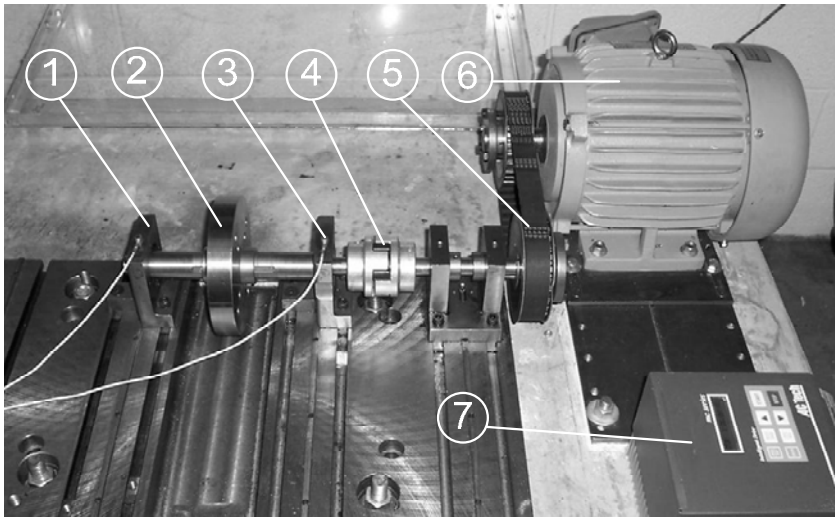

1. Test bearing housing
2. Balanced disk
3. Piezo accelerometer
4. Flexible coupling
5. Timing belt
6. Motor
7. Speed controller

Figure 3.8. Experimental test bed

Figure 3.9 illustrates the extracted displacement, velocity, and related phase plane of the bearing vibration, obtained from integrating the measured acceleration data.

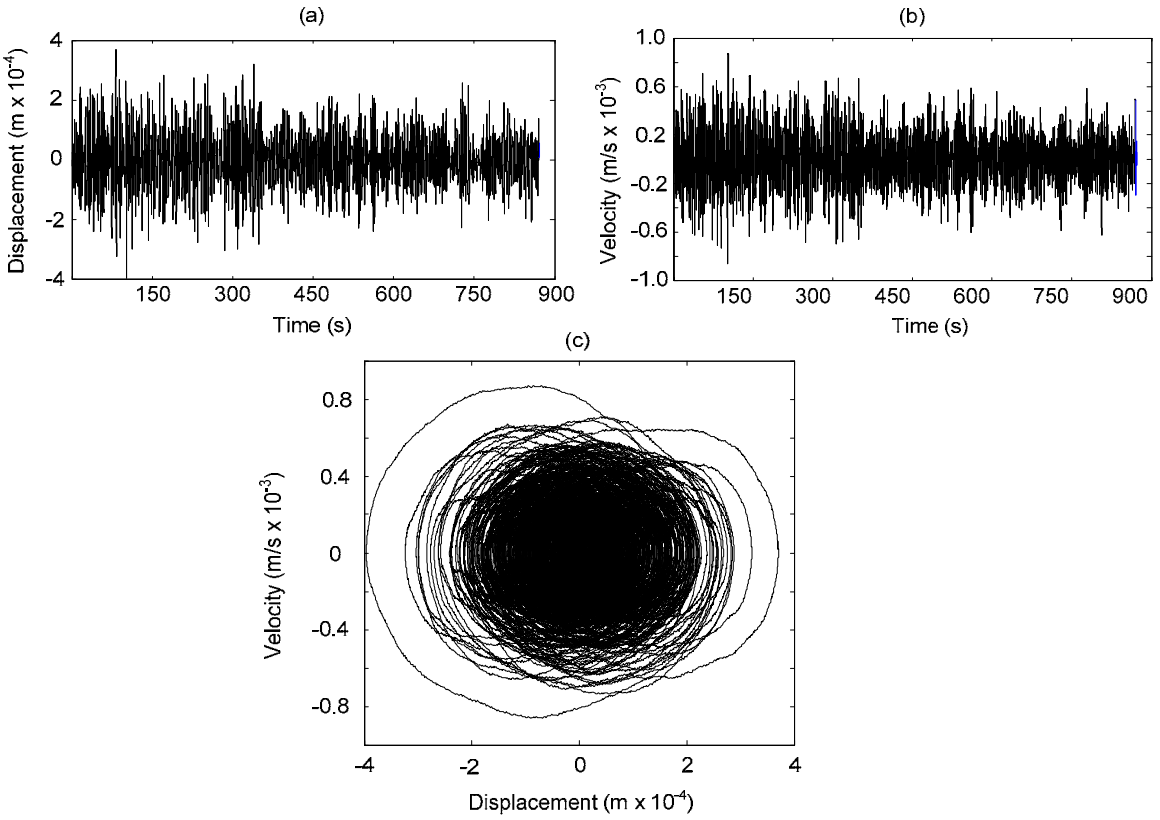

Figure 3.9. Vibration of ball bearing (experimental data) at the speed of 680 rpm and sampling frequency 6000 Hz (a) displacement, (b) velocity, and (c) phase plane

The phase plane diagram in Figure 3.9 contains an infinite number of orbits that tend to fill a portion of the plane. It can be a strong indicator of chaotic vibration. Yet, it is the Poincare map that is the principal way of identifying a system's chaos. If a system, however, does not have sufficient damping, the chaotic attractor appears in the form of a cloud of unorganized points. This type of map is shown in Figure 3.10 (a), obtained from the same data used in constructing the phase plane in Figure 3.9 (c). The plotted data in Figure 3.9, and Figure 3.10 (a) are obtained from a ball bearing lubricated by normal oil ($v = 15$ mm^2/s). To increase the damping of the bearing, the rings and balls are lubricated with a viscous grease ($v = 110$ mm^2/s), which results in increasing the damping from 572.4 to 694 (Ns/m). The procedure for the damping measurement is described in detail in the previous section. The constructed map in Figure 3.10 (b) reveals a strange attractor

with a fractal structure that validates the existence of chaos in the measured data. The shape of strange attractor obtained from experimental data, Figure 3.10 (b), is similar to the simulated map in Figure 3.3 (b), generated by solving the equation of motion (2.7) with similar parameters for the damping, bearing specifications, and running speed, as used in the experimental setup. This qualitative verification not only confirms the existence of chaos in the rolling element bearings, but also validates the behavior of the mathematical model proposed in Chapter 2. Other quantitative measures; namely, the Lyapunov exponent and fractal dimension will be used later to further confirm that chaos does indeed exist in the bearings vibration. These chaos measures also will serve to quantify the effect of the faults on the vibration signature of the system.

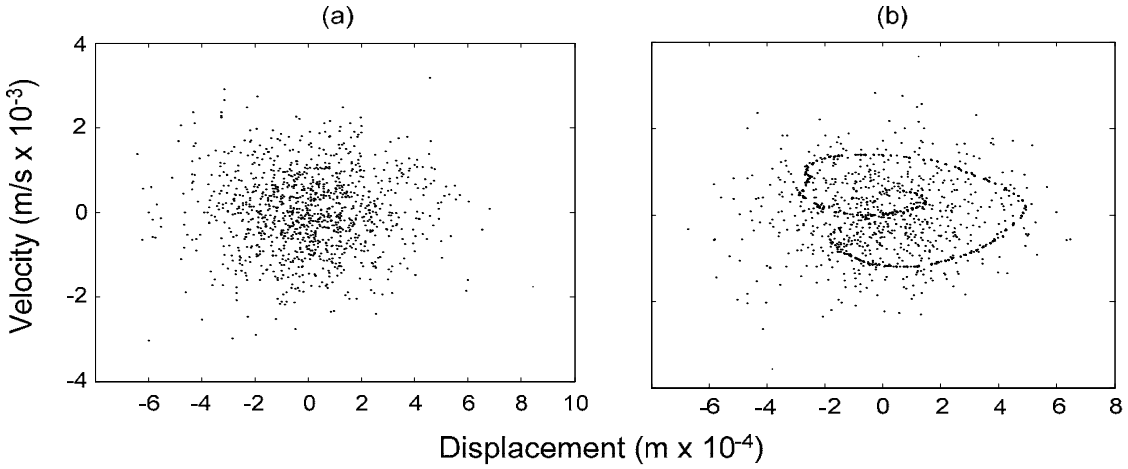

Figure 3.10. Experimental Poincare map of a ball bearing at the speed of 680 rpm with (a) normal lubrication (*c*=572.4 Ns/m) and (b) grease (*c*=694 Ns/m)

3.3 Summary

The numerical analysis of the developed nonlinear model verifies that bearings exhibit chaotic behavior through period doubling and intermittency routes in a wide range of rotational speeds. The simulation results also show the effect of damping, regarding the appearance of the strange attractor in the Poincare map. The experimental results in this thesis reveal the existence of a strange attractor, and its similarity with the simulated attractor. This strong evidence confirms the chaotic behavior of a healthy rolling element bearing, and qualitatively validates the developed model for bearing vibration. In the next chapter, some measures for the quantification of the chaotic behavior are introduced. Furthermore, the effect of the localized faults of the bearings on the chaotic parameters is investigated.

Chapter 4

Fault Diagnosis and Chaotic Indicators

In the previous chapters, it was shown that rolling element bearings exhibit chaotic behavior within a wide range of rotation speed. Then, it is reasonable to expect that, the faults in the system can affect this behavior. The propagation of damage can manifest itself in the phase plane or the Poincare map, or, better still, alter chaotic quantifiers such as the Lyapunov exponent, correlation dimension, and information entropy.

Up to now, very little research has been reported in the literature, regarding the possible relation between chaotic parameters and bearing faults. Lin et al. [101] have reported that the faults in simple rotary machinery with gears and bearings can affect the fractal dimension value. Logan and Mathew [8, 9] have proposed a correlation integral for the assessment of a bearing's condition. They have utilized a partial correlation integral to determine the dimension of the system. Their experimental results for a self-aligned bearing at a constant speed of 3000 rpm demonstrate a significant reduction in the system's dimension for a bearing with a defect in the outer ring. However, the application of a low pass filter at 2000 Hz in the data acquisition process results in eliminating useful high frequency data (>4000 Hz) which usually contains the effect of higher harmonics of the inner race and ball damage effect. Consequently, the reported fault diagnosis of the inner race and ball damage is not notable. Choy et al. [10] have utilized a modified Poincare map for the damage quantification in tapered and roller bearings. Their work shows that the modified Poincare map, based on the cage speed, provides information on the damage type. Furthermore, the size of defect is corroborated by the vibration amplitude to provide information regarding the level of fault propagation. Recently, Li

and Qu [102] have proposed a new fault diagnosis scheme, based on the forward detecting method, for bearings. Such a method is used to detect weak periodic signals by identifying the transformation of the chaotic oscillator from the chaotic state to the large-scale periodic state, when a weak external periodic signal is applied. This method is successfully applied to detect the existence of a periodic signal at the bearing characteristic frequency, which confirms the existence of damage in the corresponding component.

In the current chapter, the goal is to establish that different bearing faults directly impact the chaotic response of a system. Novel measures, the Lyapunov exponent, correlation dimension, and information entropy are utilized to quantify the effect of damages on the chaotic signature. Variation in these chaotic quantifiers, due to the propagation of a fault in the bearing components, can be employed as a diagnostic routine for rolling element bearings.

4.1 Chaotic Indicators

To investigate the effect of bearing faults on chaotic vibration, measures for determining the system's chaos level are required. In the current study, three known quantifiers of chaotic systems: the Lyapunov exponent, correlation dimension, and information entropy are utilized to measure the changes in the chaotic state. Usually, these measures are used as diagnostic criteria to reveal if a system is in the state of chaos or not. However, in this thesis these quantifiers are utilized to diagnose a bearing heath condition.

4.1.1 Lyapunov Exponent

The Lyapunov exponents of a map can be used as a measure of a system's sensitivity to initial conditions. When a chaotic system evolves from a set of initial conditions within radius d_0 in the phase plane, after time *t*, the trajectories' divergence is characterized by

$$d = d_0 2^{\lambda t} \tag{4.1}$$

where Lyapunov exponent λ, corresponds to the average rate of the divergence of the trajectories. When the largest Lyapunov exponent is positive, or the system contains at least one positive Lyapunov exponent, the system exhibits chaotic behavior.

Different methods have been proposed for computing the Lyapunov exponents from a time series, categorized as direct and model based methods. The direct method is adopted to estimate the Lyapunov exponents of the reconstructed state without fitting a model to the experimental data. The common method for reconstructing the data from the experimental measurements or time series is the delay coordinates technique. For a given time series $x(t)$, *m*-dimensional reconstructed data is in the form of

$$\left[x(t), x(t+\tau), ..., x\left(t+(m-1)\tau\right)\right] \tag{4.2}$$

When the reconstruction dimension, *m*, is large, it is expected that the noise decreases the density of the data that represents a strange attractor. Therefore, the small value of *m* usually results in more reliable Lyapunov exponents. When the time delay is very small, the reconstructed vectors do not significantly differ from each other. In this case, the investigation of a possible fractal structure becomes difficult. If the selected time delay is lengthy, the attractor may not contain sufficient data to show the fractal structure of the data series. In this thesis, the proper combination of reconstruction parameters for the bearing vibration is found by a number of experiments. The results prove that a series of two-dimensional vectors, reconstructed with a ball passage period delay, provides a stable Lyapunov exponent at each constant rotational speed. The selected computation process is a direct method, developed by Wolf et al. [103], to estimate the largest

Lyapunov exponents of the reconstructed state without fitting a model to the experimental data. For the current application, the Wolf method is modified to reconstruct a two-dimensional data series from the acceleration, measured at a sampling frequency of 6 kHz, and low pass filtered at 2 kHz to reduce the effect of noise. Then, the reconstructed time series is re-sampled with a time delay of 1.156 seconds (equal to ball pass period) to obtain the Poincare points. The computation stops when the results converge within a ±1 percent error band.

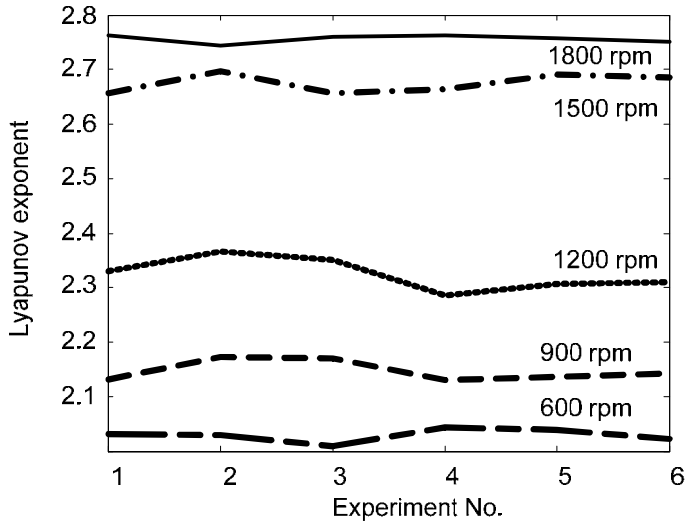

Figure 4.1. Stability Lyapunov exponent at various shaft rotational speeds

Since the Lyapunov exponent is the average of the trajectories' divergence in the system, where the chaotic mechanism is unknown, the repeatability of the exponent should be checked. A set of experiments is conducted to investigate the repeatability of the Lyapunov exponent. The results, shown in Figure 4.1, demonstrate the stability of the measured Lyapunov exponent at different rotational speeds. Moreover, the positive value of all the measured Lyapunov exponents further validates the chaotic vibration of the system.

4.1.2 Correlation Dimension

In addition to the Lyapunov exponent which is a quantitative measure of chaotic motion, the fractal dimension is a measure of the strangeness of the attractor. There are various ways to express the dimension of a fractal set. The correlation dimension is an efficient method to determine the dimension of experimental data [92]. To calculate the correlation dimension, the orbit of the phase plane needs to be digitized to a set of N_d points, $[x_i]$. Then, the distance between each pair of points is calculated. The correlation function is defined as

$$C_d(\varepsilon) = \lim_{N_d \to \infty} \frac{1}{N_d^2} \sum_{i=1}^{N_d} \sum_{j=1}^{N_d} H\left(\varepsilon - \left\| x_i - x_j \right\|\right) \tag{4.3}$$

where x_i and x_j are points in the data set. H is the Heaviside function (with $H(x) = 1$ for $x > 0$ and zero elsewhere), and N_d is the number of digitized data chosen from the data set. The Heaviside function counts the number of points within radius ε from point x_i, and $C_d(\varepsilon)$ is the average fraction of the points within ε. Consequently, the correlation dimension is the slope of a graph of $\log C_d(\varepsilon)$ versus $\log \varepsilon$. This method of estimating the dimension has the advantage of requiring less computer memory and computational time than other methods. An important step in computing the correlation dimension from the experimental data is choosing the appropriate parameters for the attractor reconstruction. However, there are only a few guidelines for selecting the parameters for an unknown system, and finding the optimum values is based on a large number of experiments.

The first step for determining the correlation dimension is data reconstruction. m - dimensional vectors can be constructed with delay τ and vector spacing α from a data series with length M. Ruelle [104] has suggested that the length of a data series for calculating the correlation dimension should be selected such that

$$M \geq A^{\frac{dg}{2}} \tag{4.4}$$

where dg is correlation dimension, and A should be at least 10. For the experimental data, Simm et al. [105] have recommended that the length of the reconstructed vector, m, be larger than the system dimension ($m \geq d$). Time delay τ and vector spacing α are defined by a number of experiments to satisfy the repeatability condition within a ±5% error band. Afterwards, the correlation integral is calculated in a range of different radii ε. Finally, the correlation dimension is obtained from the slope of a graph of $\log C_d(\varepsilon)$ versus $\log \varepsilon$. To compute the values of the correlation dimensions, it was found that the proper reconstruction parameters are as follows: vector length m = 15, internal vector delay $\tau = 8$, and vector spacing $\alpha = 15$.

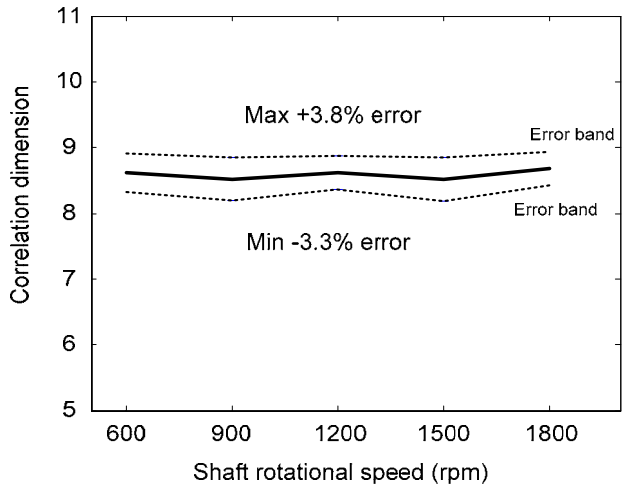

Figure 4.2. Experimental correlation dimension and measured error band

These parameters are applied to compute the correlation dimension of the measured acceleration. The experimental results plotted in Figure 4.2 demonstrate that the correlation dimension is constant for a wide range of rotation speeds within an acceptable error band. This unique property of the correlation dimension can be applied for the fault diagnosis of rotary machines with variable speeds.

4.1.3 Information Entropy

A chaotic system is very sensitive to the initial conditions. In such a system, although the initial state is known, the ability to predict future states diminishes due to the trajectories' divergence. The measure for determining the diminishing rate of the necessary information for future state estimation is called information entropy. For calculation, it is necessary to count the number of points N_i which lie within a subinterval, N, of the data set. The probability of finding a point in that subinterval, P_i, is determined by

$$P_i = \frac{N_i}{N_0} \tag{4.5}$$

where N_0 is the total number of points in the reconstructed time domain data. The information entropy, I, is defined by

$$I = -\sum_{i=1}^{N} P_i \log P_i \tag{4.6}$$

If the length of each N subinterval data set is assumed to be ε, for a small ε, the information entropy behaves according to:

$$I \approx d_I \log\left(\frac{1}{\varepsilon}\right) \tag{4.7}$$

where d_I is the information dimension of the chaotic attractor. It has been reported by Kaplan and Yorke [106] that the information dimension, d_I, is related to the Lyapunov exponents by

$$d_I = j + \frac{\sum_{i=1}^{j} \lambda_i}{\left|\lambda_{j+1}\right|} \tag{4.8}$$

and j is defined by the condition

$$\sum_{i=1}^{j} \lambda_i > 0 \qquad \text{and} \qquad \sum_{i=1}^{j+1} \lambda_i < 0 \tag{4.9}$$

Equation (4.9) clearly shows that a variation in the positive Lyapunov exponents directly affects the information dimension, and consequently, the information entropy. This relationship between the positive Lyapunov exponents and the information entropy will be used for fault diagnosis of the bearings.

To show the robustness of this chaotic measure, the stability of the information entropy is studied. Figure 4.7 shows the results of experimental information entropy at various running speeds. Although the level of entropy increases at higher speeds, the variation of this indicator remains in an acceptable error band at each constant speed.

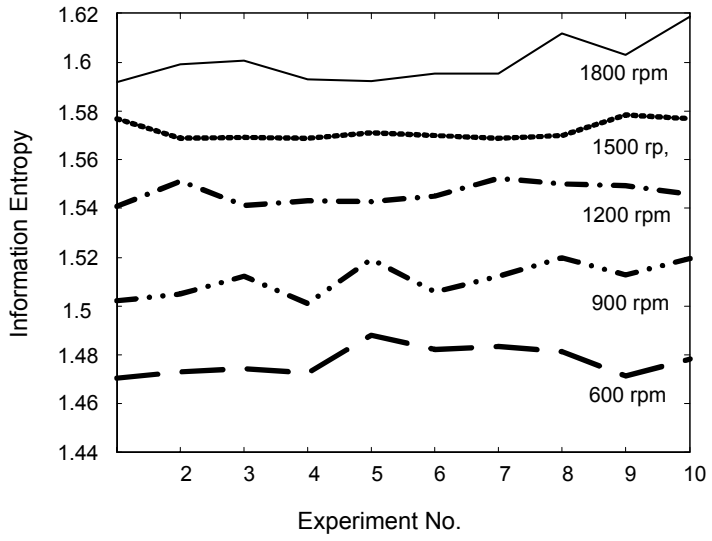

Figure 4.3. Stability information entropy at various shaft rotational speeds

4.2 Effect of Machinery Faults on Chaotic Indicators

In the previous chapters, it was demonstrated that a balanced and aligned rotor, supported by a healthy rolling element bearing could exhibit chaotic vibration. Therefore, it is expected that the faults in the system could affect this behavior. Such a variation can reshape the geometric representatives or change the chaotic quantifiers. Therefore, the

effect of common machinery malfunctions on chaotic quantifiers is studied to assess their efficiency as fault indicators.

4.2.1 Bearing Localized Faults

When a defect on a raceway or rolling element strikes its mating element, a pulse of a short duration is produced. For a constant shaft speed, a series of such pulses is generated, forming a pulse train that is periodic with a frequency that depends on the nature and location of the fault, as well as on the geometric parameters of the bearing. It is reasonable to expect that this added periodicity affects the chaotic vibration of the bearing. In other words, the presence and severity of a fault affects the resulting phase diagram and Poincare map. The visual inspection of these diagrams is certainly crucial for fault diagnosis. Better still are some measurable quantities such as numerical values that can potentially be employed in an automated fault diagnostic system. In this section, the Lyapunov exponent, correlation dimension, and information entropy are chosen as the numerical quantifiers for fault monitoring.

To visualize the effect of a localized fault on the chaotic attractor, an impulse train that symbolizes the strikes between the moving component and the physical damage, is added to the right hand side of equation (2.7). The frequency of the impulse is set at the bearing fault frequencies which correspond to the location of the virtual damage. Figure 4.4 portrays the effect of different types of virtual damage on the chaotic attractor of a cylindrical roller bearing.

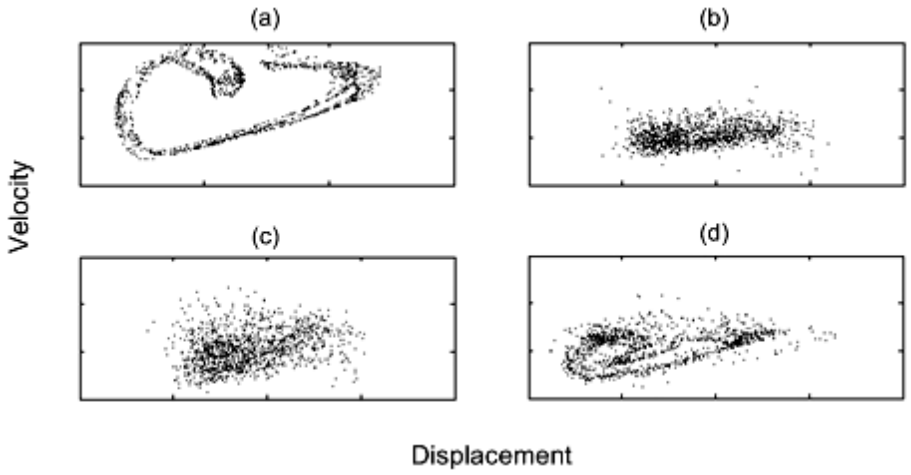

Figure 4.4. Simulation results: Effect of localized faults on the chaotic attractor; (a) healthy cylindrical roller bearing, (b) inner race fault, (c) ball damage, and (d) outer race fault

The simulation results in Figure 4.4 illustrate the effect of the faults on the chaotic attractor. The added periodicity in the equation of motion through the impulse train significantly reshapes the form of the strange attractor. However, the effect of the outer race fault, due to a smaller hitting frequency, is not as significant as that of the inner race and ball damage faults with higher fault frequencies.

To evaluate the effect of bearing faults on chaotic behavior, vibration data are obtained from experiments for four bearing conditions: normal (fault-free), inner race fault (localized wear area1.6 mm^2, created by grinding), ball damage (indentation 0.8 × 0.8 mm, created by an electro discharge machine), and outer race fault (localized wear 2.8 mm^2, created by grinding). The faults are induced into the drive-end bearing of model SKF NJ204ECP, a cylindrical roller bearing, on the test rig in Figure 3.8. This bearing is chosen for the fault diagnostic experiments because of its ease in inducing the faults, as well as the assembling and disassembling. Before inserting the bearings inside the housing, each bearing is properly lubricated, and the system is run for 20 minutes prior to the data collection. Each bearing is tested at five rotational speeds: 600, 900, 1200, 1500, and 1800 rpm.

The numerical simulations of the mathematical model are also run to compare its results with the experimental results. To simulate the effect of a fault, as described earlier, an impulse train at the proper fault frequency is applied, as an external excitation, to the governing equations of motion (2.7). The amplitude of the pulse train is assumed to be 50% more than that of the RMS of the normal signal that presents a small damage effect. Then the solutions of (2.7), at different shaft speeds, are employed for computing the Lyapunov exponents, correlation dimensions, and information entropy.

The fault periodic impulse leads to a greater deviation of the phase plane trajectories. Since the Lyapunov exponent is the average of the trajectories' divergence, the bearing faults result in an increase of the Lyapunov exponent. Figure 4.5 shows the Lyapunov exponents, obtained experimentally and numerically. Figure 4.5 demonstrates that the localized faults in a bearing manifest themselves by increasing the level of the Lyapunov exponent, as expected. Although increasing the rotational shaft speed raises the level of the Lyapunov exponent in a normal bearing, the difference between the exponent of a healthy bearing and that of a damaged bearing remains at a distinguishable level. The level of the Lyapunov exponent in the experimental results, due to existing noise in the system, is higher than that of the simulated exponents. However, the existing similarity in the trend of the simulation and the experimental results also validates the behavior of the developed model. Furthermore, since the rolling elements bearings exhibit periodic behavior at low speeds (for the current test bearing <600 rpm), the effect of the fault on Lyapunov exponents is only visible within a medium-high shaft speeds (>600 rpm).

The correlation dimension is very sensitive to periodic motion, and the level decreases as a result of any existing periodic signal. Since the effect of bearing damage appears as a periodic signal, any localized defect, theoretically, leads to a reduction of the correlation dimension. Likewise, the virtual faults are modeled as an impulse train at the related characteristic frequency of a fault in the governing equations of motion.

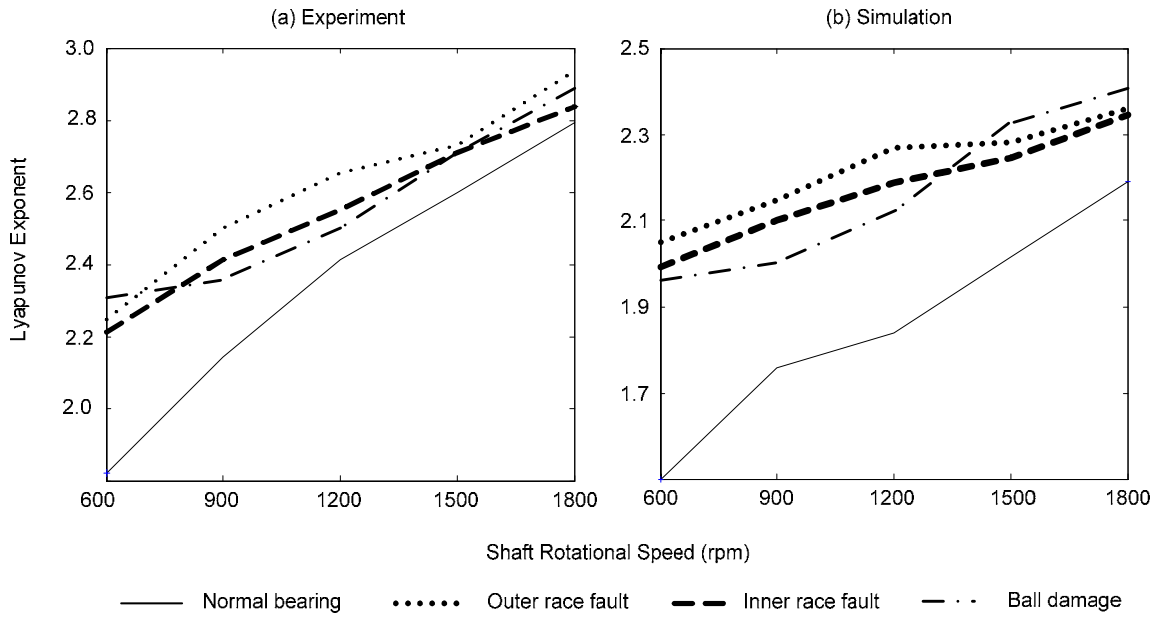

Figure 4.5. Effect of the localized defects on the Lyapunov exponent (experimental and simulation results)

Figure 4.6 depicts the experimental and simulation results of the correlation dimension for different types of faults. To compare the numerical results with the experimental measurements the same length of reconstructed vector, delay, and vector spacing are used for numerical simulations. This is the reason that although the system has only five dimensions the simulated correlation dimension is within the range of 7 to 9. The correlation dimension of a normal bearing relatively remains within a constant range, particularly in the experimental results. An inner race fault significantly decreases the correlation dimensions for the measured and simulation data. The rolling element damage reduces the dimension of the system at all the tested speeds; however, the reduction is more pronounced at higher shaft speeds. The outer race damage does not exhibit a significant variation in the level of the correlation dimension in the experimental results. Also, the weak effect of the outer race fault is due to its low frequency periodicity as observed in Figure 4.4. Similarly, the results of the correlation dimension are only valid for the chaotic range of oscillations, for this particular bearing, higher than 600 rpm. The fact that the correlation dimension for a normal bearing is independent of the shaft speed

makes it an applicable tool for the diagnosis of localized fault of bearings in variable speed systems.

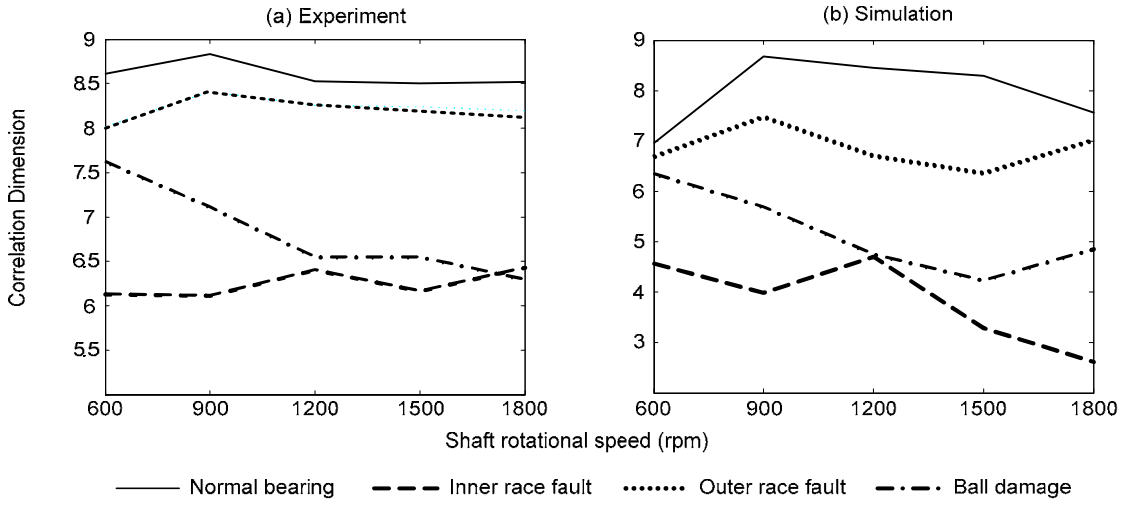

Figure 4.6. Effect of the localized defects on the correlation dimension (experimental and simulation results)

In the previous section, it was mentioned that the information entropy of a chaotic system is proportional to the summation of the system's positive Lyapunov exponents. The above study confirms the increase of positive Lyapunov exponents due to the propagation of the damage in a bearing. Consequently, it is expected that the occurrence of damage in the bearing to increase the level of the information entropy.

The calculation of the information entropy from the experimental data is much simpler and faster than computing the largest Lyapunov exponent. In addition, since the increase of all the exponents influences the variation of the information entropy to a larger extent, this feature should be more sensitive to the damage than the largest Lyapunov exponent. Therefore, the information entropy has the potential to be a suitable candidate for bearing fault indication. Figure 4.7 presents the variation of the information entropy due to the existence of the physical and simulated damage in the bearing's components.

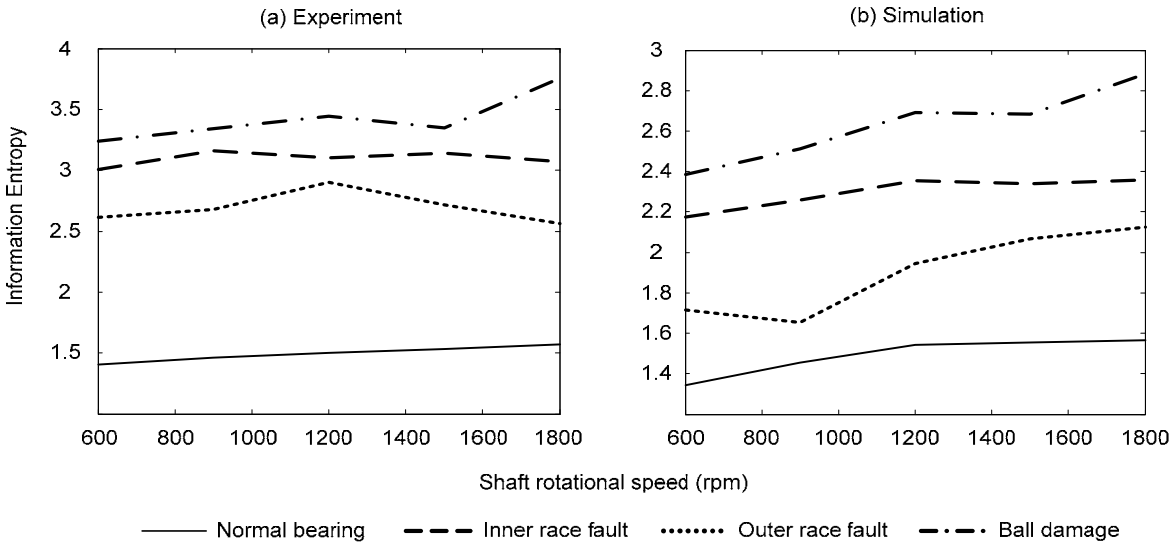

Figure 4.7. Effect of the localized defects on the information entropy (experimental and simulation results)

As expected, existing faults in bearing components manifest themselves by raising the level of the information entropy. Figure 4.7 shows that the effect of the faults is more significant in the information entropy than the largest Lyapunov exponents due to the contribution of several exponents to this chaotic indicator. Once again, the results are valid at speeds higher than 600 rpm, and the level of the information entropy increases at higher speeds.

4.2.2 Imbalance and Misalignment

In addition to changes in chaotic indicators due to faults in bearing components, they also change due to improper function or mounting of the whole system, for example due to imbalance and misalignment. Imbalance results in sinusoidal vibration at the same frequency of shaft speed. This sinusoidal motion can be accompanied by low-level harmonics. For a large amount of imbalance, the periodic motion is dominant. The effect of imbalance on the chaotic attractor is presented in Figure 4.8. The imbalance adds a large periodicity to the system that transfers the strange attractor of Figure 4.8 (a) to the closed orbit of Figure 4.8 (b), which corresponds to a periodic system.

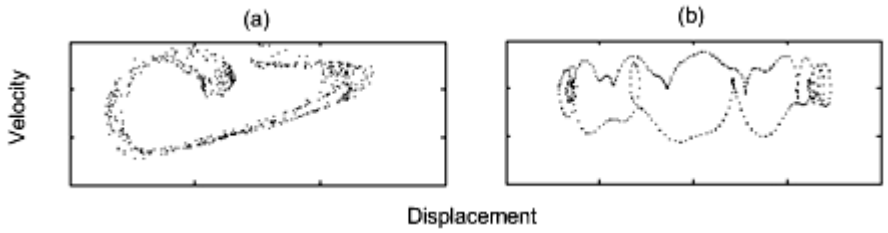

Figure 4.8. Effect of imbalance on the strange attractor: (a) balanced rotor, (b) imbalance rotor (simulation results)

To accentuate the effect of imbalance, the measured vibration is band pass filtered with a centre frequency that coincides with the shaft rotational frequency and bandwidth of ±20 Hz. Since the periodic component in this range is dominant, the value of the Lyapunov exponent, and consequently, the information entropy is almost zero, and thus, is useless as an indicator. However, the correlation dimension results are very promising for imbalance detection. Adding a small imbalance to the system reduces the dimension significantly. This reduction is proportional to the amount of imbalance. The correlation dimensions, computed from the experimental data, are listed in Table 4.1. The reduction in the correlation dimension, in direct relationship to the increase in imbalance, is quite clear. It is concluded that the correlation dimension of a band pass filtered signal is an ideal indicator for the diagnosis of imbalance, even at very small values of imbalance.

Table 4.1. Effect of imbalance on the correlation dimension (experimental measurements)

Imbalance (gr.m)	Correlation Dimension
0	8.11
1.52	5.25
3.01	4.02
3.55	3.57
5.11	2.53

It has been shown that the characteristic frequencies, due to misalignment occur at the even harmonics of the shaft rotational speed. Therefore, in case of the existing

misalignments, the shape of the strange attractor is affected by periodic behavior. Figure 4.9 shows that misalignment transfers the strange attractor, Figure 4.9 (a), to a closed orbit, Figure 4.9 (b), due to the dominant periodicity of the system.

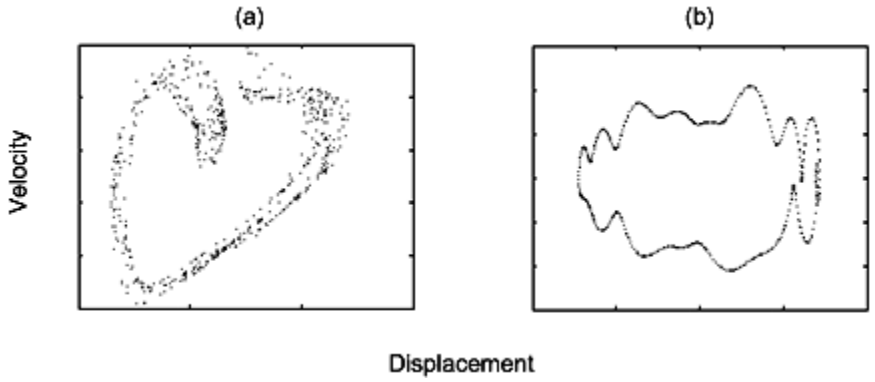

Figure 4.9. Effect of misalignment on the strange attractor: (a) aligned rotor and (b) misaligned rotor

Since the existence of misalignment can create significant periodic motions, it is expected that, similar to imbalance, the level of the correlation dimension drops in proportion to the amount of misalignment. This is evident from the experimental results listed in Table 4.2. Again, in these experiments, the data is band pass filtered with the centre frequency coinciding with the shaft speed and a bandwidth of ±20 Hz. The correlation dimension drops from 8.11 for a system that is normal, to 3.64 for a system with an angular misalignment of α=0.39º. The drastic reduction can be exploited as a feature in system diagnosis.

Table 4.2. Effect of misalignment on the correlation dimension

Fault Description	Correlation Dimension
Aligned system (fault free)	8.11
Parallel misalignment (offset=0.5 mm)	5.69
Angular misalignment (α=0.19º)	3.64
Angular misalignment (α=0.39º)	3.24

4.3 Summary

In this chapter three chaotic measures, the Lyapunov exponent, correlation dimension, and information entropy are employed as fault indicators in rotary machines. The common mechanical failures in rotary machines such as imbalance, misalignment, and bearing damage contribute periodic motions that can disturb, and ultimately, overwhelm, the chaotic vibration of a fault-free system. The simulation and experimental results show the effect of these faults on chaotic attractors and quantifiers. It was shown that these faults increase the level of the Lyapunov exponent and information entropy, while reducing the correlation dimension. This chapter demonstrated that the parameters that describe the chaotic behavior of a system have the potential to be adopted as indices for the diagnosis of faults in rotary machinery.

Chapter 5

Assessment of Bearing Condition Monitoring Techniques

It was shown in the previous chapter that chaotic quantifiers are sensitive to the existence of faults in a bearing's components. To evaluate the diagnosis efficiency of the chaotic indicators, a comprehensive comparison with the most common techniques is conducted in the current chapter. The comparison will be limited to vibration-based techniques. They are the most common detection methods which are categorized as time, frequency, and time-frequency domain, and are briefly described next.

- **Time Domain Analysis**

Time domain analysis, due to its simplicity, has always been an attractive approach for bearing diagnosis. The simplest method is to measure the overall RMS level of the bearing vibration. The resultant values are compared with recommended values to determine the overall health of a bearing [11]; however, this technique is not sensitive to small or early-stage defects [12]. The Crest Factor is the ratio of the peak acceleration to the RMS value. Ingarashi et al. [18] have reported that the level of the crest factor for a normal bearing is approximately five. These authors have proven that the crest factor is a good indicator of small size defects; although, when localized damage propagates, the value of the crest factor decreases significantly due to the increasing RMS. The vibration peak level can also be employed as a monitoring index; but is found to be unreliable for small size defects [17].

The Kurtosis, the fourth normalized statistical moment, corresponds to the peakedness of the data. For an undamaged bearing, this amount is equal to three in the low frequency bands (Appendix II). Many researchers [13, 14, 15, 16] have found the Kurtosis value to be more useful, when it is compared with the RMS, crest factor, and peak value.

The impulse, generated by the impact of the damage, can excite the resonant frequency of the sensor. This effect is studied in either the frequency domain or the time domain. The shock pulse method [17, 20] is based on the measurement of the maximum amplitude of the sensor's resonance in the time domain. Although the shock pulse meters have been accepted by industry [21], their dependency on the bearing bore size and speed limits their application in speed variable systems. Moreover, some researchers have proven that the method is ineffective in detecting defects at low speeds [22]. Hemmings and Smith [19] have proposed a time-averaging technique to reduce the sample size and increase the signal to noise ratio. In this technique, a signal is obtained when the inner race and a ball are aligned at a specific point in the outer race. By averaging a number of samples, the effect of the ball size is reduced, and signal to noise ratio is increased.

The chaos effect is categorized as time-domain analysis; however, little research has been reported regarding bearing diagnosis based on chaotic monitoring indices. Logan and Mathew [8, 9] proposed fractal dimension, Choy et al. [10] utilized the modified Poincare map, and Li and Qu [102] employed a new fault diagnosis scheme based on forward detecting method.

- **Frequency Domain Analysis**

For bearing fault diagnosis, frequency domain, or spectral analysis, is the most popular approach. Many researchers have reported successful results for detecting damaged bearings through spectral analysis. Usually, it is carried out at low-range frequencies and the defects are identified by the change of the spectral amplitude at each of the

characteristic frequencies. Taylor [24] has formulated the sequence of appearing and disappearing spikes in the spectrum. In addition, he has proposed a method for measuring the size of the defects on the raceways. Mathew and Alfredson [17] have offered the amplitude difference between healthy and damaged spectra as a fault diagnosis technique. The envelope detection is a well-defined technique for bearing fault diagnosis. The efficiency of this method has been evaluated by many researchers [26, 27, 28, 29, 32] and can also be combined with an auto detection filter band and spectrum analyzer [33]. Martin and Thrope [29] have suggested the use of the normalized spectral amplitude of an enveloped signal. Ho and Randal [30] have conducted extensive research on the envelope technique. Their work has demonstrated that a Self-Adaptive Noise Cancellation (SANC) method, in conjunction with an envelope analysis improves a bearing's diagnostic results. Braun [107] has proposed a technique that includes decomposing the vibration signal into a generalized periodic function. The key feature of the technique is its insensitivity to structural parameters.

Another approach for bearing fault diagnosis is the High Frequency Resonance Technique (HFRT) [34, 35, 36]. It is similar to the shock pulse method, but instead of measuring the resonance amplitude, the spectral of the resonant signal is examined. This method performs poorly at low shaft speeds.

- **Time-Frequency Domain Analysis**

In signal processing, a number of time-frequency analysis methods, such as the short time Fourier transform and wavelet transform, have been introduced. Of these methods, wavelets have been established as the most widely used technique due to their flexibility and their efficient computational process.

The application of wavelet decomposition for bearing fault diagnosis was first suggested by Li and Ma [42]. Rubini and Meneghetti [44] have used the average of the wavelet amplitude frequencies over a selected band that is not affected by the system's resonance.

Sun and Tang [45] have applied a singularity analysis on the continuous wavelet transform. This method identifies the lines in the wavelet map that converge to singular points at fine scales. Nikolaou and Antoniadis's [48] decomposition method is based on the shifted Morlet wavelet, where the envelope of a signal contains the important features of a defect. Jing et al. [108] have developed a denoising method, derived from Morlet wavelet, for feature extraction that is successfully employed for inner race fault detection. Luo et al. [109] have proposed a fast continuous wavelet decomposition method which, together with autocorrelation enhancement, can be used as an on-line fault detection tool. The application of the discrete wavelet transform for bearing diagnosis has been reported by Morie et al. [46]. Their method is utilized for the detection of single bearing faults. Prabhakar et al. [40] have shown that the discrete wavelet transform can be used as an effective tool for detecting multiple faults.

The current section presents a comprehensive comparison of a number of acceptable monitoring techniques in the literature. The investigation is conducted by using the same vibration data that are measured from different bearing conditions: inner race fault, outer race fault, or roller fault, under similar conditions of load and speed. The diagnosis methods are selected from the time domain, frequency domain, wavelets, and the chaotic analyses introduced in the previous chapter. All the techniques are coded in the Matlab[1] environment. Since the goal of this work is to introduce monitoring indices with a low speed and load dependency, the effect of load and speed variation on chosen indicators is also studied.

5.1 Data Acquisition and Signal Pre-Processing

The bearing test apparatus used in this investigation is similar to the one shown in Figure 3.8. To assess the effect of bearing faults on different fault indicators, vibration data are obtained from experiments by using the following seven bearing conditions:

[1] Copyright the MathWorks Inc., Version 6.5, Release 13

- Normal bearing
- Small inner race fault, dimple foot print diameter 1.1 mm (damage area 0.95 mm^2, Figure 5.1 (b)), applied by a hardness testing machine
- Large inner race fault, total wear area 4.1 mm^2 , formed by grinding as shown in Figure 5.1 (a)
- Small roller damage, dimple foot print diameter 0.95 mm (damage area 0.71 mm^2, Figure 5.1 (d)) , applied by a hardness testing machine
- Large roller damage, indentation diameter 2.1 mm, (area 3.46 mm^2 , Figure 5.1 (c)), created by an electro discharge machine
- Small outer race damage, localized wear 1.8 mm^2, created by a grinding machine
- Large outer race damage, damaged area 3.1 mm^2, generated by a grinding machine, Figure 5.1 (e)

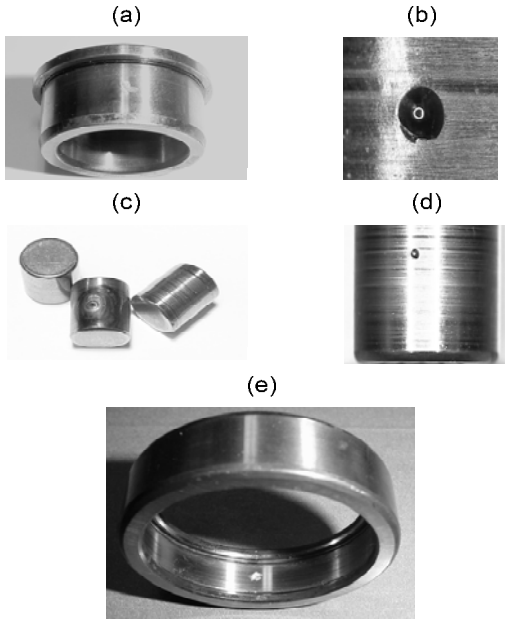

Figure 5.1. Bearing induced localized faults

The faults were induced at the drive-end bearing, model SKF NJ204ECP. Before the bearings were inserted inside the housing, each bearing was properly cleaned of metal chips, well lubricated, and run for 20 minutes prior to the data collection. To compare the results, each bearing was tested at the same rotation speed of 1500 rpm and radial load of

23 N. The vibration was measured with a Dytran 3035AG accelerometer with a sensitivity of 100 mV/g mounted on the bearing housing. A proximity sensor mounted close to the rotating disk as a phasor, provided a one-pulse-per- revolution impulse for the signal averaging process. The accelerometer's signal was amplified by the Dytran 4105C, and low pass filtered. The filter cut-off frequency for the low sampling frequency of 6000 Hz was chosen to be high enough to capture the fifth harmonic of the inner race frequency at 850 Hz. For the high resonant frequency analysis, the signal was band pass filtered at the centre of 24 kHz. In this application, the vibration data was measured at the sampling frequency of 72 kHz, and the anti-aliasing filter was set at 30 kHz.

5.2 Fault Index Extraction and Signal Processing Techniques

From the various diagnostic techniques in the literature, the experiments conducted, here, are limited to the most acceptable monitoring methods. They include the Kurtosis, crest factor, envelope analysis, HFRT, Lyapunov exponent, correlation dimension, normalized information entropy, and the continuous and discrete wavelet transforms. All the diagnostic algorithms are coded in Matlab environment. The formulation and implementation of each method is briefly explained below.

5.2.1 Kurtosis

The different statistical moments of the vibration data, widely used as a bearing monitoring index, is calculated by

$$M_k = \int_{-\infty}^{+\infty} \left(x - \bar{x}\right)^k P\left(x\right) dx \tag{5.1}$$

M_k is the k-th statistical moment of the data about the mean $\bar{x}$, and $P(x)$ is the probability distribution function. The most common form, Kurtosis, is the fourth moment of the data normalized by the square of variance (= RMS^4 for zero mean data). This index is commonly used as a measure of the vibration peakedness, caused by the localized damage of the bearings. The vibration data of a healthy bearing exhibits a normal

distribution; thus, the kurtosis is equal to three (Appendix II). The propagation of damage in the bearing, which generates more peaks and increases the RMS, alters the Kurtosis level.

To compute the Kurtosis, the vibration signal is collected at a sampling frequency of 6000 Hz for 10 seconds. The measured data is then digitally low pass filtered at a cut-off frequency of 1000 Hz. The Kurtosis is obtained from

$$\text{Kurtosis} = \frac{\sum x^4}{\sigma^2} \tag{5.2}$$

where x is the zero-mean filtered vibration signal and σ is the variance.

5.2.2 Crest Factor

The crest factor is the ratio of the maximum amplitude to the RMS value. This monitoring index determines the level of energy associated with the impact of a faulty bearing. The crest factor is capable of detecting powerful impacts in a low energy time domain signal. Since the impacts appear at a high frequency range, crest factor is extracted from the raw vibration signal sampled at 6000 Hz by the following simple formulation:

$$\text{Crest factor} = \frac{\max(x)}{\text{RMS}(x)} \tag{5.3}$$

5.2.3 Envelope Analysis

When a rolling element strikes a localized defect, a pulse is generated, exciting the natural frequency of a bearing's components, housing, and the overall assembled structure. The generation frequency of this pulse is called the characteristic frequency. Most of the defect detection techniques in the frequency domain are derived from the study of these frequencies, which are dependent on the location of the fault. The frequencies for a rolling element bearing are:

$$\text{Ball Pass Frequency of Outer race (BPFO)} = \frac{Nf_s}{2}\left(1-\frac{D_b\cos\alpha}{D_m}\right)$$

$$\text{Ball Pass Frequency of Inner race (BPFI)} = \frac{Nf_s}{2}\left(1+\frac{D_b\cos\alpha}{D_m}\right)$$

$$\text{Ball Spin Frequency (BSF)} = \frac{D_m f_s}{D_b}\left(1-\left(\frac{D_b}{D_m}\right)^2\cos^2\alpha\right) \tag{5.4}$$

$$\text{Fundamental Train Frequency or cage frequency (FTF)} = \frac{f_s}{2}\left(1-\frac{D_b\cos\alpha}{D_m}\right)$$

D_b and D_m are the roller and pitch diameters, N is the number of rolling elements, α corresponds to the contact angle, and f_s is the shaft rotational frequency.

Monitoring the level of the vibration spectral amplitude in narrow-band characteristic frequencies can be an effective method to diagnose a bearing's faults. In this analysis, which is conducted at low frequencies, a defect is identified through a change in the spectral amplitude at the defect frequencies. Raceway defects are identified in a narrow-band spectrum at the BPF. As the defect develops, the spikes are modulated by the shaft frequency, and the fault is detected at the BPF accompanied by shaft frequency sidebands. When the damage propagates, the spikes become less pronounced. The defects in the inner and outer races exhibit similar behavior. The rolling element defects are identified at the BPF and its multiples. Usually, the characteristic frequencies are modulated with either a rotational frequency, or other machine frequencies; therefore, the spectral analysis of the amplitude demodulated signal is more efficient. An envelope detector is used to demodulate the signal by removing all the high frequency components. The envelope of signal *x(t)* is obtained by computing the amplitude of a complex signal, formed from *x(t)* as the real part, and its Hilbert transform as the imaginary part. The Hilbert transform of a time domain signal is defined as

$$\text{Hilbert}[x(t)] = \tilde{x}(t) = \frac{1}{\pi}\int_{-\infty}^{+\infty}\frac{x(\tau)}{t-\tau}\,d\tau \tag{5.5}$$

Therefore, the envelope of signal *x(t)* is expressed as

$$\text{Envelope}\left[x(t)\right] = \sqrt{x^2(t) + \tilde{x}^2(t)} \tag{5.6}$$

The spectral analysis of the enveloped signal is widely employed for bearing fault diagnosis.

5.2.4 High Frequency Resonant Technique (HFRT)

Another approach for the diagnosis of rolling element bearing faults is the High Frequency Resonance Technique (HFRT). The impulses, created by the strikes of the rolling elements on the defects, have short durations with a low energy level that is distributed over a broad-band. However, the generated impulses have enough energy to excite the resonance of the vibration transducer spring-mass system. The signal of the resonance is amplitude modulated at the defect frequencies.

In this method, the original signal is band pass filtered around the resonant frequency (20-26 kHz), and the defect frequencies are extracted by the amplitude demodulation technique. This process accentuates the bearing defect impulses in the time domain and the corresponding spectral lines at the characteristic frequencies. The amplitude demodulation of a digital signal is obtained through its Hilbert transform. The procedure is detailed in Figure 5.2.

The high amplitude values of an envelope spectrum at a particular characteristic defect frequency, obtained by the previous method, indicate the occurrence of a defect. The location of the defect can be determined by its unique characteristic frequency.

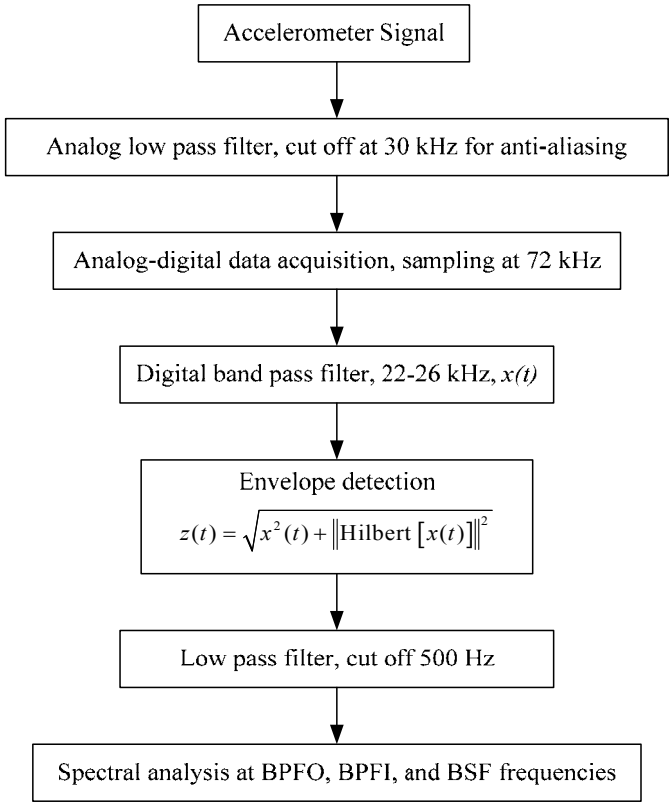

Figure 5.2. HFRT signal processing flow diagram

5.2.5 Lyapunov Exponent

Due to the damping effect, the divergence of the reconstructed trajectories is only locally exponential. Thus, to define a measure of this divergence, the exponential growth is averaged at different points of the trajectories. This method, originally proposed by Wolf et al. [103], starts with a point on the reference trajectory and a point on a nearby trajectory with an initial distance of $d_0(t_0)$. At later time t_1, the initial distance evolves to $d(t_1)$. When $d(t_1)$ becomes too large, a new replacement element on a nearby trajectory should be considered. The replaced point must satisfy two criteria: the separation distance $d_0(t_1)$ and the angular separation between the evolved and replacement point should be small. In this case, the Lyapunov exponent is obtained from

$$\lambda = \frac{1}{t_M - t_0} \sum_{k=1}^{M} \log_2 \frac{d(t_k)}{d_0(t_{k-1})} \tag{5.7}$$

where M is the total number of replacements.

For the current application, the accelerometer signal is low pass filtered at 2000 Hz and recorded by an A/D data acquisition card at a sampling frequency of 6000 Hz. The digitized data is re-sampled at 10 Hz to obtain the Poincare points. To construct the trajectories, the Poincare points are organized into two-element vectors with an embedding dimension of 2 which results in 1190 reconstructed vectors. The largest Lyapunov exponent is then computed through the discussed method by assuming the replacement criteria listed in Table 5.1.

Table 5.1. Replacement criteria for calculating the largest Lyapunov exponent

Minimum separation	0.0001
Maximum separation	0.1
Maximum orientation angle	30°

5.2.6 Continuous Wavelet Map

The wavelet transform is a tool that splits data into different frequency components, and then each component can be studied with a resolution matched to its scale. The use of the wavelet transform is efficient for fault diagnosis, since the technique gives the information about the signal in the time and the frequency domains. The Continuous Wavelet Transform (CWT) of signal $x(t)$ is obtained from

$$\mathrm{CWT}(\alpha, \tau) = \frac{1}{\sqrt{\alpha}} \int_{-\infty}^{+\infty} x(t) \psi^*_{\alpha,\tau}(t)\, dt \tag{5.8}$$

where $\psi^*(t)$ denotes the complex conjugate of mother wavelet $\psi(t)$ such that

$$\psi_{\alpha,\tau}(t) = \frac{1}{\sqrt{\alpha}} \psi\left(\frac{t-\tau}{\alpha}\right) \tag{5.9}$$

Parameters α and τ are scale and translation indices which corresponds to mutual frequency and the time shifting, respectively. The crucial aspect in the calculation of the wavelet is to select the appropriate mother wavelet. In bearing fault diagnosis through a series of tests, it is found that the Morlet wavelet yields superior results. The reason is found in the existing similarity between the shape of this wavelet, Figure 5.3, and the generated signal due to the strike of damage with the rolling elements.

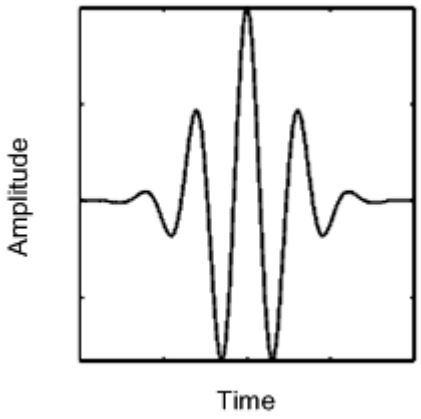

Figure 5.3. Morlet Wavelet

The Morlet wavelet is defined in the time domain as a sinusoidal wave, multiplied by a Gaussian function. The Morlet wavelet is expressed as

$$\psi(t) = ce^{-\sigma^2 t^2} e^{j2\pi f_0 t} \tag{5.10}$$

This wavelet has the shape of Gaussian window in the frequency domain, where f_0 is the centre frequency, and σ determines its width. Parameter c is chosen as

$$c = \frac{\sigma}{\sqrt{\pi}} \tag{5.11}$$

The wavelet amplitude map can be determined from (5.8) in the time-scale domain. In this investigation, to increase the signal-to-noise ratio, the time domain signal is averaged based on the phasor and one revolution of the cage to magnify the effect of the fault. The wavelet amplitude map is then calculated according to the linear scale, and displayed in

time-frequency plane. The wavelet amplitude map is an effective tool to visualize the existence of damage in bearing components.

5.2.7 Discrete Wavelet Transform

The Discrete Wavelet Transform (DWT) of a vibration signal reflects the existence of impulsive behavior by increasing the wavelet coefficients. Therefore, the DWT coefficients are suitable candidates for bearing diagnosis and prognosis. The DWT is derived from the discretization of the continuous wavelet, and the wavelet coefficients are given by

$$\text{DWT}\ (j,k) = \frac{1}{\sqrt{2^j}} \int_{-\infty}^{\infty} x(t) \psi^* \left(\frac{t - 2^j k}{2^j} \right) dt \tag{5.12}$$

where *x(t)* presents the time domain signal, ψ^* denotes the mother wavelet complex conjugate, and $2^j, 2^j k$ represent the scale and the translation, respectively. In each step of the wavelet decomposition, the signal is high/low pass filtered, resulting in vectors *CA*/*CD*. The *CA* vector represents the approximate coefficients, whereas *CD* consists of detailed coefficients [110]. In this work, the Maximum of Approximate Coefficients Wavelet (MACW), decomposed up to four levels by using the Daubechies4 wavelet (*db*4) of the measured vibration, is used as the monitoring index. The Daubechies family wavelets (*dbN*) are efficient to study impulsive and fractal systems. Figure 5.4 shows the scaling and wavelet function of *db4*.

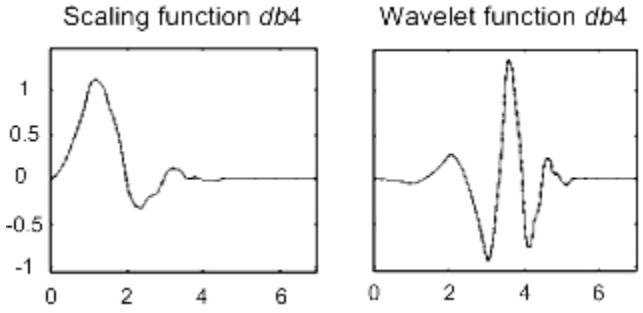

Figure 5.4. Scaling and wavelet function of *db4*

5.2.8 Correlation Dimension

The characteristic of this chaotic monitoring index was discussed in detail in section 4.1.2. Here, the practical calculation steps are explained. The measured vibration is recorded at the sampling rate of 6 kHz. The phase space vectors are then generated from the raw time series signal as follows:

$$\begin{aligned} X_1 &= \{x_1, x_{\tau+1}, ..., x_{m\tau+1}\} \\ X_2 &= \{x_{\alpha+1}, x_{\alpha+\tau+1}, ..., x_{\alpha+m\tau+1}\} \\ &\vdots \\ X_M &= \{x_{M\alpha+1}, x_{M\alpha+\tau+1}, ..., x_{M\alpha+m\tau+1}\} \end{aligned} \tag{5.13}$$

where X_M are reconstructed vectors from the time signal, vector length m = 15, internal vector delay, $\tau = 8$,and vector spacing $\alpha = 15$ which are obtained by a number of experiments. The total number of reconstructed vectors, M, are found from

$$M = \text{Integer}\left(\frac{N - m\tau}{\alpha}\right) - 1 \tag{5.14}$$

where N is the length of the measured data.

After calculating all the distances between the generated vectors, $\|X_j - X_i\|$, the range between the longest and shortest distance is divided by 100 to determine the diameters of the *m-dimensional spheres*, ε. Subsequently, the correlation function (4.3) counts the number of points which exist in the constructed sphere at each point X_i. Finally, the results are plotted on the $\log C_d(\varepsilon)$ - $\log \varepsilon$ plane. The slope of the generated curve represents the correlation dimension value and can be obtained by using the least square method.

5.2.9 Normalized Information Entropy

It was discussed in Chapter 4 that an increase in the information entropy takes place in a damaged bearing. Meanwhile, it was found that this monitoring index highly depends on the rotating speed, as shown in Figure 4.3.

Calculating the information entropy from the experimental data is much simpler and faster than computing the largest Lyapunov exponent. In addition, since the increase of all the exponents influences the information entropy, this feature should manifest the presence of damage more clearly than a single Lyapunov exponent. It should be realized, however, that since the vibration of the bearing is more periodic than chaotic at low speed ranges (for the current test bearing, less than 800 rpm), the application of the information entropy as a fault indicator is limited to medium to high speed rotors (for the current research >800rpm). To decrease the speed dependency, the information entropy is normalized by the RMS of the signal.

To calculate Normalized Information Entropy (NIE), the accelerometer signal is low pass filtered at 2 kHz and then digitized by an A/D data acquisition card at the sampling frequency of 6 kHz. The recorded data is reconstructed with a time delay of 0.71 seconds. The probability of finding a point in the subinterval, P_i, is determined by (4.5). After the information entropy of data series is obtained from (4.6), the resultant information entropy is normalized by the RMS of the vibration signal.

5.3 Experimental Results and Discussions

Tests are conducted at a constant speed of 1500 rpm and static load of 23 N. The rotor is very well balanced and extra care is taken to isolate the bearing signal from the surrounding noise. In these tests, the vibration is online monitored and the data collected only after passing the transient situation.

Two quantified criteria are used for comparing the efficiency of each monitoring index. These criteria are computed for 35 sets of data for each bearing conditions. To compare the variation of indices, the value of each index is normalized before computing the variance.

- The variance of the normalized computed indices for each bearing condition

$$\text{Variance} = \frac{\sum_{i=1}^{35}\left(I_i - \overline{I}\right)^2}{35} \tag{5.15}$$

where I is the normalized monitoring index.

- The average ratio of each index to that of a normal bearing for various heath conditions

$$\Re_1 = \frac{\overline{I}_{\text{Small damage}}}{\overline{I}_{\text{Normal}}} \qquad \Re_2 = \frac{\overline{I}_{\text{Large damage}}}{\overline{I}_{\text{Normal}}} \qquad \Re_3 = \frac{\overline{I}_{\text{Large damage}}}{\overline{I}_{\text{Small damage}}} \tag{5.16}$$

The first measure, the variance, corresponds to the statistical dispersion of the computed index around the mean value. Low variance signifies the repeatability and robustness of the monitoring index. The evaluation measures, $\Re_1$, and $\Re_2$, correspond to the change of the index for a small and a large damage with respect to the normal condition. $\Re_3$ reflect the change of the averaged index, when the level of damage increases from small to large. Therefore, the higher ratio reflects the sensitivity of the monitoring index. Since the level of the correlation dimension decreases for the faulty bearing, the associated values in the table are $\Re_1^{-1}$, $\Re_2^{-1}$, and $\Re_3^{-1}$.

The test results of the various bearing conditions, utilizing the preceding fault indices, are summarized in Table 5.2. Symbols V_N, V_S, and V_L denote the index variance of a normal bearing, a bearing with small damage, and a bearing with large damage. In addition, the following abbreviations are used in the comparison Table 5.2.

Max. Approximate Coefficient of Wavelet	*MACW*	Kurtosis	*K*
Crest factor	*CF*	Correlation dimension	*CD*
Envelope analysis	*EA*	Normalized Information Entropy	*NIE*
High Frequency Resonance Technique	*HFRT*	Lyapunov exponent	*LE*

The results of Table 5.2 are discussed for each type of fault, obtained at the same speed of 1500 rpm and radial load of 23 N. For each type of bearing fault, each figure presents the level of the monitoring indices, corresponding to a normal bearing (black line), a

bearing with a small fault (blue line), and a bearing with a large fault (red line). The average value of each index is shown by dotted line in the same figure. Except the EA and HFRT plots which are generated for one set of data from each bearing conditions, the other figures present the results of the related extracted fault feature for 35 sets of data. The wavelet amplitude map generated by CWT presents only a visual picture of the location of the fault.

5.3.1 Inner Race Fault

As expected, the average of the healthy bearing Kurtosis, Figure 5.5 (a), is close to three. The small dimple generates more peaks in the vibration signal, increasing the level of Kurtosis to 4.2. When the damage is excessive, the continuous generation of impulses in the vibration signature increases the variance of the signal, subsequently diminishing the pattern of peaks. In this case, the level of Kurtosis drops to one. Although the small values for V_N, V_S, and V_L indicate the repeatability, the inconsistency in reflecting the size of the damage is the major weakness of Kurtosis. The same trend is observed in the CF, Figure 5.5 (b). The small damage increases the CF; however, a large damage produces approximately the same level of peaks, while significantly raising the level of the RMS. The combination of these two effects decreases the CF level.

The envelope analysis highly depends on the running speed. Even a small variation in speed, caused by the motor, slippage of the belt, or backlash in the coupling, can affect the frequency of the fault, and hence, reduce the repeatability of the index as represented by high variance in Table 5.2. Envelope analysis is successful to distinguish different levels of faults, Figure 5.5 (c), with the high ratios $\Re_1$ and $\Re_2$. The damage impacts generated on the inner race passes through rotating rollers. Therefore, the HFRT results are similar to the EA with higher sensitivity to speed which causes more dispersion in the results, as shown in Table 5.2, and Figure 5.5 (d).

The generated impulses, due to the strike of the fault and its mating surface, affect the vibration of the bearing and reposition the location of the Poincare points. Accordingly, due to this divergence of the Poincare points in the reconstructed time series, the deviation of the trajectories increases, resulting in higher values of the Lyapunov exponents, as seen in Figure 5.5 (e). Although the small variances denote the consistency of the index, the small difference between the damaged and the normal Lyapunov exponents clearly shows the insensitivity of this monitoring index. Discrete wavelet coefficients are very sensitive to the impacts in the vibration signal. This sensitivity is evident in Figure 5.5 (f), and the high values of $\Re_1$, $\Re_2$, and $\Re_3$ listed in Table 5.2. The repeatability of MACW is within an acceptable range, which can be deduced from the low variance values.

The correlation dimension is very sensitive to periodic motion, and the level decreases as a result of any existing periodic signal. Since localized defects add periodicity to the vibration signals, any surface damage inside the raceways can result in the reduction of the correlation dimension as seen in Figure 5.5 (g). The low variances of different bearing conditions and relatively high $\Re_1^{-1}$, $\Re_2^{-1}$, and $\Re_3^{-1}$ ratios express the efficiency of the correlation dimension for fault detection. The NIE of a damaged bearing is higher than that of a fault-free bearing, according to the rise in the Lyapunov spectrum in Figure 5.5 (h). A remarkable variation of the NIE shows the sensitivity of this monitoring index. The existence of a small fault is found by comparing the wavelet amplitude maps, Figure 5.5 (J) and (k); however, due to the complexity of image processing, the wavelet amplitude can be employed only as a visualization tool for fault detection.

Table 5.2. Comparison among different techniques, speed 1500 rpm, radial load 23 N

	V_N	V_S	V_L	$\Re_1$	$\Re_2$	$\Re_3$
			Inner Race Damage			
K	0.0891	0.0371	0.0298	1.0918	-	-
CF	0.0679	0.2829	0.0509	1.2861	-	-
EA	0.2165	0.1701	0.2249	2.0635	3.4372	1.6657
HFRT	0.2971	0.2666	0.2453	2.0244	3.7184	1.8368
LE	0.0114	0.0113	0.0138	1.0302	1.0669	1.0356
MACW	0.1243	0.1029	0.0488	3.5240	8.8324	2.5063
CD	0.0234	0.0480	0.0785	1.3507	1.6167	1.1969
NIE	0.0267	0.0128	0.0127	5.7528	9.2541	1.6086
			Outer Race Damage			
K	0.1080	0.0658	0.0189	1.8839	-	-
CF	0.0637	0.1036	0.0547	1.0096	-	-
EA	0.1487	0.2990	0.1513	2.1178	12.9380	6.1092
HFRT	0.2424	0.2505	0.2534	0.5973	1.9102	3.1981
LE	0.0114	0.0196	0.0178	1.0069	1.0390	1.0319
MACW	0.1040	0.1359	0.0465	4.2146	8.7142	2.0676
CD	0.0282	0.0981	0.0810	1.3728	2.6129	1.9033
NIE	0.0250	0.0305	0.0123	3.7931	6.1667	1.6257
			Rolling Element Damage			
K	0.0891	0.0715	0.0993	4.9300	5.4481	1.1051
CF	0.3679	0.2258	0.3302	0.7305	1.0728	1.4686
EA	0.1794	0.2118	0.1893	2.9732	8.3908	2.8221
HFRT	0.2424	0.2455	0.2210	2.4371	3.7007	1.5185
LE	0.0114	0.0115	0.0136	1.0086	-	-
MACW	0.2243	0.0751	0.1088	3.2857	3.8571	1.1739
CD	0.0234	0.0312	0.0423	1.3278	1.3728	1.0338
NIE	0.0467	0.0345	0.0265	2.8174	3.2932	1.1688

5.3.2 Outer Race Fault

The behavior of an outer race fault is similar to that of inner race damage. Since the location of the defect is stationary and the probability of impact generation is high, the effect is more pronounced in the Kurtosis, Figure 5.6 (a), by the larger increase from 3 to almost 7 for small defect. For the same reason, the effect of the fault in HFRT and particularly in EA is more obvious, as conveyed in Figure 5.6 (c) and (d). Figure 5.6 (b) exhibits the failure of CF to diagnose the outer race damage, since the level of the normal

and small damage CF is unrecognizable. A significant rise is present for the level of large damage in the MACW plot in Figure 5.6 (f), whereas acceptable results are also obtained for the small fault.

Since the location of the fault is fixed, the strikes between the rolling elements and the damaged area are more frequent. In other words, a heavy periodicity is added to the vibration signal which results in a significant decrease in the correlation level, as shown in Figure 5.6 (g). The existence of a highly periodic signature diminishes the effect of the divergence of the trajectories. As a result, the presence of a fault in the outer race, especially for faults located in the load zone, has a small effect on the Lyapunov exponent in Figure 5.6 (e). On the other hand, much better results are observed in the NIE graphs in Figure 5.6 (h). All the variances are similar to that of the inner race fault. Again the wavelet amplitude map reveals the presence of the small damage in the outer race.

5.3.3 Rolling Element Damage

Sine the damage can hit either the inner or the outer ring, the probability of the generation of strikes for a bearing with roller damage is high, compared with that of an inner race fault or stationary outer race damage. As a result, random peaks with less energy happen more frequently in the vibration signal, which increasing the peakedness of the signal and its measured Kurtosis, as observed in Figure 5.7 (a). The Kurtosis level is significantly changed from 3 to 23 for a small damage and 25 for a large damage. Since the opportunity of incurring small and large peaks is similar, the level of Kurtosis for a small and a large defect is close. The small variances indicate the repeatability of this method. The level of the CF depends mostly on the efficiency of the incurred strike between the damage and the races. Due to this random behavior, the CF results fluctuate greatly and are inaccurate, as portrayed in Figure 5.7 (b). Figure 5.7 (c) illustrates the promising results of EA. Likewise, the effect of the faults is well pronounced in the spectrum of HFRT in Figure 5.7 (d).

The impulse generation results in the divergence of the trajectories; but, due to the randomness of the occurrence, the computed Lyapunov exponent is not steady in Figure 5.7 (e). The effect of increasing Lyapunov exponent is more visible and steadier in the NIE in Figure 5.7 (h); however, the data are more scattered, compared with the inner race and the outer race results.

As it is expected, the periodicity added to the vibration signal, due to the unpredictability of the generated strikes, is less than that of the inner/outer race. Consequently, the decrease in the correlation dimension is low, as displayed in Figure 5.7 (g). Due to the nature of fault, the wavelet amplitude map does not portray the damage; however, a trace of damage is visible in the Figure 5.7 (k).

Other characteristics of the monitoring indices such as the effects of operating conditions, damage size, and so on can also be examined. But, what is most important is to realize that the MACW, CD, and NIE, for any type of damage studied here, present more consistent results. In the following section, the effect of the speed and load on these three selected indices is examined.

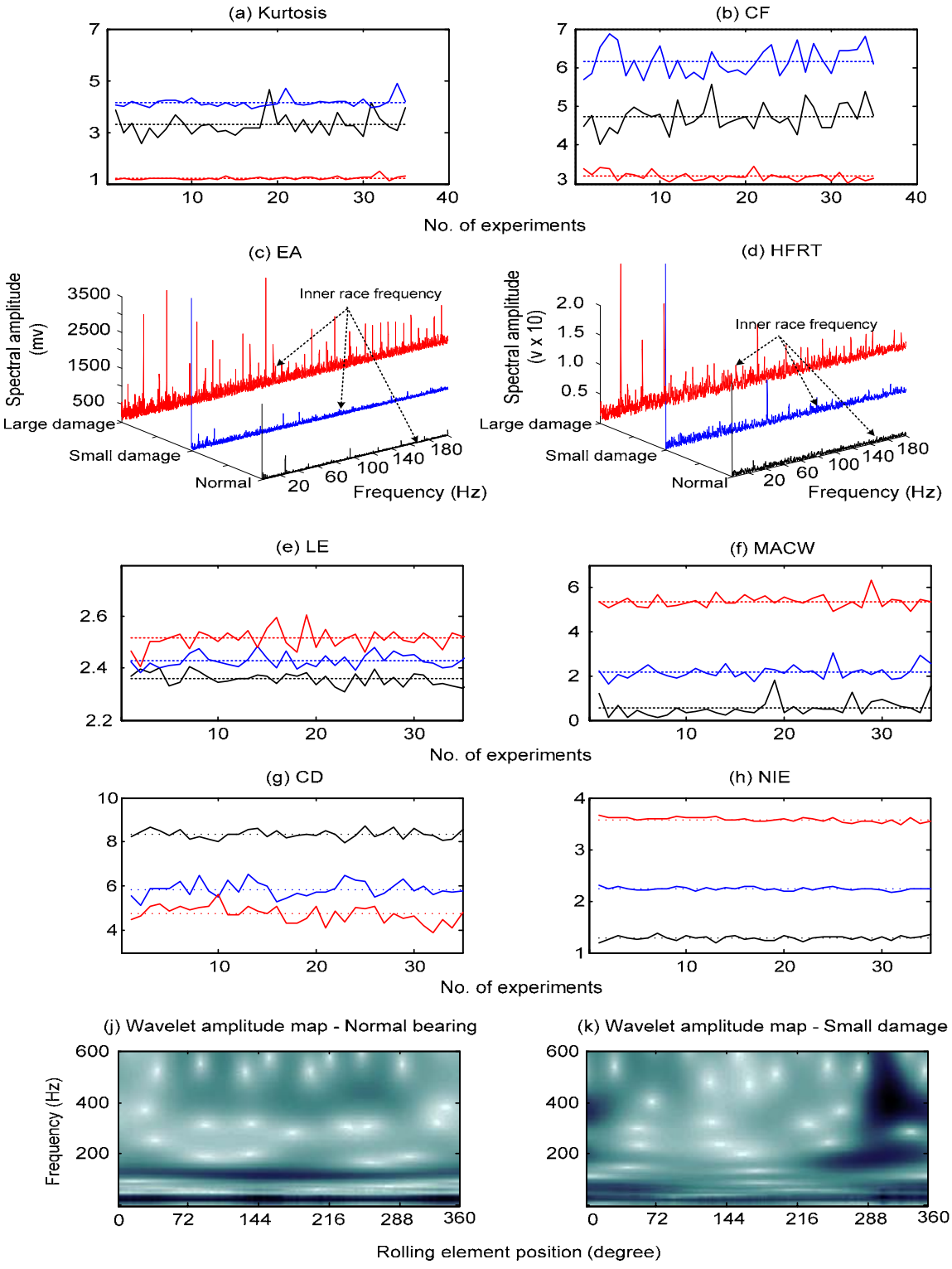

Figure 5.5. Condition monitoring of bearing with inner race fault (black: normal, blue: small damage, and red: large damage)

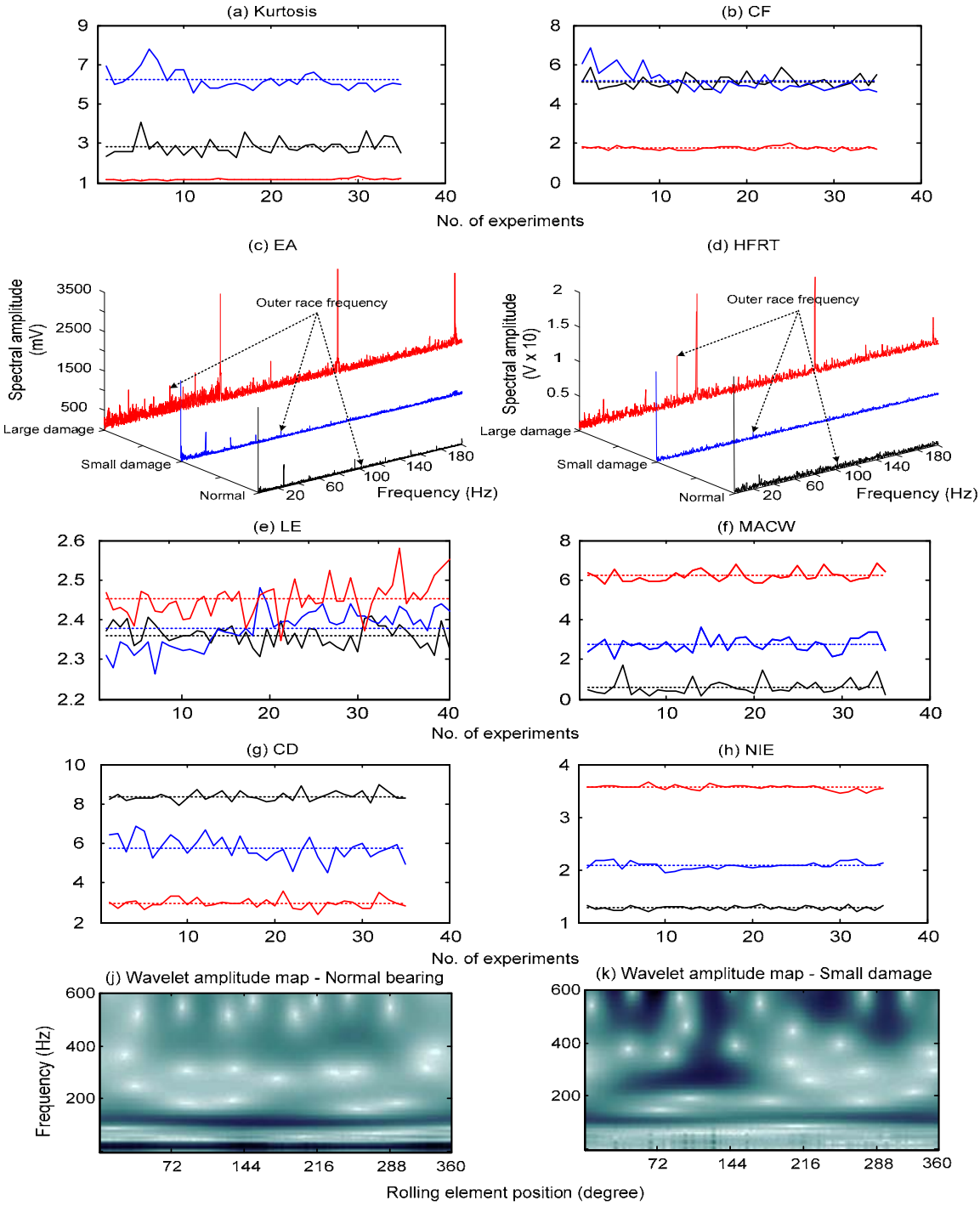

Figure 5.6. Condition monitoring of bearing with outer race fault ((black: normal, blue: small damage, and red: large damage)

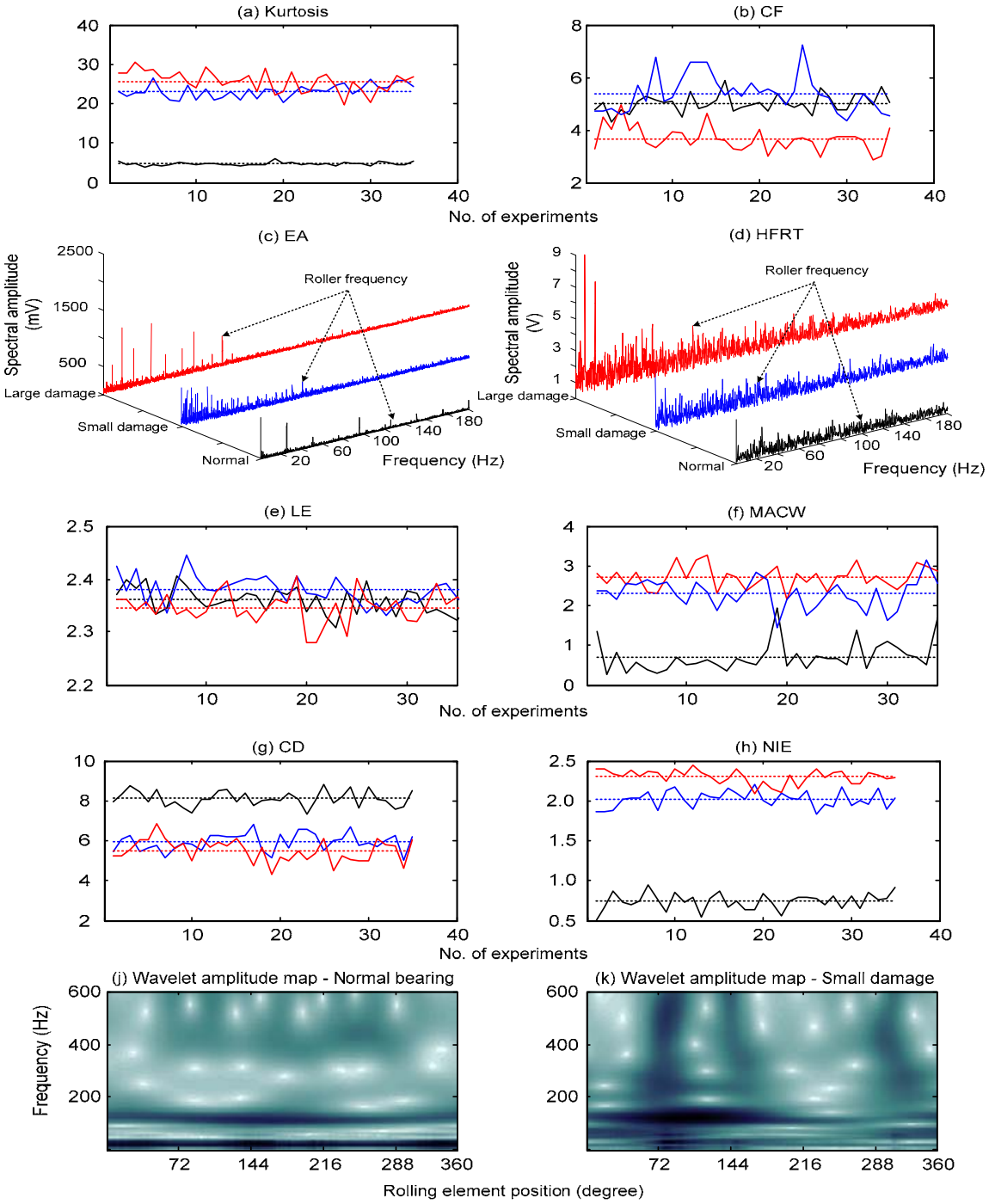

Figure 5.7. Condition monitoring of bearing with rolling element damage (black: normal, blue: small damage, and red: large damage)

5.4 Effect of Speed and Load on Selected Monitoring Indices

Figure 5.8 is a schematic of the test bed used for the study described in this section. The test bed consists of a ball bearing unit, a hydraulic cylinder, driving components (not shown in the schematic), accelerometer, and load cell. The ball bearing used in this research is NTN UC205, which is damaged by applying an excessive radial force of 8 kN for 825 minutes. The propagated defect is located on the outer race with a size of 0.925 mm^2. The radial load is applied by a hydraulic cylinder. The vibration of the bearing is measured by a Dytran 3035 AG accelerometer with a sensitivity of 100 mV/g. The shaft is supported by two taper roller bearings, SKF 30204 J2/Q. The system is driven by a 3 hp induction motor, equipped with an AC Tech M1230 SB speed controller, in the speed range of 0-1800 rpm. The applied radial force is measured by a LC411-5K OMEGADYNE load cell. To examine the effect of load and speed on the monitoring indices, the vibration data is collected at six different speeds: 300, 600, 900, 1200, 1500, and 1800 rpm under load conditions of 0.08, 2, 4, and 8 kN. After 20 minutes of warming period, the normal bearing data is recorded. The collection of damage data begins when all the three diagnostic indices: NIE, CD, and MACW register significant change in our case from 0.6 to 3.1, 8.1 to 5.0, and 0.8 to 3.7, respectively.

Figure 5.9 shows the measured NIE, of the normal and the damaged bearings under different speed and load conditions. The experimental results reveal that when the shaft speed is higher than 800 rpm, the NIE of the healthy bearing is relatively constant in the range of 0.2 to1.5, and for the damaged bearing, the NIE is between 2.5 and 4. What is more important in Figure 5.9 is that the NIE is independent of the speed and load in the speed range, where the chaotic vibration dominates (for the test bearing, the chaotic behavior occurs when the speed is higher than 800 rpm). This is a critical characteristic for a bearing fault indicator that can be utilized in the diagnosis or prognosis of variable condition systems.

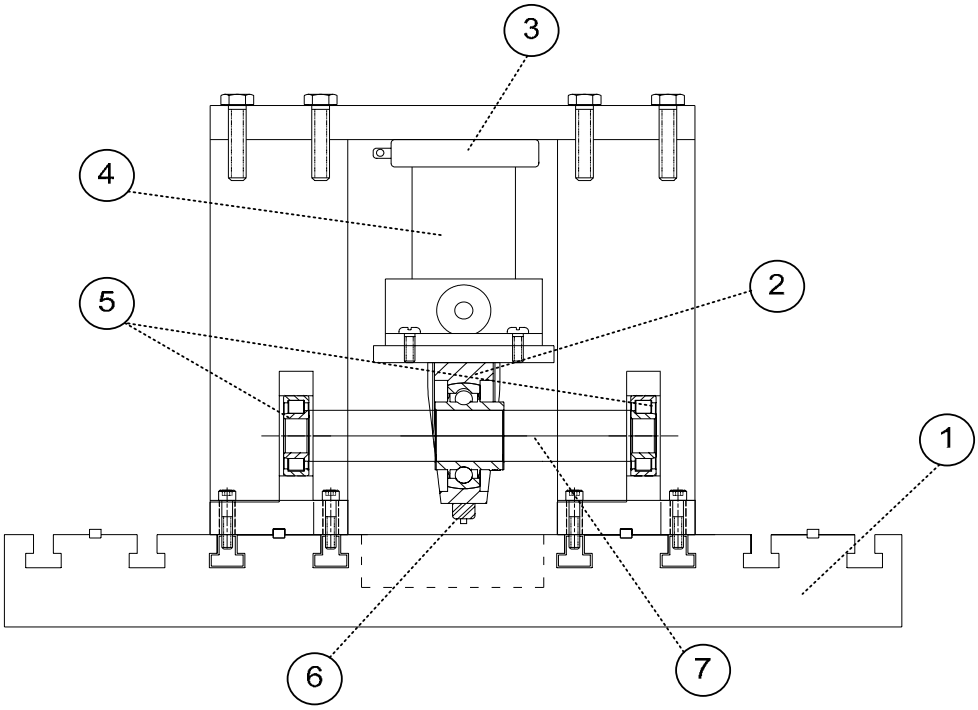

1. Base plate
2. Test bearing, NTN UC205
3. Load cell
4. Hydraulic cylinder
5. Supporting bearings, SKF 30204 J2/Q
6. Accelerometer
7. Driving shaft

Figure 5.8. Schematic of load-speed test bed

The experimental results in Figure 5.10 demonstrate that the reduction in the correlation dimension in a damaged bearing is distinguishable within a load range of 2 to 8 kN. However, the variation is not significant for lightly loaded systems (0.08 kN). The reason for this is in a lightly loaded bearing, the effect of damage on the vibration signature is more randomlike than periodic. As a result, a reduction in the correlation dimension is small. Similar to the results of NIE, the results show that the correlation dimension is effective as a fault indicator for speeds higher than 800 rpm. Within this range and for a load condition higher than 2 kN, The correlation dimension is independent of speed and load.

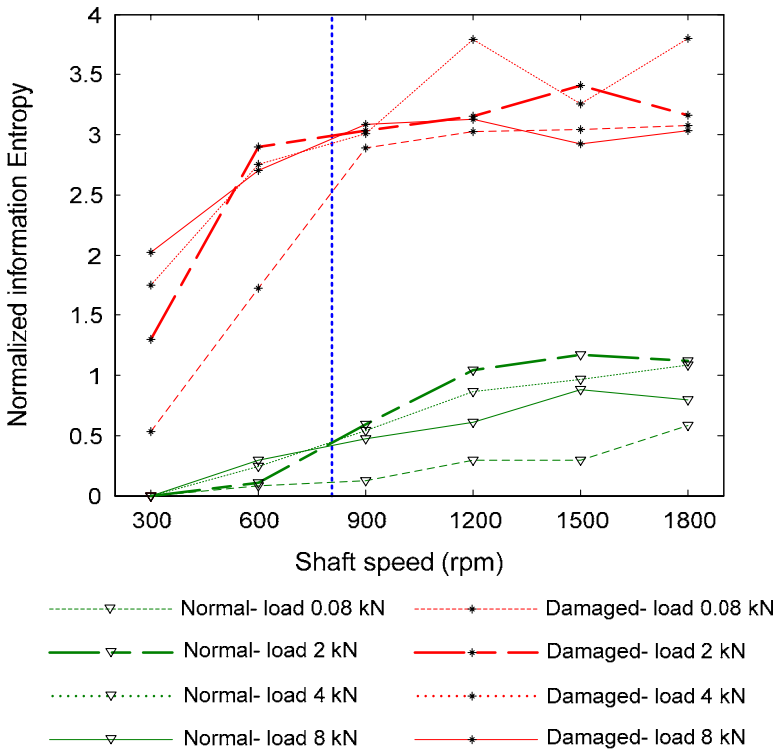

Figure 5.9. Variation of the Normalized Information Entropy (NIE) under different speed and load conditions for normal and damaged bearings

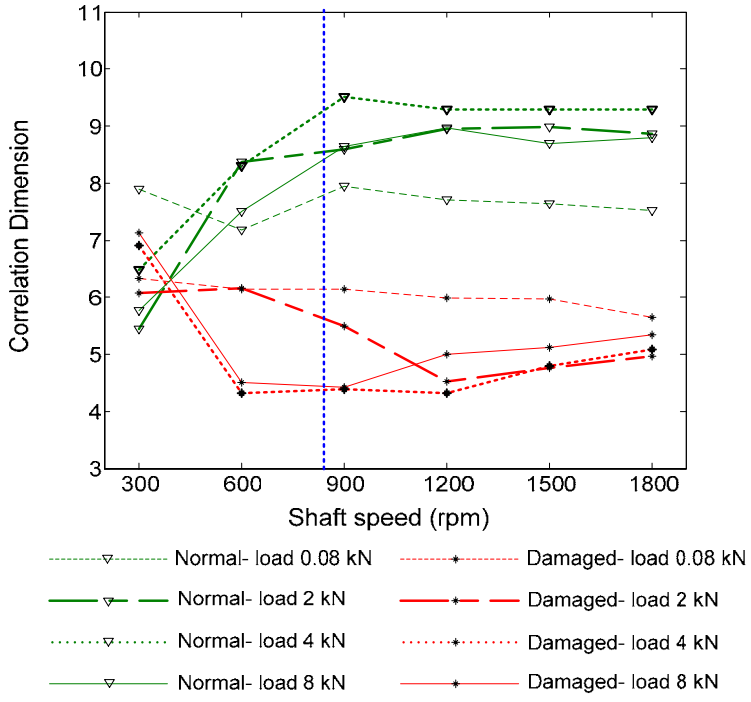

Figure 5.10. Variation of correlation dimension (CD) under different speed and load conditions for normal and damaged bearings

The MACW decomposed up to 4 levels by the Daubechies4 wavelet (db4) of the measured vibration, is plotted in Figure 5.11. The graph shows that there is a dependency on speed, yet the level of the MACW in a damaged bearing is significantly higher than that associated with a normal bearing within a wide range of rotational speeds and loads. It is worth noting that an attempt was made to lessen the speed dependency by dividing the MACW by the RMS. The attempt was, though, unsuccessful primarily because of the significant difference in the slopes of the MACW and the RMS. The distinct separation, however, between the values of the MACW, associated with normal bearings and the damaged bearings, still makes it possible to use the MACW as a damage monitoring index. This effectiveness of the MACW, as a reliable indicator, diminishes greatly at low speeds, <600rpm, and lightly loaded systems >0.08 kN.

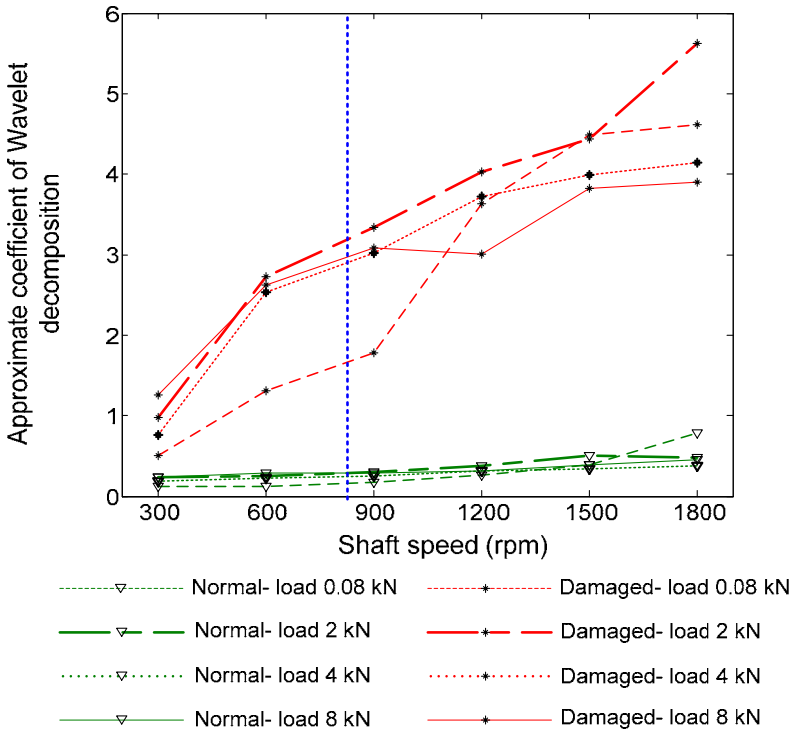

Figure 5.11. Variation of the Maximum Approximate Coefficient of Wavelet (MACW) under different speed and load conditions for normal and damaged bearings

5.5 Summary

From this comprehensive investigation, it is found that Normalized Information Entropy (NIE), Correlation Dimension (CD), and Maximum Approximated Coefficient of Wavelet (MACW) are reliable indices for bearing condition monitoring. It is also demonstrated that the variation of these indices is proportional to the damage size. In addition, it is experimentally confirmed that these indices have a lower sensitivity to the load, and speed conditions. Consequently, the indices are suitable for monitoring a system that is subject to load and speed fluctuation and variation.

Chapter 6

Neuro-Fuzzy Diagnosis System

The comprehensive study in Chapter 5 indicates that the most sensitive and robust methods for bearing fault diagnosis include: NIE, Correlation Dimension (CD), and MACW. Failure detection entails the classification of the indices into different categories. For this purpose, an intelligent processing tool is used to map the features into monitoring decisions.

The traditional methods for fault diagnosis are categorized as pattern classification, knowledge-based inference, and numerical modelling. Pattern classification and knowledge-based inference techniques are used in the industry. In these two methods, a human expert looks for particular patterns in the vibration signature that might indicate the presence of a fault in the bearing. Alternatively, statistical analysis and ANNs are utilized for the automated fault detection systems. ANNs are capable of learning the behavior of nonlinear systems. In a fuzzy inference system, a set of logical rules is extracted from an expert knowledge database, independent of the system's configuration.

ANNs are adopted for machinery fault diagnosis and condition monitoring. One of the first applications of ANNs for bearing fault diagnosis has been proposed by Baillie and Mathew [50]. The scheme requires a collection of time series features for each class of bearing faults as inputs of an ANN. This time domain based model has the advantage that the diagnosis can be performed by using a short data length and is appropriate for slow-speed machines. However, due to computational difficulties the model is unable to process a large volume of data and consequently long time monitoring. Liu et al. [61] have developed a fuzzy expert system for bearing diagnosis. The system employs the

average of the top five amplitudes of the frequency response in a high frequency region (5-22 kHz), as a monitoring feature. Piecewise linear membership functions are used in the proposed fuzzy reasoning system. Subrahmanyam and Sujatha [54] have compared the performance of a multilayer feed-forward with supervised training with that of an Adaptive Resonance Theory (ART-2) based network with an unsupervised training algorithm. A collection of features, including Kurtosis, RMS, peak values of time and high frequency domains, and peak values of autocorrelation are chosen as monitoring indices. The test results reveal an acceptable rate of correct classification after a long training process due to the large number of inputs.

Jack et al. [52] have tested the application of a Radial Basis Function (RBF) network for diagnosis. The features of interest are extracted by an experimental apparatus under a constant load and speed for different bearing faults. The features include various statistical moments of vibration data, extracted from raw and demodulated vibration signals. Although the proposed network is unsuccessful in classifying the outer race and cage defects, the research demonstrates the advantage of using features, obtained from a demodulated signal instead of raw vibration. Samanta and Al-Balushi [51] have found that a feed-forward ANN with two hidden layers is sufficient for the separation of bearings with and without faults. The features, used as network inputs, are RMS, Kurtosis, skewness, and normalized sixth central moment of time domain data, extracted from the envelope of the signal.

Wang et al. [111] have introduced three reference functions, based on wavelet transform, beta Kurtosis, and phase modulation for gear system monitoring. The developed neuro-fuzzy classifier provides a robust diagnosis for gear systems. According to the non-stationary characteristics of bearing fault vibration, a diagnosis method based on the Empirical Mode Decomposition (EMD) energy entropy, has been reported by Yang et al. [112]. An ANN, with the input features extracted from different frequency bands of the EMD, can accurately identify the localized fault pattern.

According to our knowledge, the application of neural networks for the fault diagnosis of variable speed systems has not been tested yet. In this chapter, an intelligent neural based algorithm is employed to integrate the strength of the proposed monitoring indices to provide a more reliable assessment of bearing condition in speed varying systems. To select the best decision-making algorithm, the diagnosis performance of three well-known neural networks, Multi Layer Perceptron (MLP), RBF, and Adaptive Neuro-Fuzzy Inference System (ANFIS) are compared to verify the efficiency of each scheme.

6.1 Decision-making Schemes

Figure 6.1 illustrates the decision-making process. All the steps shown in the figure are off line. The features employed here are extracted from a pre-processed bearing vibration signal. The resultant features serve as the input to the diagnostic algorithm. The output of the neural-system identifies the bearing health condition and the level of possible damage. Here, the performance of three types of ANNs is studied as the decision-making algorithm. A brief description of each network follows.

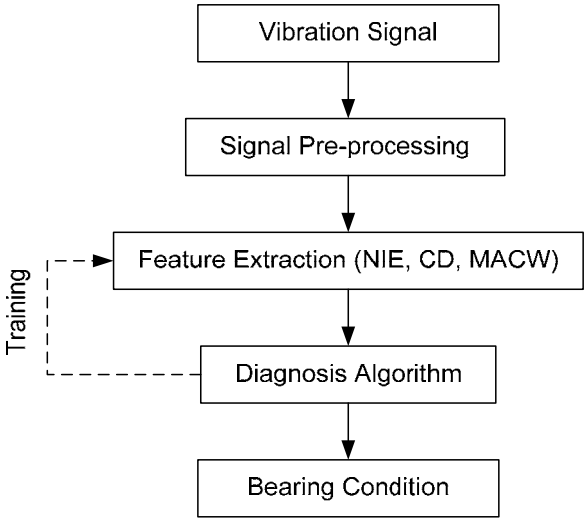

Figure 6.1. Bearing condition decision-making process

6.1.1 Multi Layer Perceptron (MLP)

MLP is one of the most successful feed-forward neural networks for diagnosis. The challenges for constructing a MLP network are the determination of sufficient number of hidden layers, neurons within each layer, learning rate, and activation function. Although a formal methodology to express the number of hidden layers and neurons does not exist yet, the larger the number of layers and neurons, the better the classification. However, more neurons and layers result in a longer training period and convergence problem. By experimenting, the best results of a classification by MLP are obtained from a structure that includes three hidden layers, where each consists of 10 neurons. For the nodes in the hidden layers, a hyperbolic tangent sigmoid is chosen as the transfer function, whereas the linear function is assigned to the output node. The input vector consists of three monitoring indices: NIE, CD, and MACW, computed for each batch of bearing vibration data that are measured by an accelerometer. The numerical value of the network's output corresponds to the level of the bearing health. A gradient descent algorithm with a learning rate of 0.25 is applied to train this network.

6.1.2 Radial Basis Function Network (RBF)

Radial Basis Function (RBF) networks belong to the class of feed-forward neural networks. Traditionally, they have been used for mapping nonlinear functions and are efficient for data classification. The constructed network consists of an input layer, including monitoring indices: a single hidden layer; and an output layer that corresponds to the condition of the bearing.

The network structure utilizes a nonlinear transfer function in its hidden layer, but uses linear transformation between the hidden and the output layer. Unlike other types of feed-forward networks, the connection weights between the input and the hidden layer are all equal to unity. The Gaussian kernel function is selected as the activation function of the hidden layer neurons. To train the RBF network a combination of an unsupervised

clustering and a supervised weight updating is required. In the first step, the self organizing map is employed to extract the centre and width of the radial basis function. Then, a supervised least mean square algorithm is used to update the connection weights between the hidden layer and the output layer. An important feature of RBF networks is their fast training compared with that of back-propagation networks.

6.1.3 Adaptive Neuro-Fuzzy Inference System (ANFIS)

Learning the behavior of a nonlinear numerical system is the most important feature of neural networks. Fuzzy-inference systems consist of rules for the system's behavior. The combination of both systems, neuro-fuzzy systems, provides fuzzy inference with a learning capability.

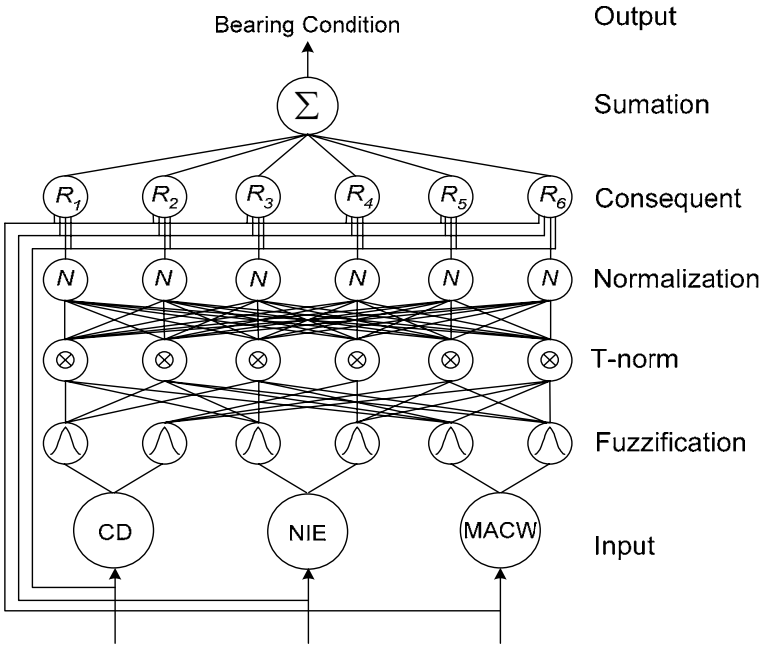

Figure 6.2. Network structure of an ANFIS employed for bearing diagnosis

ANFIS utilized here is a five-layer neuro-fuzzy system which maps the inputs, through membership functions, to the outputs. The initial membership functions and rules for a fuzzy inference system are designed by either human expertise or automatically. ANFIS can then refine the fuzzy if-then rules and the membership functions to describe the

input-output behavior of a complex system. Figure 6.2 reflects the five-layer ANFIS structure, used as the prognosis tool in this thesis.

The input data are fuzzified in the first layer, where each neuron stores the parameter of the membership function (a, b, c), defined by

$$\mu_{A_i}(x_i) = \frac{1}{1+\left(\left(\frac{x_i - c}{a}\right)^2\right)^b} \tag{6.1}$$

In the T-norm layer, the inputs of each neuron are the degrees of the membership functions which are multiplied through a T-norm operator to determine the degree of rule satisfaction. The output of this layer is normalized in the normalization layer. The neurons of the subsequent layer are then connected to the inputs and one neuron of the previous layer. Each neuron computes the consequence of the rule, and the output of the network is the summation of all the consequence layer outputs [113].

6.2 Results and Discussion

To compare the diagnostic efficiency of the selected networks, a series of tests is conducted by using the apparatus in Figure 3.8. The same bearing conditions, described in section 5.1, including a normal bearing, small and large inner race, outer race, and roller defects, are tested under different rotational speeds of 900, 1200, 1500, and 1800 rpm. A total of 560 sets of data are collected to examine the diagnostic reliability. The test conditions and the number of each data set are listed in Table 6.1.

Each set of data is represented by a three element array, called a monitoring vector, and consists of three monitoring indices: NIE, CD, and MACW. The required signal processing method and calculation procedure of each monitoring index is detailed in section 5.2. From the 560 data sets, 120 identical monitoring vectors are used for the training, and the remaining 440 vectors are utilized for testing. To quantify the bearing

health level, quantified values are assigned for different health conditions: fault free = 1, small damage = 2, and large damage = 3 with a limiting range of ±0.5 for each level.

Table 6.1. Bearing condition monitoring data sets

Bearing Condition		Speed (RPM)	Data sets
Normal		900 1200 1500 1800	40 40 40 40
Inner race	Small damage	900 1200 1500 1800	15 15 15 15
	Large damage	900 1200 1500 1800	15 15 15 15
Outer race	Small damage	900 1200 1500 1800	15 15 15 15
	Large damage	900 1200 1500 1800	15 15 15 15
Rolling element	Small damage	900 1200 1500 1800	15 15 15 15
	Large damage	900 1200 1500 1800	15 15 15 15

The MLP network is trained by a gradient descent algorithm after 200 epochs for 3.4 seconds. Figure 6.3 shows the classification results of the MLP network.

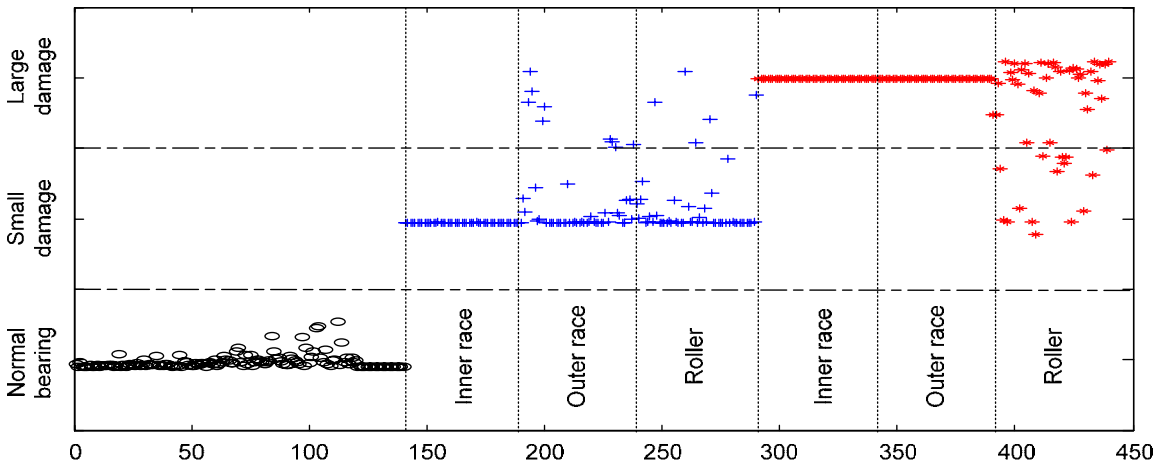

Figure 6.3. Diagnosis results of the MLP network: (o: fault-free; +: small damage; *: Large damage)

Figure 6.3, illustrates that MLP has successfully detects all the fault-free and small damaged inner race conditions; however, the accuracy of indicating the level of small damage in the outer race is inadequate. Although the results of the outer and inner race large damage are significantly consistent, due to the low sensitivity of the monitoring indices to the level of roller damage, categorizing large and small damage is unsuccessful.

Since the connection weights between the input and the hidden layer in RBF are all equal to unity, the normalization of the input data plays an important role in the performance of the mapping. Therefore, the elements of the monitoring vectors for both the training data and testing batch are normalized. The network is then trained by a hybrid method that consists of a supervised and an unsupervised algorithm after 200 epochs for 0.9 seconds. Figure 6.4 presents the classification results of the RBF network. It is evident that the RBF network not only fails to categorize different levels of faults, but also, is incapable of classifying the fault-free conditions from the damaged data sets. The low quality of the classification in RBF can be due to the equal connection weights between the input layer and the neurons of the hidden layer. The equal weights in RBF structure, affect the unique behavior of each fault indicator within the network.

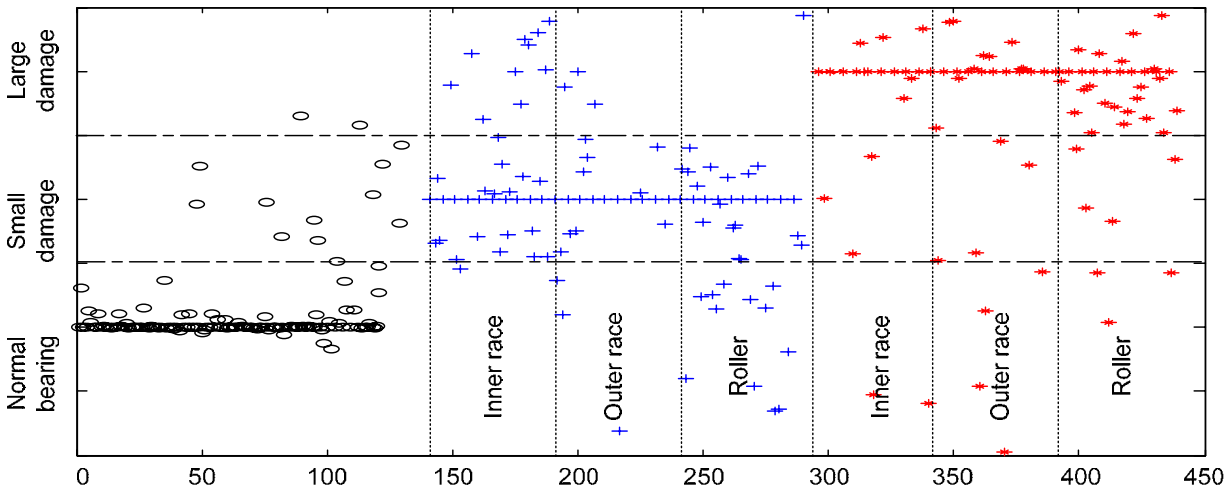

Figure 6.4. Diagnosis results of the RBF network (o: fault-free; +: small damage; *: Large damage)

The proposed ANFIS for the bearing fault classification problem is constructed as a Sugeno-type inference system. Similar to the other networks, to train the model, 120 sets of training vectors are needed. The training process converges after only 20 epochs for less than 1.2 seconds. Figure 6.5 exhibits the classification results by a trained ANFIS network for 440 series of data for different fault categories.

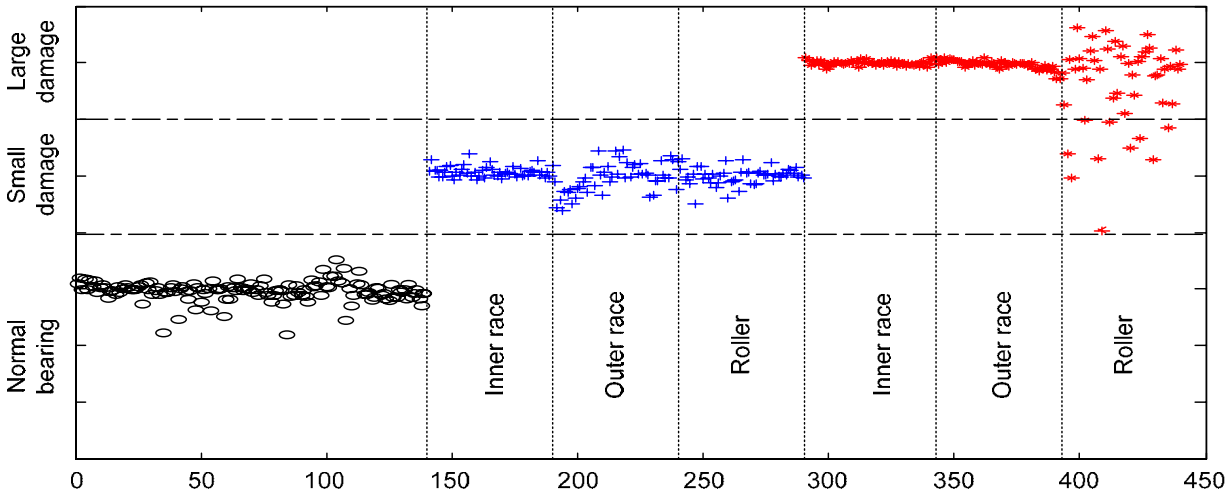

Figure 6.5. Diagnosis results of the ANFIS network. (o: fault-free;, +: small damage; *: Large damage)

The results demonstrate the high rate of correct diagnosis by the ANFIS network. The noticeable classification of each fault level except the large roller damage is significant in ANFIS. The **incorrect** diagnosis decisions by the proposed schemes are listed in Table

6.2. In this table a “false alarm” is employed for any misclassification between the normal bearings and damaged ones, and “false grading” is assigned to any incorrect indication of the damage level, small and large damage.

Table 6.2. Diagnosis results of proposed neural networks

Network	False alarm	False grading
MLP	0	29
RBF	36	25
ANFIS	0	10

6.3 Summary

To enhance the bearing diagnostic efficiency, a set of different fault indicators extracted from the vibration data, are selected. The features include: NIE, CD, and MACW. Neural networks with nonlinear curve fitting and learning capability are potential candidates for the decision making-algorithm in a diagnostic scheme. In this chapter, the diagnostic efficiency of three neural networks, MLP, RBF, and ANFIS are compared. The experimental results indicate a high rate of correct classifications and damage quantification, in excess of 95%, by ANFIS.

Chapter 7

Bearing Condition Prognosis

In the previous chapter, it was shown that the integration of the proposed monitoring indices for a decision-making system increases the reliability of the diagnosis of faulty bearings. The same approach may be feasible for a prognostic system, a prognostic system capable of predicting the fault propagation trend, and providing an alarm before a fault reaches a critical level. The experimental results in section 6.2 demonstrate that a combination of a neuro-fuzzy algorithm with the monitoring indices, proposed in Chapter 5 can provide superb diagnosis results for variable speed systems. In addition, Karray and Siva have shown [113] that of all the flexible forecasting models, Recurrent Neural Networks (RNNs) and ANFIS are the most promising methods for time series prediction. In this chapter, the prognostic performance of RNNs and ANFIS, are compared. Finally, a prognostic architecture that consists of three components: monitoring indices, a forecasting algorithm, and decision-making rules is proposed and its performance is evaluated.

The bearing prognostic methods reported so far are classified as model based life prediction, and intelligent systems. The first category focuses on a model to predict the fatigue life of a bearing, and various models have been proposed in the literature. The Weibull model, based on the dispersion of fatigue life [67]; the well known Lundberg-Palmgren model, based on surface-originated fatigue [68]; and its extended version by Tallian [69], and the discrete-stressed approach by Ioannides and Harris [70], are among the most noted models for bearing life estimation. Recently, more complex prognostic models, based on the bearing stiffness [71], inverse power law [72], and Hertzian contact theory [73], have been proposed.

The second category deals with bearing prognosis based on statistical and intelligent systems. The primary challenge in this category is selecting a suitable monitoring index or indices, and an efficient prediction scheme. Time and frequency indicators such as RMS, Kurtosis, crest factor, and spectral amplitudes have been widely employed for bearing diagnostics. However, these indices are either strongly dependent on speed and load, or have a low sensitivity to a bearing's early stage faults.

Little research has been reported on the application of neural networks for bearing prognosis. Malhi and Gao [74] have presented a multi-step prediction scheme, based on RNNs. In this scheme, the monitoring feature is the wavelet pre-filtered normalized peak value. Their experimental work on a bearing with an initial damage under particular test conditions shows an advantage of the modified RNN training method over the conventional incremental method. Gebraeel et al. [75] have introduced a feed-forward back propagation network for the prognosis of thrust bearings. In their experiments, failure was induced by means of a constant excessive load. The monitoring index in the suggested prognosis scheme is the RMS of the vibration data. The authors reported more than an 80% correct prediction of actual failure time. Wang et al. [114] have demonstrated that when a Neuro-Fuzzy (NF) system is properly trained, it performs better than a RNN in both estimation and training. Consequently, the prognosis results of a NF are found to be very reliable and robust for a gear system. However, NF has not yet been tested on bearings. Haung et al. [76] have proposed a prognosis structure that depends on a fault indicator derived from a self-organizing map that is trained by time and frequency features. The authors have utilized a back propagation neural network for the prediction of the bearing's residual life. The results of the developed model show less than a 10% error which is superior compared to that of the L_{10} traditional formula.

So far, only a small amount of research has been conducted on bearing prognosis under variable speed and load conditions which is the subject of the investigation in this thesis. In this chapter, ANFIS is utilized for forecasting; and it is shown that it can efficiently capture the dynamic behavior of fault propagation in a run-to-damage experiment. The

method's effectiveness is demonstrated for bearing prognosis under different loads, speeds, and bore diameters.

7.1 Experimental Setup

The experimental setup shown in Figure 7.1 is used to perform accelerated life tests on the bearings. The test bed consists of a ball bearing unit, a hydraulic cylinder, driving components, accelerometer, and a data acquisition system. The ball bearings for this research are NTN UC205, and Koyo UCP206, both mounted in the pillow block cast iron housing. The bearings are properly lubricated by a multi purpose grease No. 630-2. The radial load is applied by an ENERPAC hydraulic single-acting cylinder RCH 202. To accelerate the defect propagation process, an excessive radial load of up to 15 kN is applied on the bearing. The theoretical bearings fatigue life for NTN UC205, under the test condition is rated at 31, and 24 hours for Koyo UCP206 at a speed of 1500 rpm. The vibration of the bearing is measured by a Dytran 3035 AG accelerometer. The shaft is supported by two taper roller bearings, SKF 30204 J2/Q, each with a dynamic load rate higher than that of the tested bearing. The system is driven by a 3 hp induction motor, equipped with an AC Tech M1230 SB speed controller in a speed range of 0-1800 rpm. A DACTRON dynamic signal analyzer, Photon 100, equipped with a low-pass anti-aliasing filter, is utilized for the data acquisition.

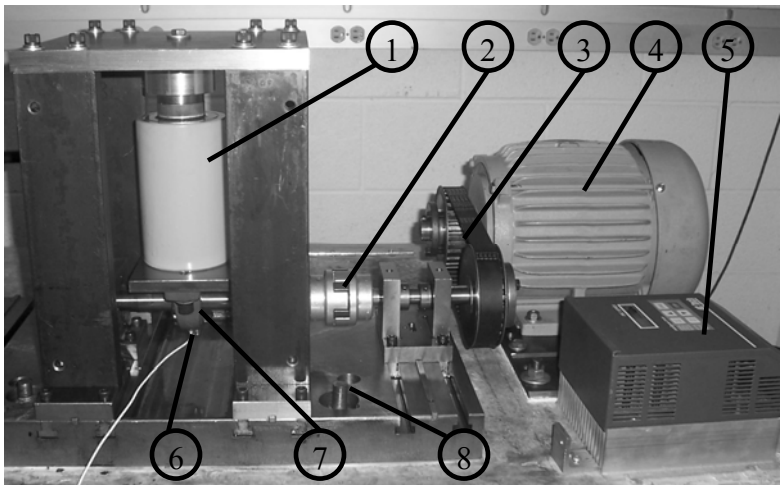

1. Hydraulic Cylinder
2. Coupling
3. Belt and pulley
4. Motor
5. Speed controller
6. Accelerometer
7. Test bearing
8. Base plate

Figure 7.1. Experimental setup

7.2 Monitoring indices

The sensitivity and robustness of the fault indicators play key roles in an automated prognostic system. Currently, there are many vibration-based monitoring techniques available for the detection of bearing faults. Usually, more than one monitoring index is adopted to increase the robustness of the prognostic system. In this work, three indices are utilized: NIE, CD, and MACW whose sensitivities and robustness were demonstrated in detail in section 5.4. These monitoring indices, extracted from a measured vibration signal, are employed as the input to the forecasting algorithm. NIE and CD proved to be insensitive to speed and load. The third indicator showed some dependency on speed, yet there was a marked difference in the values of the normal and damaged bearing.

7.3 Neural Network Predictors

A reliable prognostic system should forecast the fault propagation, and generate an alarm before the fault reaches a critical level. To prognose the health condition of a

bearing, a reasonable approach is to use the current and previous monitoring indices values to forecast the future state. Of the flexible forecasting approaches, neural networks have the most potential due to their capability of learning the behavior of nonlinear systems. In this section, the efficiency of bearing prognosis is evaluated by using two types of common predictive networks: RNN and ANFIS. These two networks are among the most promising intelligent systems for the prediction of random and chaotic time series [113]. They are briefly discussed below.

7.3.1 Recurrent Neural Networks (RNN)

In this type of feed-forward network, the current and previous states of the system are used for future state prediction. Feedback connections still exist within the main body of the network, as depicted in Figure 7.2. RNNs contain two key advantages for the prediction of dynamic systems. First, the network possesses an internal memory in its structure. Secondly, the network's output depends on the previous state of the system. These properties of RNNs enable them to exhibit internal dynamic behavior, rendering them more suitable for the prediction of complex dynamic systems. Since the forecasting performance of RNNs with different architectures is mostly similar, in this work, an Elman structure is utilized for the prognosis. The proposed network has four layers and three input nodes. The input vector is in the form of, $x_t = \{x_{t-2n}\ x_{t-n}\ x_t\}$, where x is the monitoring index for n-step-ahead prediction. In this work the idea is to estimate the next state of the bearing condition through a one-step-ahead prediction of the monitoring index, x_{t+1}. The nodes in the input and context layers transmit only input values to the hidden layers. The hyperbolic tangent sigmoid transfer function is chosen for the hidden layer neurons, whereas a linear function is assigned to the output node. A quasi Newton algorithm[113] is utilized for training RNN with a gradient learning rate of 0.2.

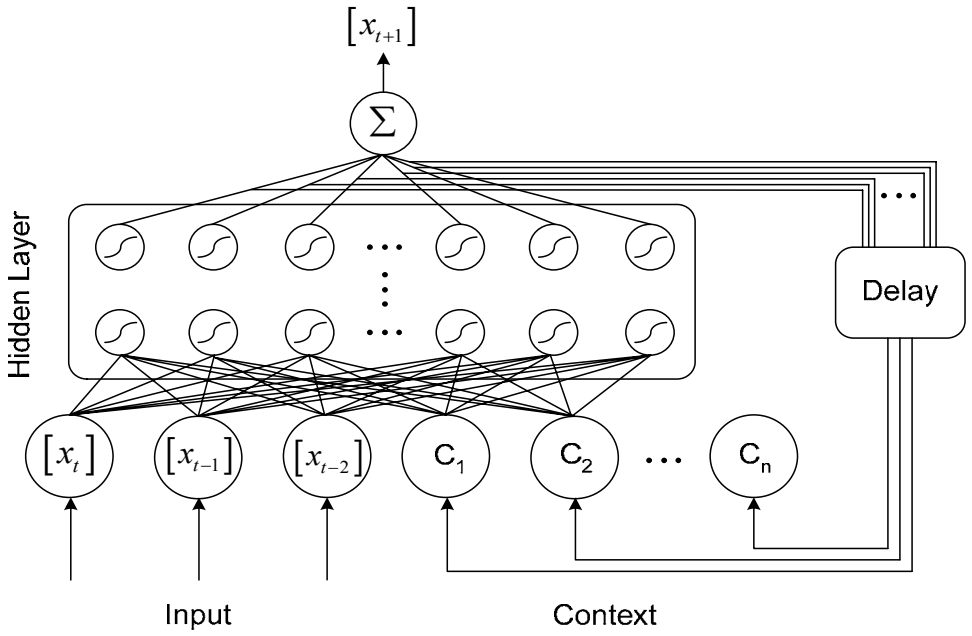

Figure 7.2. Recurrent Neural Network (RNN) structure

7.3.2 Adaptive Neuro-Fuzzy Inference System (ANFIS)

ANFIS is a five-layer neuro-fuzzy system. The initial membership functions and rules for a fuzzy inference system are chosen arbitrarily. ANFIS then refines the fuzzy if–then rules and the membership functions through a training process. To make the ANFIS comparable with the aforementioned RNN, the same three input parameters are used for the one-step-ahead prediction.

7.4 Bearing Fault State Prognosis

To test the newly developed prognosis scheme, five accelerated life tests under different test conditions are conducted. In each test, a new set of bearings is mounted on the shaft and run for 20 minutes without an external load. After the warm-up period, the load is applied on the bearing and the acceleration data is collected over 10 seconds at the sampling frequency of 6000 Hz. The data is collected every five minutes. The tests are continued without interruption to the point of termination, when one or more of the monitoring indices increase abruptly. In addition to the three indices, NIE, CD, and

MACW, the Kurtosis and HFRT amplitude are also monitored. After each test, the bearing is removed, and the outer race cut for a visual inspection of the damage in the different components. The visual inspection is carried out under a microscope, where the projected area of damage can also be estimated. Figure 7.3 exhibits the propagated wear on the outer race during Test 1 and Test 3.

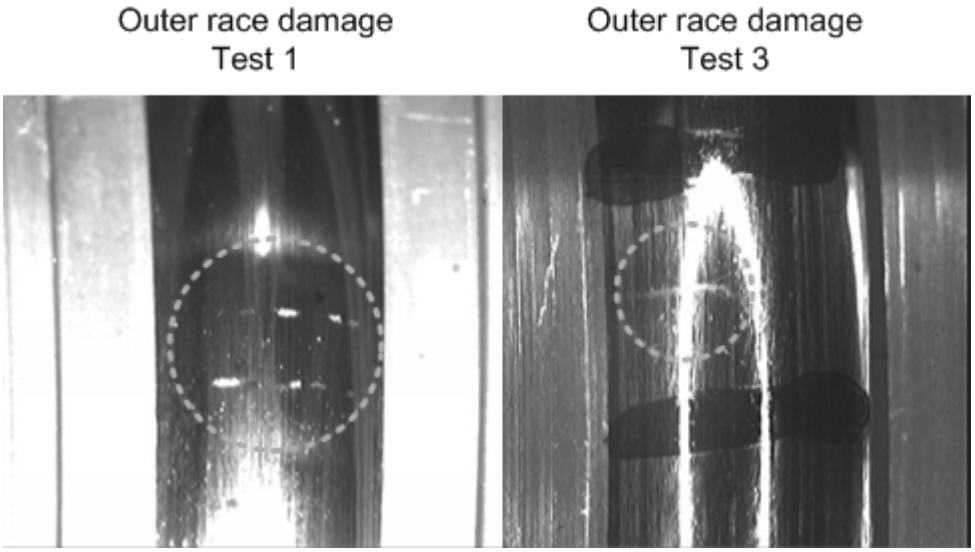

Figure 7.3. Outer race damage Test 1 and Test 3

Table 7.1 lists the running time of each test, type and size of damage(s), and the indicator(s) that lead to terminating the test. According to [115], the industry standard for a critically damaged area is 6.25 mm^2 (0.01 in^2). The recorded damage areas in Table 1 are one order of magnitude smaller than the critical value. In other words, the proposed scheme is sensitive enough to show the incipient faults clearly. The prediction of the time period for a small fault to develop to the critical standard size (remaining life) depends on the type of application and working environment, a study which is beyond the scope of this research.

Table 7.1. Test descriptions and conditions

	Type Bearing	Time span (min)	Speed (rpm)	Load (kN)	Defect location	Defect size (mm^2)	Alarm indicator	Change in indicator	
								From	To
Test 1	NTN UC205	630	1500	8	outer race	0.614	NIE CD MACW	0.6 8.2 0.7	2.3 5.3 2.4
Test 2	NTN UC205	130	1500	8	-	-	Kurtosis	3.1	14.6
Test 3	NTN UC205	315	1500	12	outer race ball ball	0.468 0.535 0.578	NIE CD MACW	0.7 8.1 0.6	2.4 5.2 2.8
Test 4	NTN UC205	825	1000	8	outer race	0.925	NIE CD MACW	0.6 8.1 0.8	3.1 5.0 3.7
Test 5	Koyo UCP206	350	1500	15	outer race outer race	0.791 0.296	NIE CD MACW	0.7 9.2 0.8	2.2 5.9 2.5

In the first test the bearing is damaged under the load of 8 kN at the speed of 1500 rpm for 630 minutes. The three indicators: NIE, CD, and MACW exhibit a very large variation, 0.6 to 2.3, 8.2 to 5.3, and 0.7 to 2.4, respectively. In the meantime, the kurtosis changes only from 3.0 to 2.7. In the second test with similar conditions to those of test 1, it is the Kurtosis that increases drastically from the normal value of 3 to 14.6. NIE, CD, and MACW show negligible change. The investigation of the bearing components does not demonstrate any damage in the bearing elements which casts doubt on the robustness of the Kurtosis while lends credence to the proposed indices. In tests 3 and 4 the same type of bearing is tested under different speeds and load conditions. In these tests, it is the proposed indices that signal the occurrence of damage. In test 3, the damage is found on the outer race, as well as on two balls. In test 5, a larger size bearing (bore diameter 30 mm) of a brand different from those used in tests 1-4 is tested under a load of 15 kN at a speed of 1500 rpm. Again it is NIE, CD, and MACW that signal the occurrence of damage. In this case, the damage is found on the outer race at two locations.

An investigation is conducted to assess the prognosis performance of RNN and ANFIS when each of the monitoring indices is employed. Table 7.2 lists the different setups in the investigation; the first three lines, schemes 1, 2, and 3 are associated with RNN whereas the last, schemes 4, 5, and 6 are associated with ANFIS. In schemes 1 and 4, NIE is used as the monitoring index, in 2 and 5 it is CD, and in 3 and 6, it is MACW. The forecasting relies on finding the index x_{t+1} at time $t+1$ by using current x_t and previous x_{t-1} and x_{t-2}. In this way, the forecasting is limited to one-step-ahead. In each step, the forecasted value is compared with the actual measured value of the index; the difference between them is the "error in forecasting". The overall error is computed by summing the square of the error at all steps, taking the square root of that, and dividing it by the average of the measured index. The result is multiplied by 100 to attain the forecasting error percentage. It should also be realized that the intention of the forecasting is to use the forecasted value in making the prognosis of the bearing health condition, healthy or damaged. Accordingly, another measure of the performance of the used algorithm, RNN or ANFIS, is established; that is, FCP, the False Condition Prediction. FCP is calculated by counting all the incidents in which the forecasted values give false indications, missed, or false alarms, when they are compared to the actual measured ones, and dividing by the number of all measured data in the experiment.

The investigation is conducted for the five tests listed in Table 1. Test 1 is used for training the networks; Tests 2-5 are applied to assess their prognosis performance. In each experiment, the "normal value" of the monitoring index is taken as the average of the measured values over the first 30 minutes. Based on the behavior of the indices observed in Figures 5.9,5.10, and 5.11, the damage threshold for each monitoring index is selected at: a) a value three times greater than the normal value for NIE; b) a value smaller than 6 for CD; c) a value three times greater than the normal value for MACW.

Table 7.2. Prognostic schemes

Scheme No.	Network	Neuron/Layer	Input	Monitoring Index
1	RNN	10/4	$[X]=\{x_t, x_{t-1}, x_{t-2}\}$	x = NIE
2	RNN	10/4	$[X]=\{x_t, x_{t-1}, x_{t-2}\}$	x = CD
3	RNN	10/4	$[X]=\{x_t, x_{t-1}, x_{t-2}\}$	x = MACW
4	ANFIS	6/5	$[X]=\{x_t, x_{t-1}, x_{t-2}\}$	x = NIE
5	ANFIS	6/5	$[X]=\{x_t, x_{t-1}, x_{t-2}\}$	x = CD
6	ANFIS	6/5	$[X]=\{x_t, x_{t-1}, x_{t-2}\}$	x = MACW

The prognosis results with RNN, schemes 1, 2, and 3, for tests 3, 4, and 5 are plotted in Figure 7.4. The results indicate that RNN is relatively successful in accurately forecasting the behavior of similar bearings, in tests 3 and 4, while using speed independent inputs, schemes1 and 2. The prognosis of the RNN, however, with the MACW, scheme 3, at the lower speed in test 4, is quite unreliable due to the speed dependency of this monitoring index.

Figure 7.5 presents the results of the prognosis with ANFIS, schemes 4, 5, and 6. Apparently, the forecasting results of the ANFIS structure are more accurate for all three schemes. The proposed prognostic system appears to be successful in following the behavior of the fault propagation very closely. The trained ANFIS can effectively prognose the future state of the bearing, independent of the testing conditions. Furthermore, the proposed scheme is even capable of predicting the condition of a bearing with a larger bore diameter (Koyo UCP206), while it is trained with the data acquired from a smaller size bearing (NTN UC205).

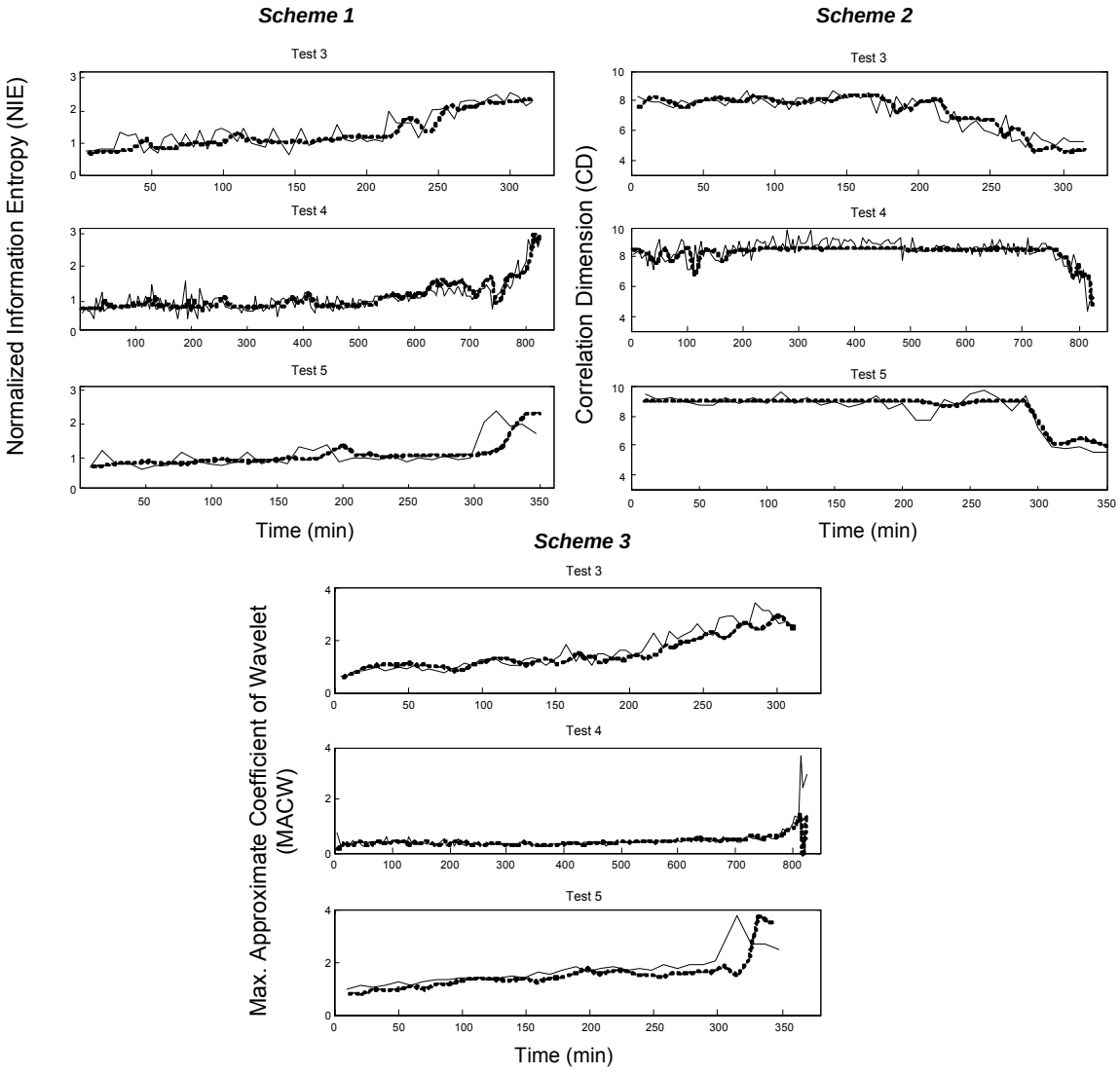

Figure 7.4. Prediction results of schemes 1, 2, and 3: solid: measured data; dotted: network prediction

Table 7.3 summarizes the performance efficiency of each scheme for a total of 305 data sets, collected under different test conditions. The results verify the accuracy of ANFIS for the three schemes, when compared with those of the RNN. The computation platform for the data processing is a Pentium (R) 3.20 GHz, 1GB RAM. Moreover, the ANFIS network converges faster in the training process than RNN. By using a 3.2 GHz PC,

ANFIS converges in 1.5, 4.2, and 3.3 seconds for schemes 4, 5, and 6, respectively. This is compared with the convergence times for RNN of 18.9, 10, and 19.1 seconds for schemes 1, 2 and 3, respectively.

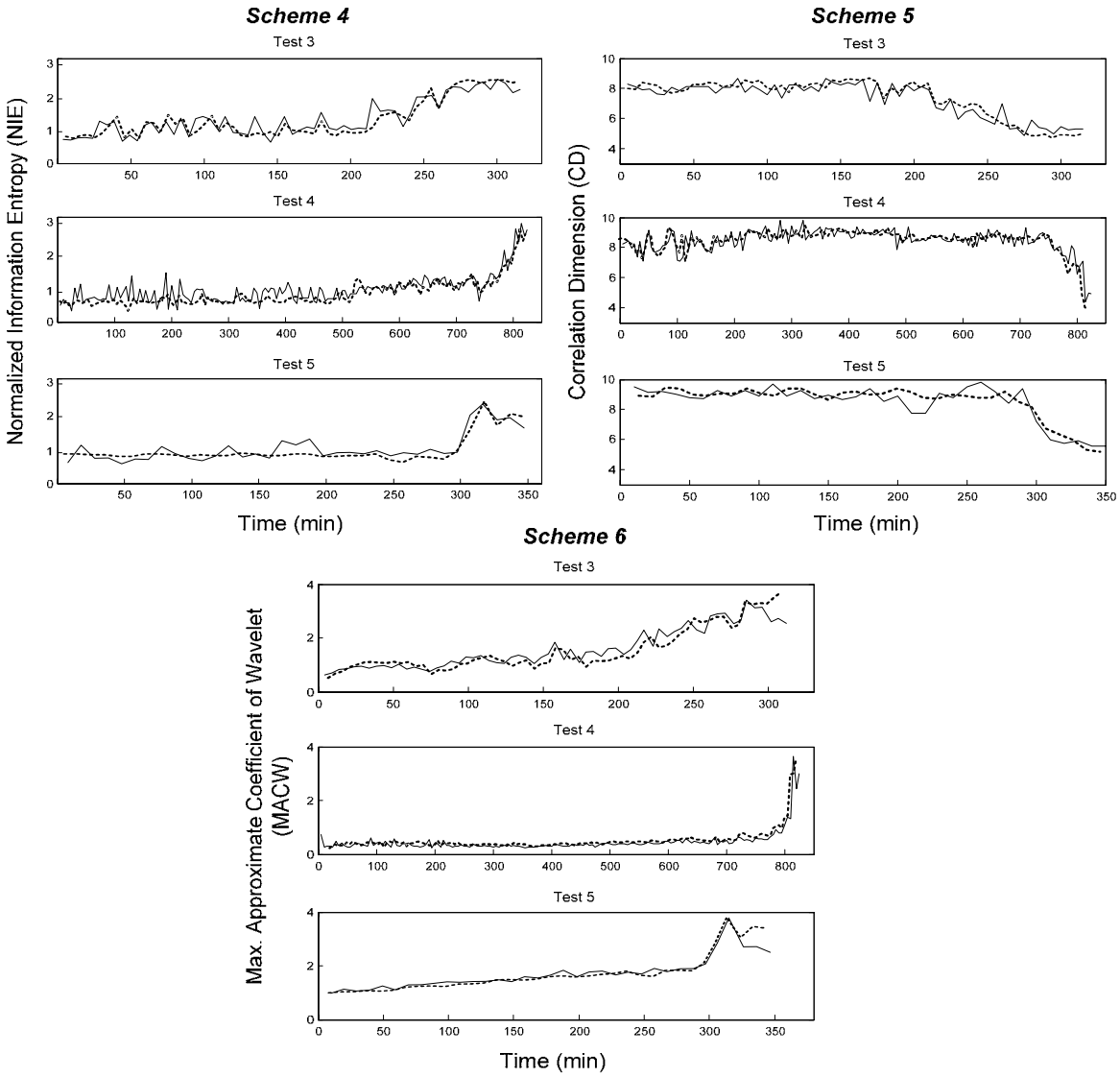

Figure 7.5. Prediction results of schemes 4, 5, and 6: solid: measured data; dotted: network prediction

Table 7.3. Comparison of prognosis performance

Comparison Criteria	Scheme 1 Test				Scheme 2 Test				Scheme 3 Test				Scheme 4 Test				Scheme 5 Test				Scheme 6 Test			
	2	3	4	5	2	3	4	5	2	3	4	5	2	3	4	5	2	3	4	5	2	3	4	5
Forecasting error %	22	24	26	35	5	8	8	10	56	67	71	47	6	11	12	12	3	5	4	4	8	9	17	12
FCP %	0	10	6	9	0	8	3	6	0	10	12	9	0	1	2	2	0	1	0	0	0	1	3	1

To increase the robustness of the novel prognostic system, the condition of the bearing can be decided based on a combination of different prognostic indices. Since the results demonstrate a better prognosis performance by using the ANFIS, it is selected for estimating the NIE, CD, and MACW, separately, and then a logic system using following rules is applied

Rule1: **IF** (NIE>T_N) **AND** (CD<T_C) **AND** (MACW>T_M) **THEN** "*Damage*"

Rule2: **IF** (NIE>T_N) **AND {**(CD>T_C) **OR** (MACW<T_M)**} THEN** "*Warning*"

Rule3: **IF** (CD<T_C) **AND {**(NIE<T_N) **OR** (MACW<T_M)**} THEN** "*Warning*"

Rule4: **IF** (MACW>T_M) **AND {**(NIE<T_N) **OR** (CD>T_C)**} THEN** "*Warning*"

Rule5: **IF** (NIE<T_N) **AND** (CD>T_C) **AND** (MACW<T_M) **THEN** "*Normal*"

Here, T_N, T_C, and T_M are the threshold values for the NIE, CD, and MACW monitoring indices. For the current test results, and based on the previously described criteria, the following threshold values are assigned: $T_N = 2.1$, $T_C = 6$ and $T_M = 2.4$.

The preceding inference system generates the *Damage* alarm when all the monitoring indices confirm damage and *Normal* when all the indices verify a healthy condition for a bearing. When any index exceeds the related threshold, the system produces a *Warning* alarm. Table 7.4 summarizes the prognostic performance of the proposed ANFIS-based predictor, when is applied for tests 2 to5 for a total of 305 prediction cases.

Table 7.4. Overall prognostic efficiency

Test No.	Number of Cases	Missed Alarm	False Alarm	Overall Efficiency
2	22	0	0	100 %
3	56	0	1	98.4 %
4	161	1	0	99.3 %
5	66	0	0	100 %

The results indicate a significantly enhanced performance, compared with that of a single indicator. Furthermore, the *Warning* alarms only appear a few steps before the damage is actually detected. The correct timing of the warning alarm is another indication of the sensitivity and intelligence of the proposed system.

7.5 Summary

The performance of two types of viable neural networks, RNN and ANFIS, are evaluated for forecasting the next state of the monitoring indicators. It is explained that once an ANFIS system is trained with the run-to-damage vibration data of a bearing, the network can capture the damage propagation behavior accurately. Such a trained network is utilized successfully to predict future states of the same series of the bearings under different speed and load conditions. The reliability of the ANFIS system is reinforced by a logical combination of the three proposed monitoring indices. The developed prognostic structure is used to evaluate the future condition of the tested bearings in 305 cases with a success rate higher than 98 percent.

Chapter 8

Conclusions

Traditionally, the monitoring of the condition of rolling element bearings has been focused on vibration measurement methods. However, very few studies have been carried out on the effect of the damage on the nature of the resulting vibration.

In this research, the behavior of a fault-free rolling element bearing is investigated. In the analyzed model, the contacts between the rolling elements and races are considered as Hertzian elastic contacts, assumed to be nonlinear springs. It is proven that the number of equilibrium points of a bearing's motion depends on the internal clearance. Bearings with a small clearance exhibit periodic motion with a unique equilibrium point. For larger clearances three equilibrium points exist at each time frame which divides the phase space into one unstable region and two stable regions. For high cage speeds (>1000 rpm), the inner ring jumps from one of the stable regions to the other, exhibiting chaotic behavior. Several routes that lead from the periodic regime to chaos, including, period doubling, Hopf bifurcation, and intermittency are explored.

The experimental results and numerical simulations confirm that the ball and cylindrical roller bearings, with a normal class of clearance, exhibit broad-band chaotic vibration at various rotational speeds. In addition, it is found that the bearing defects manifest themselves as periodic impulses, disturbing the chaotic behavior of a normal system. The experimental and simulation results reveal that faults significantly affect the chaotic quantifiers: Lyapunov exponent, correlation dimension, and information entropy. Therefore, they have the potential to be bearing fault indicator.

Consequently, the sensitivity and robustness of these quantifiers are compared by well-known diagnostic methods. The experimental results pinpoint three indices as the most sensitive and robust monitoring features for fault diagnosis: Normalized Information Entropy (NIE), Correlation Dimension (CD), and Maximum of Approximated Coefficient Wavelet (MACW). Theses monitoring indices are less sensitive to load and shaft speed variations.

To integrate the strengths of the three proposed monitoring indices, a neural-based diagnostic system is developed. The monitoring indices used as the input of the diagnostic scheme, and the output of the system corresponds to the level of bearing's health. The comparison demonstrates that the Neuro-Fuzzy Inference System (ANFIS) is more efficient to map the indices into the condition of the bearings. In a number of experiments, the overall reliability of the newly developed diagnostic system is more than 95%.

A prognostic scheme can be employed to forecast the future states of the fault propagation, based on the previous and current state of the system. From all the flexible-model-based forecasting approaches, the most promising methods are Recurrent Neural Networks (RNNs), and ANFIS. By assessing the performance of these two predictors, it is found that once an ANFIS system is properly trained, it performs better than RNNs in the one-step-ahead prediction of monitoring indices. Furthermore, it is concluded, that if an ANFIS system is trained with the run-to-damage vibration data of a bearing, the network can capture the damage propagation behavior accurately. Such trained networks are utilized successfully to predict the future states of the same series of bearings under different speed and load conditions. The reliability of the proposed system is reinforced by the logical combination of the three monitoring indices. The test results confirm a success rate greater than 98 percent.

The proposed system, due to its high robustness and sensitivity, is suitable for condition monitoring of rotary machines in critical operations. The research accomplished in this thesis should be continued in the following directions:

- Integrate the other diagnostic techniques developed for the gears, shafts, and power transmission components with the proposed scheme to create a comprehensive monitoring system for rotary machinery.
- Develop a stand-alone integrated sensor instrument to provide continuous on-line bearing health information.
- Test the proposed monitoring system on large-scale rotary machines such as turbines, and industrial fans.

Appendix I

To calculate the equivalent stiffness, k, for each rolling element in bearings, it is assumed that the contact area between the element and either ring is very small, compared with curvature radii. The radial deformation, δ, is obtained [100] by applying the Hertzian contact theory, for two sphere bodies (ball bearings) with elastic module E, Poisson ratio v, and compressing force Q such that

$$\delta = \frac{3K}{\pi\mu}\sqrt[3]{\frac{\left(1-\nu^2\right)\sum\rho}{3E^2}Q^2} \tag{I.1}$$

where $\Sigma\ \rho$ is the summation of the curvatures between the raceways and the rolling elements in the principal planes. The curvatures are identified by two indices; the first refers to the body, and the second refers to the principal plane, as illustrated in Figure I.1. The element curvature is the reciprocal value of the associated radii. The sign of ρ is positive, when the centre lies inside the body, and negative when the centre is located outside.

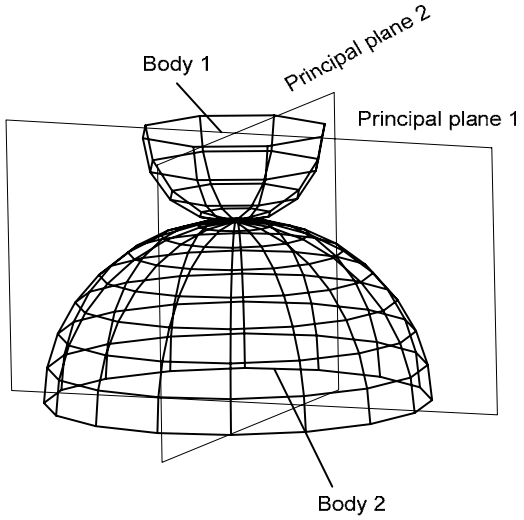

Figure I.1. Contact of two bodies with curved surfaces

According to the Hertzian theory definition, the coefficients, μ and K, are determined as the functions of $\cos(\tau)$, as follows:

$$\cos(\tau) = \frac{\rho_{11} - \rho_{12} + \rho_{21} - \rho_{22}}{\sum \rho} \tag{I.2}$$

Since the material properties and the geometry of a bearing are constant, (I.2) can be is simplified to

$$\Delta = \Gamma \sqrt[3]{\sum \rho} Q^{2/3} \tag{I.3}$$

where Γ is Hertzian deformation constant. The curvature summation for each element-ring contact is obtained from

$$\begin{aligned} \sum \rho_i &= \frac{4}{D_b} + \frac{2}{D_m - D_b} - \frac{1}{r_i} \\ \sum \rho_o &= \frac{4}{D_b} - \frac{2}{D_m + D_b} - \frac{1}{r_o} \end{aligned} \tag{I.4}$$

where D_b is the ball diameter, D_m corresponds to the pitch diameter, and r_i, and r_o represent the inner and outer race groove radii. The ball deformation between the outer and inner rings can be modelled as two springs in series. Therefore, the compression force for each ball-ring contact is governed by

$$Q_{i/o} = k_{i/o} \delta_{i/o}^{2/3} \tag{I.5}$$

where indices *i* and *o* correspond to the inner and outer rings. By combining (I.4) and (I.5)

$$\begin{aligned} k_i &= \Gamma^{-3/2} \left(\frac{4}{D_b} + \frac{2}{D_m - D_b} - \frac{1}{r_i} \right)^{-0.5} \\ k_o &= \Gamma^{-3/2} \left(\frac{4}{D_b} - \frac{2}{D_m + D_b} - \frac{1}{r_o} \right)^{-0.5} \end{aligned} \tag{I.6}$$

The total radial deformation for the ball element, δ, can be written in the form of

$$\delta = \delta_i + \delta_o = \left(\frac{Q_i}{k_i} \right)^{\frac{2}{3}} + \left(\frac{Q_o}{k_o} \right)^{\frac{2}{3}} \tag{I.7}$$

By considering the equal compression force $Q = Q_i = Q_o$ in spring series and by substituting (I.6) in (I.7) results in the equation of equivalent stiffness, k (N/m$^{1.5}$), of each rolling element in ball bearings as follows:

$$\sqrt[3]{\frac{1}{k^2}} = \Gamma^{-3/2}\sqrt[3]{\frac{4}{D_b}+\frac{2}{D_m-D_b}-\frac{1}{r_i}} + \Gamma^{-3/2}\sqrt[3]{\frac{4}{D_b}-\frac{2}{D_m+D_b}-\frac{1}{r_o}} \tag{I.8}$$

In the cylindrical roller bearings, the contact between the roller and rings is assumed to be a line that is parallel to the trust axis, as shown in Figure I.2. It is experimentally established [100] that the deformation δ (mm) is governed by

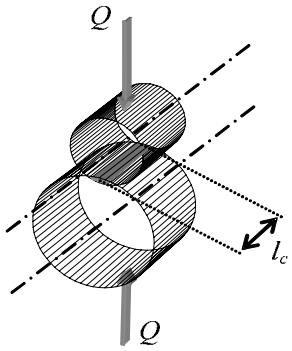

Figure I.2. Line contact between roller and raceways

$$\delta = 4.05\times10^{-5}\frac{Q^{0.925}}{\left(l_c-2r_c\right)^{0.85}} \tag{I.9}$$

In this equation, l_c is the length of contact, and r_c is the radius of roller edge. Since the deformation of two cylinders is independent of the contact body diameters, the total deformation of each element is written in the form of

$$Q = k\delta^{1.08} \tag{I.10}$$

Likewise, the ball bearings, the equivalent stiffness of the element in cylindrical roller bearings, k (N/mm$^{1.08}$) is obtained from

$$k = 2.6232\times10^{4}\left(l_c-2r_c\right)^{0.92} \tag{I.11}$$

Appendix II

Figure II.1 shows the probability distribution of the bearing vibration data, compared with normal distribution. Since the distribution of data is mostly linear within the probability of 2% and 98%, the distribution of data can be assumed to be a normal distribution.

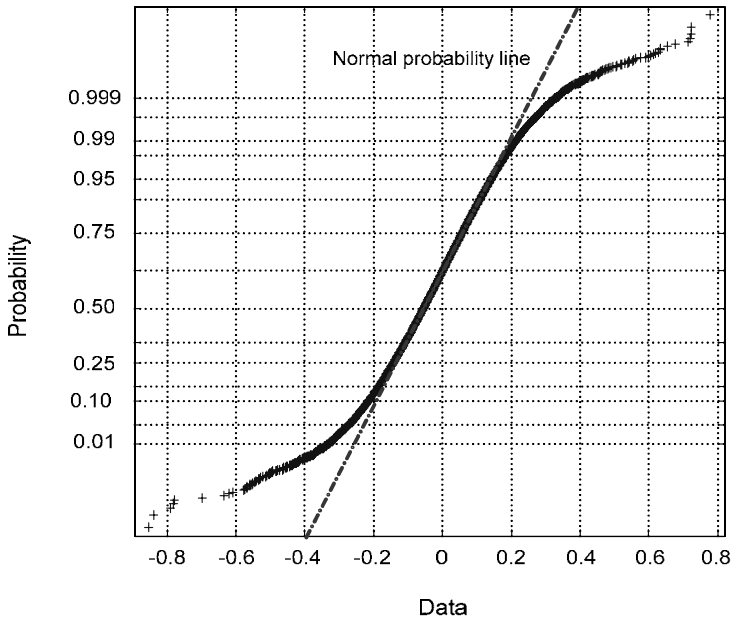

Figure II.1. Probability distribution of normal bearing vibration data

The probability function of a normal distribution is

$$P(x) = \frac{1}{\sqrt{2\pi\sigma^2}} e^{\frac{-(x-\bar{x})^2}{2\sigma^2}} \tag{II.1}$$

where $\bar{x}$ is the mean and σ^2 is the variance of data. Since Kurtosis is defined as the normalized form of the fourth central moment of the distribution, the value of Kurtosis for a normal distribution is calculated by

$$\text{Kurtosis} = \frac{1}{\sigma^4} \int_{-\infty}^{+\infty} \left(x - \bar{x}\right)^4 P(x)\, dx \tag{II.2}$$

By substituting (II.1) in (II.2) the value of Kurtosis for normal bearing is found by

$$\text{Kurtosis} = \frac{1}{\sigma^4}\int_{-\infty}^{+\infty}\left(x-\bar{x}\right)^4 \frac{e^{\frac{-\left(x-\bar{x}\right)^2}{2\sigma^2}}}{\sqrt{2\pi\sigma^2}}dx = \frac{1}{\sigma^5\sqrt{2\pi}}\left(3\sigma^5\sqrt{2\pi}\right) = 3 \qquad \text{(II.3)}$$

References

[1] Shigley J.E. and Mischke C.R., Mechanical Engineering Design, 5th edition, McGraw-Hill, **1989**.

[2] Standard ISO 281, Rolling bearings - Dynamic load ratings and rating life, **2007**.

[3] Gustafsson O.G. and Tallian T., "Research report on study of the vibration Characteristics of Bearings," Report: AL631023, Reg. 585 14:422 3, **1963**, SKF Inc.

[4] Sunnersjö C.S., "Varying compliance vibrations of rolling bearings," *Sound and Vibration*, v 58, n 3, **1978**, pp. 363-373.

[5] Meyer L.D., Ahlgren F.F., and Weichbrodt B., "An analytic model for ball bearing vibrations to predict vibration response to distributed defects," *Mechanical Design*, v 102, **1980**, pp. 205-210.

[6] Mevel B. and Guyader J.L., "Routes to chaos in ball bearings," *Sound and Vibration*, v 162, n 3, **1993,** pp. 471-487.

[7] Ghafari S.H., Golnaraghi F., and Ismail F., "Fault diagnosis based on chaotic vibration of rotor systems Supported by Ball Bearings," *Proceeding of COMADEM 2006*, **2006**, pp. 819-826.

[8] Logan D. and Mathew J., "Using the correlation dimension for vibration fault diagnosis of rolling element bearings - I. Basic concepts," *Mechanical Systems and Signal Processing*, v 10, n 3, **1996**, pp. 241-250.

[9] Logan D. and Mathew J., "Using the correlation dimension for vibration fault diagnosis of rolling element bearings - II. Selection of experimental parameters," *Mechanical Systems and Signal Processing*, v 10, n 3, **1996**, pp. 251-264.

[10] Choy F.K., Zhou J., Braun M.J., and Wang L., "Vibration monitoring and damage quantification of faulty ball bearings," *Tribology*, v 127, n 4, **2005**, pp. 776-783.

[11] Tandon N., "A comparison of some vibration parameters for the condition monitoring of rolling element bearings," *Measurement*, v 12, **1994**, pp.285-289.

[12] Downham E., "Vibration monitoring and wear prediction," *Proceeding of 2nd International conference on vibration in rotary machinery, IMechE*, **1980**, pp. 29-33.

[13] Dyer D. and Stewart R.M., "Detection of rolling element bearing damage by statistical vibration analysis," *Mechanical Design*, v 100, n 3, **1978**, pp. 229-235.

[14] Stronach A.F., Cudworth C.J., and Johnston A.B., "Condition monitoring of rolling element bearing," *Proceeding of International Conference on Condition Monitoring*, Swansea, UK, **1984**, pp. 162-177.

[15] Williams T., Ribadeneira X., Billington S., and Kurfesss T., "Rolling element bearing diagnostics in run-to-failure lifetime testing," *Mechanical Systems and Signal Processing*, v 15, n 5, **2001**, pp. 979-993.

[16] White M. F., "Simulation and analysis of machinery fault signals," *Sound and Vibration*, v 93, **1984**, p 95-116.

[17] Mathew J. and Alfredson R.J, "The condition monitoring of rolling element bearing using vibration analysis," *Vibration and Acoustics, Stress, and Reliability in Design*, v 106, **1984**, pp. 447-453.

[18] Ingarashi T., Noda B., and Matsushima E., "A study on the prediction of abnormalities in rolling bearing," *JSLE*, v 1, **1980**, pp. 71-76.

[19] Hemmings R.C., Smith, J.D. "Information from bearing vibration," *IMechE*, **1976**

[20] Tandon N. and Nakara B.C., "Comparison of vibration and acoustic measurement techniques for condition monitoring of rolling element bearings," *Tribology International*, v 25, n 3, **1992**, pp. 205-212.

[21] Butler D.E., "The shock pulse method for detection of damaged rolling bearings," *NDT International*, **1973**, pp. 92-95.

[22] Smith J.D., "Vibration monitoring of bearings at low speeds," *Tribology International*, v 15, **1982**, pp. 139-144.

[23] Igarashi T. and Hamada H., "Studies on the vibration and sound of defective rolling bearings (first report: vibration of ball bearings with one defect)," *JSME*, v 25, **1989**, pp. 248-253.

[24] Taylor J.I., "Identification of bearing defects by spectral analysis," *Mechanical Design*, v 102, **1980**, pp. 199-204.

[25] Osuagwu C.C. and Thomas D.W., "Effect of inter-modulation and quasi-periodic instability in the diagnosis of rolling element incipient defect," *Mechanical Design*, v 104, **1982**, pp. 296-302.

[26] Kadushin D., "Roller element bearing fault analysis using envelope detection during an experimental case study," *Proceeding of 3rd International Machinery Monitoring and Diagnostics Conference, COMADEM 91*, **1991**, pp. 132-141

[27] McMohan S.W. and Scott T., "Condition monitoring of bearing using ESP and an expert system," *Proceeding of 3rd International Machinery Monitoring and Diagnostics Conference, COMADEM 91*, **1991**, pp. 165-182

[28] Milne R., Aylett J., McMahon S., and Scott T., "Portable bearing diagnostics using enveloping and expert systems," *Proceeding of 3rd international Machinery Monitoring and Diagnostics Conference, COMADEM 91*, **1991**, pp. 75-79

[29] Martin K.F. and Thrope P., "Normalized spectra in monitoring of rolling bearing elements," *Wear*, v 159, **1992**, pp. 153-160.

[30] Ho D. and Randall R.B., "Optimization of bearing diagnostic techniques using simulated and actual bearing fault signals," *Mechanical Systems and Signal Processing*, v 14, n 5, **2000**, pp. 763-788.

[31] McFadden P.D., and Toozhy M.M., "Application of synchronous averaging to vibration monitoring of rolling element bearings," *Mechanical Systems and Signal Processing*, v 14, n 6, **2000**, pp. 891-906.

[32] Randall R.B., Antoni J., and Chobsaard S., "The relationship between spectral correlation and envelope analysis in the diagnostics of bearing faults and other cyclostationary machine signals," *Mechanical Systems and Signal Processing*, v 15, n 5, **2001**, pp. 945-962.

[33] Jianfang J., Yuemping S., and Qi Z., "A method of bearing vibration signal extraction and fault detection," *Proceeding of 1st International Machinery Monitoring and Diagnostics Conference*, **1989**, pp.149-154.

[34] McFadden P.D. and Smith J.D., "Vibration monitoring of rolling element bearings by the high frequency resonance technique-a review," *Tribology International*, v 17, n 1, **1984**, pp. 3-10.

[35] Ghosh M. and Rajamani A., "Diagnostic monitoring of antifriction bearings," *Inter Noise*, **1986**, pp. 1187-1190.

[36] Lai M.S. and Reif Z., "Prediction of ball bearing failures," *Proceeding of 1st International Machinery Monitoring and Diagnostics Conference*, **1989**, pp. 122-126.

[37] Bolaers F., Cousinard O., Marconnet P., and Rasolofondraibe L., "Advanced detection of rolling bearing spalling from de-noising vibratory signals," *Control Engineering Practice,* v 12, **2004**, pp. 181-190.

[38] Ericsson S., Grip N., Johansson E., Persson L.E., Sjoberg R., and Stromberg J.O., "Towards automatic detection of local bearing defects in rotating machines," *Mechanical Systems and Signal Processing*, v 19, **2005**, pp. 509-535.

[39] Yang H., Mathew J., and Ma L., "Fault diagnosis of rolling element bearings using basis pursuit," *Mechanical Systems and Signal Processing*, v 19, **2005**, pp. 341-356.

[40] Prabhakar S., Mohanty A.R., and Sekhar A.S., "Application of discrete wavelet transform for detection of ball bearing race fault," *Tribology International*, v 35, **2002**, pp. 793-800.

[41] Liu B., Ling S. F., and Gribonval R., "Bearing failure detection using matching pursuit," *NDT&E International*, v 35, **2002**, pp. 255-262.

[42] Li C.J. and Ma J., "Wavelet decomposition of vibrations for detection of bearing-localized defects," *NDT&E International*, v 30, **1997**, pp. 143-149.

[43] Nikolaou N.G. and Antoniadis I.A., "Demodulation of vibration signals generated by defects in rolling element bearings using complex shifted Morlet wavelets," *Mechanical Systems and Signal Processing*, v 16, n 4, **2002**, pp. 677-694.

[44] Rubini R. and Meneghetti U., "Application of the envelope and wavelet transform analyses for the diagnosis of incipient faults in ball bearings," *Mechanical Systems and Signal Processing*, v 15, n 2, **2001**, pp. 287-302.

[45] Sun Q. and Tang Y., "Singularity analysis using continuous wavelet transform for bearing fault diagnosis," *Mechanical Systems and Signal Processing*, v 16, n 6, **2002**, pp. 1025-1041.

[46] Mori K., Kasashima N., Yoshioka T., and Ueno Y., "Prediction of spalling on a ball bearing by applying the discrete wavelet transform to vibration signals," *Wear*, v 195, **1996**, pp. 162-168.

[47] Altmann J. and Mathew J., "Multiple band-pass autoregressive demodulation for rolling-element bearing fault diagnosis," *Mechanical Systems and Signal Processing*, v 15, n 5, **2001**, pp. 963-977.

[48] Nikolaou N.G. and Antoniadis I.A., "Rolling element bearing fault diagnosis using wavelet packets," *NDT&E International*, v 35, **2002**, pp.197-205.

[49] He Z., Wu M., and Gong B., "Neural network and its application on machinery fault diagnosis," *Proceeding of IEEE International Conference on Systems Engineering*, **1992**, pp. 576-579.

[50] Baillie D.C. and Mathew J., "A comparison of autoregressive modeling techniques for fault diagnosis of roller element bearings," *Mechanical Systems and Signal Processing*, v 10, n 1, **1996**, pp. 1-17.

[51] Samanta B.and Al-Balushi K.R., "Artificial neural network based fault diagnostics of rolling element bearings using time domain features," *Mechanical Systems and Signal Processing*, v 17, n 2, **2003**, pp. 317-328.

[52] Jack L.B., Nandi A.K., and McCormick A.C., "Diagnosis of rolling element bearing faults using radial basis function networks," *Applied Signal Processing*, v 6, **1999**, pp. 25-32.

[53] Vachtsevanos G. and Wang P., "Fault prognosis using dynamic wavelet neural networks," *IEEE Systems Readiness Technology*, **2001**, pp. 857-870.

[54] Subrahmanyam M. and Sujatha C., "Using neural networks for the diagnosis of localized defects in ball bearings," *Tribology International*, **1997**, v 30, n 10, pp. 739-752.

[55] Lou X. and Loparo K.A., "Bearing fault diagnosis based on wavelet transform and fuzzy inference," *Mechanical Systems and Signal Processing*, v 18, **2004**, pp. 1077-1095

[56] Dailly C. and Welford R.J., "Signal processing within a real time AI architecture," *IEEE colloquium on Condition Monitoring and Failure Diagnosis II, Digest 102,* **1989**, pp. 1-12.

[57] McMahon S.W. and Scott T., "Condition monitoring of bearings using ESP and an expert system," *Proceeding of 3rd International Machinery Monitoring and Diagnostics conference, COMADEM 91*, **1991**, pp. 165-182.

[58] Shi X.Z., Chen H., Liu R.Q., and Sun H.Q., "A PC-based fault diagnostic and quality evaluation system for ball bearing," *Proceeding of 2nd international Machinery Monitoring and Diagnostics conference, COMADEM 90*, **1990**, pp. 259-263.

[59] Spoerre J.K., "Application of the cascade correlation algorithm (CAA) to bearing fault classification problems," *Computers in Industry*, v 32, **1997**, pp. 295-304.

[60] Purushotham V., Narayanan S., and Prasad S.A.N, "Multi-fault diagnosis of rolling bearing elements using wavelet analysis and hidden Markov model based fault recognition," *NDT&E International*, v 38, **2005**, pp. 654-664.

[61] Liu T.I., Singonahalli J.H., and Iyer N.R., "Detection of Roller bearing defects using expert system and fuzzy logic," *Mechanical Systems and Signal Processing*, v 10, n 5, **1996**, pp. 595-614.

[62] Yang J., Zhang Y., and Zhu Y., "Intelligent fault diagnosis of rolling element bearing based on SVMs and fractal dimension," *Mechanical Systems and Signal Processing*, v 21, n 5, **2007**, pp. 2012-2024.

[63] Samanta B., Al-Balushi K.R., and Al-Araimi S.A., "Artificial neural network and support vector machines with genetic algorithm for bearing fault detection," *Engineering Applications of artificial Intelligence*, v 16, **2003**, pp. 657-665.

[64] Lei Y., He Z., Zi Y., and Hu Q., "Fault diagnosis of rotating machinery based on multiple ANFIS combination with GAs," *Mechanical Systems and Signal Processing*, v 21, n 5, **2007**, pp. 2280-2294.

[65] Samanta B., Al-Balushi K.R., and Al-Araimi S.A., "Bearing fault detection using artificial neural networks and genetic algorithm*," EURASIP, Applied Signal Processing*, **2004**, pp. 366-377.

[66] Wang X.F., Shi X.Z., and Xu M., "The fault diagnosis and quality evaluation of ball bearing by vibration signal processing," *Proceeding of 1st International Machinery Monitoring and Diagnostics Conference*, **1989**, pp. 318-321.

[67] Weibull W., "A statistical representation of fatigue failures in solids," *Acta Polytechnica, Mechanical Engineering Series 1, Royal Swedish Academy of Engineering Sciences*, **1949**, n.9.

[68] Lundberg G. and Palmgren A., "Dynamic capacity of rolling bearings," *Acta Polytechnica, Mechanical Engineering Series 1, Royal Swedish Academy of Engineering Sciences*, **1947**, n 3.

[69] Tallian T.E., "Data fitted bearing life prediction model for variable operating conditions," *Tribology Transactions*, **1999**, v 42, n1, pp. 241-249.

[70] Ioannides E. and Harris T.A., "A new fatigue life model for rolling bearings," *Journal of Tribology*, **1985**, v 107, pp. 367-378.

[71] Qiu J., Zhang C., Seth B.B., and Liang S.Y., "Damage mechanics approach for bearing lifetime prognostics," *Mechanical Systems and Signal Processing*, **2002**, v 16, n 5, pp. 817-829.

[72] Zhang C., Chuckpaiwong I., Liang S.Y., and Seth B.B., "Mechanical component lifetime estimation based on accelerated life testing with singularity extrapolation," *Mechanical Systems and Signal Processing*, **2002**, v 16, n 4, pp. 705-718.

[73] Guangyoung S., "Auxiliary bearing life prediction using Hertzian contact bearing model," *Vibration and Acoustics*, **2006**, v 128, pp. 203-209.

[74] Malhi A. and Gao R.X., "Recurrent neural networks for long-term prediction in machine condition monitoring," *Instrumentation and Measurement Technology Conference*, **2004**, pp. 2048-20.

[75] Gebraeel N., Lawley M., Liu R., and Parmeshwaran V., "Residual life prediction from vibration based degradation signals: A neural network approach," *IEEE Transactions on Industrial Electronics*, **2004**, v 51, n 3, pp. 694-700.

[76] Huang R., Xi L., Li X., Liu C.R., Qiu H., and Lee, J., "Residual life prediction for ball bearings based on self-organizing map and back propagation neural network methods," *Mechanical Systems and Signal Processing*, **2007**, v 21, pp. 193-207.

[77] Ghafari S.H., Golnaraghi F., and Ismail F., "Rolling element bearings fault diagnosis based on neuro-fuzzy inference system," *Proceeding of CMVA 2006, Canadian Machinery Vibration Association*, **2006.**

[78] Tallian T.E. and Gustafsson O.G., "Progress in rolling bearing vibration research and control," *ASLE Transaction,* v 8, n 3, **1965**, pp. 195–207.

[79] Wardle F.P. and Poon S.Y., "Rolling bearing noise - cause and cure," *Chartered Mechanical Engineer*, v 30, n 7-8, **1983**, pp. 36-40.

[80] Tandon N. and Choudhury A., "An analytical model for the prediction of the vibration response of ball bearings due to a localized defect," *Sound and Vibration*, v 205, n 3, **1997**, pp. 275-292.

[81] Choudhury A. and Tandon N., "Vibration response of ball bearings in a rotor bearing system to a local defect under radial load," *Tribology*, v 128, n 2, **2006**, pp. 252-261.

[82] Akturk N., Uneeb M., and Gohar R., "The Effects of Number of Balls and Preload on Vibration Associated with Ball Bearings," *Tribology*, v 119, **1997**, pp. 747-753.

[83] Akturk N., "Some characteristic parameters affecting the natural frequency of a rotating shaft supported by defect-free ball bearings," *Journal of Multi-Body Dynamics*, v 217, n 2, **2003**, pp. 145-51.

[84] Tamura H. and Shimizu H., "Vibration of rotor based on ball bearing – 2nd report, static stiffness of ball bearing containing a small number of balls," *JSME*, v 10, n 41, **1967**, pp. 763-775.

[85] Shimizu H. and Tamura H., "Vibration of rotor based on ball bearing – 1st report, static stiffness of ball bearing," *JSME*, v 9, n 35, **1966**, pp. 524-532.

[86] Tamura H. and Tsuda Y., "On the spring characteristics of a ball bearing – extreme characteristics with many balls," *JSME*, v 23, n 180, **1980**, pp. 961-969.

[87] Harsha S.P., "Nonlinear dynamic analysis of a high-speed rotor supported by ball bearings," *Sound and Vibration*, v 290, n 1-2, **2006**, pp. 65-100.

[88] Harsha S.P., Sandeep K., and Prakash R., "Nonlinear dynamic response of a rotor bearing system due to surface waviness," *Nonlinear Dynamics*, v 37, n 2, **2004**, pp. 91-114.

[89] Harsha S.P. and Kankar P.K., "Stability analysis of a rotor bearing system due to surface waviness and number of balls," *Mechanical Sciences*, v 46, n 7, **2004**, pp. 1057-1081.

[90] Gad E.H., Fukata S., and Tamura H., "Computer simulation of rotor radial vibration due to ball bearings," *Memoirs of the Faculty of Engineering, Kyushu University*, v 44, n 1, **1984**, pp. 83-111.

[91] Tiwari M., Gupta K., and Prakash O., "Effect of radial internal clearance of ball bearing on the dynamics of a balanced horizontal rotor," *Sound and Vibration*, v 238, n 5, **2000**, pp. 723-756.

[92] Moon F.C., Chaotic Vibrations, An Introduction for Applied Scientists and Engineers, Wiley, **1987**.

[93] Nayfeh A.H., "Resolving controversies in the application of the method of multiple scales and the generalized method of averaging," *Nonlinear Dynamics*, v 40, **2005**, pp. 61-102.

[94] Fukata S., Gad E.H., Kondou T., Ayabe T., and Tamura H., "On the vibration of ball bearings," *JSME*, v 28, **1985**, pp. 899-904.

[95] Tsuda Y., Masunaga T., Matsuzaki K., Tamura H., and Gad H., "On chaotic behaviours in the radial vibrations of a ball bearing," *JSME*, v 58, n 553, **1992**, pp. 2607-2614.

[96] Kahraman A. and Singh R., "Non-linear dynamics of a geared rotor bearing system with multiple clearances," *Sound and Vibration*, v 144, n 3, **1991**, pp. 469-506.

[97] Harsha S.P., "Nonlinear dynamic response of a balanced rotor supported by rolling element bearings due to radial internal clearance," *Mechanism and Machine Theory*, v 41, **2006**, pp. 688-706.

[98] Bai C.Q., Xu Q.Y., and Zhang X.L., "Nonlinear stability of balanced rotor due to effect of ball bearing internal clearance," *Applied Mathematics and Mechanics*, v 27, n 2, **2006**, pp. 175-186.

[99] Lioulios A.N. and Antoniadis I.A., "Effect of rotational speed fluctuations on the dynamic behaviour of rolling element bearings with radial clearances," *Mechanical Sciences*, v 48, **2006**, pp. 809-829.

[100] Eschmann P, Ball and Roller Bearings-theory, design, and application, Willey, **1985.**

[101] Lin D.C., Augustine B.J., and Golnaraghi F., "Point-wise dimension estimate of nonstationary, multi-episodes, time series and application to gearbox signal,", *17th Biennial Conference on Mechanical Vibration and Noise, Symposium on Fault Detection/ Diagnostics in Rotating Machinery,* **1999.**

[102] Li C. and Qu L., "Applications of chaotic oscillator in machinery fault diagnosis," *Mechanical Systems and Signal Processing*, v 21, **2007**, pp. 257-269.

[103] Wolf A., Swift J.B., Swinney H.L., and Vastano J.A., "Determining Lyapunov exponents from a time series," *Physica*, 16D, **1985**, pp. 285-317.

[104] Ruelle D., "Deterministic chaos: the science and fiction," *Proceedings of the Royal society of London*, A427, **1990**, pp. 241-248.

[105] Simm C.W., Sawley M.L., Skiff F., and Pochelon A., "On the analysis of experimental signals for evidence of deterministic of chaos," *Physica*, v 60, **1987**, pp. 510-551.

[106] Kaplan J. and Yorke J.A., Lecture notes in Mathematics, v 730, p 228, Springer, **1978.**

[107] S. Braun, B. Datner, "Analysis of Roller/Ball bearing vibration," *Transaction of ASME*, v 101, **1979**, pp. 118-125.

[108] Jing L., Zuo, M.J., and Fyfe, K.R., "Mechanical fault detection based on the wavelet de-noising technique," *Vibration and Acoustics*, v 126, n 1, **2004,** pp. 9-16.

[109] Luo G.Y., Osypiw D., and Irle M., "On-line vibration analysis with fast continuous wavelet algorithm for condition monitoring of bearing," *Vibration and Control*, v 9, **2003**, pp. 931-947.

[110] Newland D.E., An introduction to Random vibrations spectral and wavelet analysis, 3rd edition, Longman Scientific & Technical, **1993**.

[111] Wang W., Ismail F., and Golnaraghi F., "A Neuro-Fuzzy approach to gear system monitoring," *IEEE Transactions on Fuzzy Systems*, v 12, n 5, **2004**, pp. 710-723.

[112] Yu Y., Dejie Y., and Junsheng C., "A roller bearing fault diagnosis method based on EMD energy entropy and ANN," *Sound and Vibration*, v 294, **2006**, pp. 269-277.

[113] Karray, F.O. and Silva, C. D., Soft Computing and Intelligent Systems Design, Pearson-Addison Wesley, **2004**.

[114] Wang W.Q., Golnaraghi M.F., and Ismail, F., "Prognosis of machine health condition using neuro-fuzzy systems," *Mechanical Systems and Signal Processing*, v 18, **2004,** pp. 813-831.

[115] Hoeprich M. R., “Rolling element bearing fatigue damage propagation,” *Tribology*, v 114, **1992**, pp. 328-333.